Doctoral Dissertation

Simulation and experiments of optical emission spectroscopy for real-time plasma diagnostics

ARELLANO FATIMA JENINA TOLENTINO

June 2024

International Priority Graduate Program on Applied and Engineering Physics

Division of Precision Engineering and Applied Physics

Graduate School of Engineering

OSAKA UNIVERSITY

ABSTRACT

Optical emission spectroscopy (OES) is a highly valuable tool for real-time monitoring of plasma properties due to its non-intrusive and versatile nature. However, utilizing OES for real-time monitoring presents specific challenges, such as extracting the desired plasma characteristics from the information in the measured spectra and developing a corresponding real-time prediction model of the plasma properties. This work aims to address these specific challenges associated with determining the plasma parameters from the spectral measurements.

The first part of this work takes a step towards a better understanding of the physics behind the measured spectra by validating existing widely-used simulation models with experimental measurements. Spectral line intensities are calculated through the one-way coupling of a one-dimensional Particle-in-Cell/Monte Carlo Collision (PIC/MCC) simulations with a global collisional-radiative model. In this way, the line intensities can be determined from specific electron density n_{e} and the electron energy distribution function (EEDF) values calculated using the PIC/MCC simulation for a capacitively coupled radiofrequency argon plasma with pressure ranging from 2 to 100 Pa. Comparison of simulated spectral intensities to experimentally-measured ones shows reasonable agreement for a gas pressure up to 20 Pa. The discrepancies at high pressures are attributed to incomplete ionization balance due to the neglect

of the contribution from the metastable levels in basic PIC/MCC simulations, which is found to be important at this pressure range.

The second part of this work aims to then make a prediction model of the n_e and the EEDF from the spectral data using machine learning (ML) techniques. It uses two different models to predict the normalized EEDF, namely the Kernel Regression for Functional Data and an artificial neural network. To predict the n_e, a Random Forest regression model is used. The ML models are trained with normalized simulated spectral intensities described in the first work, but this time with the peak-to-peak voltage varied from 200 V - 500 V. All three ML models developed in this study are found to predict the plasma parameters from the simulated spectral test data well. As an additional test, the model is also used to predict from experimentally measured normalized spectral intensities, in which the models show limited capability in predicting the n_e and the EEDF, indicating a need for further improvement in the robustness of these models.

The last part aims to address the determination of plasma parameters during fluctuations and instabilities happening in magnetically confined plasmas over a short period of time ($\sim 100\mu s$). For such measurements, spectrometers with a high optical transmission-to-spectral resolution ratio must be used. A spatial heterodyne spectrometer (SHS) has field-widening prisms that realign the light passing through a detector, such that a higher resolution can still be achieved even with a large aperture size. In this study, the performance of an SHS in

charge exchange spectroscopic measurements of the toroidal flow velocity and the ion temperature of the C^{6+} impurity ion in the Large Helical Device is explored. Additionally, the resulting measurements are compared to those of conventional dispersive spectrometers typically used and found to be in good agreement with them.

ACKNOWLEDGMENTS

First of all, I would like to thank Jesus, my peace and my fortress during this PhD.

Words are not enough to thank my supervisor, Prof. Satoshi Hamaguchi, without whom I would not even be here. He has been so patient with me, imparting his wisdom and enthusiasm in research to me. He inspires me to see the unfamiliar as a learning opportunity and has taught me to see mechanisms in terms of equations. I thank him for all the discussions he had with me and all the opportunities he has handed me with. He took me in his group and helped me become the researcher I am now. I hope I can someday make you proud.

I am also very much blessed to have learned from so many experts in our field, from whom I never imagined I can learn from. First of which is Prof. Dr. Zoltan Donko, who has been guiding me since first year of Masters. He has been very kind, patient and hands-on in teaching me about the PIC/MCC code, conducting experiments, and writing papers. He has not only been a good teacher to me, but also a good friend of me and Marvin. Truly, he has been very instrumental in this PhD. I have also been fortunate to have engaged in a lot of discussions with Dr. Tsanko V. Tsankov, who is also very bright and very kind in answering even my smallest questions. I also am very much thankful to Dr. Peter Hartmann, who had always been so nice to me whenever I visit Budapest, assisting and conducting experiments with us. Prof. Uwe

Czarnetzki has also been very bright and inspiring in helping our study be fruitful.

I am also very fortunate for the opportunity to visit the Institute of Statistical Mathematics in Tachikawa, Tokyo. Prof. Yoshida and Dr. Stephen Wu have been really kind to me every time I visit there. My discussions with them gave me insight into how they think as data scientists. I am very grateful for all the guidance and teachings they provided as I started on my machine learning work. I am also very thankful to Dr. Minoru Kusaba, who was very hands-on in assisting me with using the KRFD. I have learned a great deal about data science from them, and I am very grateful to their group for always being so kind when I visit.

I am also very grateful to Prof. Katsumi Ida and Dr. Mikirou Yoshinuma without whom our CXS work will not be possible. I came to NIFS without knowing much about fusion and I am very grateful for all the help, teachings, and guidance they gave me in order to complete this work.

I have met so many international colleagues along the way, which made this academic journey more enjoyable, from friends in summer school, conferences, which introduced me to different academic systems in different countries and I am very grateful to have met them in my PhD journey. I hope I get more chances in meeting them in the future.

My constant gratitude also goes to the ones whose contribution may not be as evident in this manuscript but have been present in the every day that I

do this research. First of all, my family, who have been very supportive of my decisions in coming here. My friends in the laboratory, those who have gone before me and are still with me in the laboratory, I am grateful to have gained friends in them. And to my family away from home, my church friends from Minoh International Church, one of the reasons I have come to love my stay here in Japan.

Of course I am also very grateful that my graduate studies also led me to meet my fiance, Marvin. He has been there every step of this journey, in every emotional ups and downs, helping me in my work. He is just one of the kindest persons I know and I see how much Jesus loves me through him. Thank you for teaching me 1 Corinthians 13 kind of love.

I would also like to thank those who made my admission to Osaka University possible, my undergraduate supervisor back in the Philippines who introduced me to plasma research, Assoc. Prof. Magdaleno Vasquez Jr. I am also very grateful to Prof. Yoshitada Morikawa and the QEDC/AEP program for this English-based degree program.

I also extend my deepest gratitude to Ministry of Education, Culture, Sports, Science and Technology(MEXT) for the scholarship that allowed me to do my PhD here in Japan.

LIST OF ACRONYMS

RFR Random Forest regression xviii

RMSE root mean square error xvii

SEEC secondary electron emission coefficient 42

SHS spatial heterodyne spectrometer ii

TLS tunable wavelength monochromatic light source 33

TABLE OF CONTENTS

CHAPTER

LIST OF TABLES

TABLE

LIST OF FIGURES

FIGURE

Chapter 1

Introduction

Plasmas are generated by introducing energy into a neutral gas, typically through electrical breakdown aided by external electric and magnetic fields. During this process, charged particles are accelerated by the electric field, resulting in the creation of electrons and ions when high-energy electrons or photons collide with neutral atoms and molecules in the gas[9] These interactions can also trigger reactions and collisions required for various applications. Therefore, plasmas have diverse applications across multiple fields, including semiconductor manufacturing, thin film processing, nanotechnology, cutting, biomedicine, gas conversion, propulsion systems, and nuclear fusion.[10–12]

1.1 Real-time monitoring in semiconductor manufacturing

In semiconductor manufacturing, one of the applications of plasma is in etching and deposition of patterns in flash memories. NAND flash memories have shifted to 3D and deep thin holes with high aspect ratio almost reaching 200 has to be achieved. In order to achieve thinner and deeper etched features and deposited films, better nanoscale process control, improved uniformity, higher selectivity, increased throughput, higher aspect ratios, and minimized damage are required.[13] For such requirements, the energy and the flux of the incoming ions and radicals to the substrate should be controlled. Electron

properties are also very vital as it is usually the electrons which gets heated up from the electric field and transfer their energies to other species. To measure such properties, significant advancements in plasma diagnostics have yielded refined diagnostic techniques like spectroscopy, Langmuir probes, Thomson scattering, and mass spectrometry.[14,15]

Ensuring a high wafer-to-wafer reproducibility amidst a narrow process window necessitates immediate detection and minimization of process drifts, particularly those occurring during plasma etching and deposition. These shifts can be caused by multiple factors such as variability in the radiofrequency (RF) current discharge or duty cycle,[16,17] contamination accumulation on chamber walls,[17–19] temperature changes inside the chamber, non-uniformity in plasma gas composition,[17] or even aging of pumps.[20] Hence, real-time in situ plasma monitoring with feedback control becomes crucial for ensuring a consistent and stable plasma process.

Traditional monitoring approaches employed in the manufacturing process often rely on statistical process control charts, where critical measurements are periodically taken for a set of samples from each batch.[21] If the measurements fall outside the control limits, process diagnosis and corrective actions are implemented. However, the time delay caused by sampling, offline measurements, and identification of problematic processes can result in a huge amount of wasted products. In addition to such batch sampling, real-time in-situ measurements and process diagnostics must be implemented.[22]

Previous works on real-time monitoring involves the use of the use of diagnostics such as a mass spectrometers, residual gas analyzers, ,[23,24] flat cut-off array, sensor[25] self-excited electron resonance spectroscopy,[26,27] laser-based methods,[15,28,29] and ellipsometry.,[30] and other measurement systems on the walls of the chamber.[14,31] Data gathered from equipment parts such as mass flow controller, power supply, or other sensors such as the voltage-current probe, temperature sensors can also be used to monitor the plasma.[18,25,32–37]

In semiconductor manufacturing, information that can be typically obtained in-process includes the optical emission spectra and the current-voltage waveform measured from the oscilloscope. Most manufactured etching chambers typically already include small ports in which optical fibers can see through since the emission spectra is also very helpful in determining the etch stop such that a different species comes out in the spectra once etching the desired pattern is done. OES is a widely used non-invasive plasma diagnostic valued for its versatility and simplicity as compared to other diagnostic tools.[?,38,39] It is extensively employed in characterizing plasma composition and tracking dynamic changes in the plasma.[22,40] Moreover, OES can be employed to determine plasma parameters, such as the electron density n_{e} and the electron energy distribution function (EEDF) or the electron temperature T_{e}, as the electron kinetics are reflected in the excitation dynamics.

Several methods exist to determine the electron density n_{e} and EEDF from the optical emission spectra. One approach involves determining the excitation temperature (T_{exc}) from the slope of the Boltzmann plot of $\ln(I\lambda/g_2A_{12})$

versus the energy of the higher excited level, where I, λ, g_2, and A_{12} represent the intensity, wavelength, statistical weight, and Einstein A-coefficient of the transition, respectively. Under local thermal equilibrium (LTE), the electron temperature (T_e) can be equated to T_exc, or alternatively, it can be determined using the Saha equation and the line-continuum ratio. The electron density (n_e) is then derived from Stark broadening measurements.[41–43] However, this method assumes LTE, which typically occurs only at high electron densities and pressures.[41]

Another method assumes a corona regime, relating T_e to the ratio of emission line intensities from two excited levels, with one line usually originating from an ionic level and the other from a neutral level of the same species.[41,44,45] This assumption is generally valid only at low pressures.[8,46] When trace gases are added to the plasma, actinometry and trace rare gas optical emission spectroscopy (OES) can also determine ground-state species density and T_e.[41,47]

A commonly used method to relate spectral line intensities to plasma parameters employs collisional-radiative models (CRMs).[48–53] CRMs account for the processes that populate and depopulate each excited level, solving a rate balance equation for these levels. This allows plasma parameters affecting electron impact collisions such as n_e and the EEDF to be related to the rate of spontaneous emission reflected in spectral line intensities. Typically, CRM parameters n_e and T_e are varied until the resulting intensities align closely with measured OES intensities.[46,54–64] However, these calculations often assume a single-temperature Maxwellian[54,57–60,62,65,66] or two-temperature

distributions,[41,63,67,68] which may not accurately reflect actual conditions.[8,69,70] A more straightforward approach uses n_e and the EEDF as input parameters to the CRM to generate corresponding spectral intensities. To determine a value for the n_e and a generalized form of the EEDF, plasma simulation models such as the PIC/MCC method can be used.[71–89] This approach is based on the first principles aand tracks charged particles, represented as superparticles (collections of real particles), within time- and space-varying external fields. Therefore it is possible to couple these commonly used models by first calculating the n_e and the EEDF and then using these electron parameters as input to the CRM to calculate the corresponding spectral intensities. As far as we know, such one-way coupling of the two models (denoted as 'PIC+CRM' in the rest of the text) have not been done before this study. In the same way, an investigation of the validity of the coupling of these two commonly-used plasma models in calculating the spectral intensities has to be first done before employing it for monitoring activities.

Recently, there have also been a growing number of studies employing machine learning (ML) to determine the plasma parameters from the OES line intensities.[90–93] Shojaei and Mangolini used the OES and Langmuir probe measurements to predict the EEPF from normalized emission spectral intensities.[92] van der Gaag et. al. used a genetic algorithm to predict regions of the EEDF from the emission from electron-atom bremsstrahlung.[93] Park et. al also predicted T_e and n_e from the OES intensities.[91] In the same way, employing machine learning to somehow 'invert' the CRM and be able to quickly predict

n_e and the EEDF from spectral intensities can be vital for real-time monitoring of plasmas during the etching processes. This is especially useful since solving for the inverse of the CRM is often challenging due to the complexity of determining the realistic shape of the EEDF represented with a limited number of parameters.

The goal of this study is therefore to develop ML models trained from intensities calculated from this one-way coupling in the PIC+CRM. Therefore machine learning models are created for the prediction of the n_e and the EEDF from the spectral intensities. However, before such ML predictions are done, the validity of the PIC+CRM method is first investigated in Chapter 5. The study on the ML prediction of plasma parameters from intensities then follows in Chapter 6.

The scope of this study is limited to low-pressure ($p \leq 100\,\mathrm{Pa}$) RF-driven Ar CCPs with a symmetric pair of large parallel electrodes. For the simulations, a one-dimensional (1D) PIC/MCC code and a 0D global CRM for Ar are used.

1.2 High optical transmission-to-spectral resolution measurements in fusion plasma

Spectroscopy is also widely used in fusion plasmas, especially due to the high temperature which makes the use of probes difficult. It can be used to monitor the parameters of the plasma especially during instabilities and turbulences. Turbulence in magnetically confined plasmas is a major chal-

lenge because it negatively impacts the confinement of particles, energy, and momentum. Caused by radial gradients in plasma density and temperature, this turbulence increases transport levels, disrupting the stability needed to keep plasma species from reaching the reactor walls.[94,95] In particular, these turbulence-induced fluctuations, along with the magnetic field ripples and plasma instabilities, can affect the behavior of the fast ions, which are vital for sustaining fusion reactions and magnetic configurations.[96] Therefore, understanding the mechanism and mitigating these fluctuations and instabilities are important in order to sustain the stable discharge with a significant amount of energetic particles in the plasma.[97]

Some fluctuations and instabilities, however, needs to be highly-resolved in order to be characterized. For example, fluctuations in the intrinsic electric field of the plasma which results to velocity fluctuations can only be detected by small changes in the spectral separation of the beam emission components.[98] Additionally, the loss of energetic particles and the distortion from Maxwell-Boltzmann distribution of carbon impurity ions are reported to occur in the LHD just before magnetohydrodynamic (MHD) bursts.[97] Such fluctuations occur at a short time of $\sim 100\mu$s. To quantify these deviations, a dispersive spectrometer (DS) is typically used in the LHD to measure the ion temperature ($T_{C^{6+}}$) and the toroidal flow velocity (V_f) by charge exchange spectroscopy (CXS). However, the measurements are found to be noisy and it was not easy to quantify these deviations in the velocity distribution. Increasing the aperture size and the amount of photon collected, however, typically de-

grades the spectral resolution in these kinds of dispersive spectrometers. As a consequence, conditional averaging had to be done for intensities measured for ≈ 30 events of MHD bursts for a time period of ≈ 1 s.[97]

Recently, Burke et al. reported the use an SHS to measure the Stark split neutral beam emissions.[98] An SHS employs field-widening prisms that rotate the grating images so that they appear perpendicular to the optical axis and coincident at the output, allowing for a larger aperture size.[99,100] This configuration enables the collection of more photons without substantially compromising spectral resolution. Hence, in this study, we explored the utilization of an SHS for measuring the toroidal flow velocity (V_f) and the ion temperature ($T_{C^{6+}}$) of C^{6+} impurity ion in the LHD by CXS.

1.3 Objectives

In this dissertation, we aim to address the two problems discussed above. In order to achieve this, the following specific objectives will be undertaken:

1. To investigate the one-way coupling of a PIC/MCC simulation and CRM and perform its validation by comparing the resulting calculated intensities with experimental measurements
2. To predict the plasma parameters such as the electron density n_{e} and the electron energy distribution function (EEDF) from the spectral data of argon plasma using machine learning (ML)

3. To explore the use of a spatial heterodyne spectrometer (SHS) to measure the toroidal flow velocity V_f and the ion temperature $T_{C^{6+}}$ of the C^{6+} impurity ion by CXS

Chapter 2

Fundamental concepts

2.1 Specific plasma characteristics

2.1.1 Energy distribution function

The type of discharge created in a plasma is primarily dependent on several key plasma characteristics. To begin with, the energy stored in a plasma is defined by the energy carried by the species present within it. In low-temperature plasmas, electrons are heated more easily due to their smaller mass, resulting in electron temperatures typically around $\approx 30,000$ K.[101] In contrast, neutrals and ions generally remain near room temperature. Such plasmas are ideal for low-temperature applications where it is crucial to prevent the substrate from heating up.

The probability of finding a single species at a specific energy or velocity (kinetic energy) is often expressed in terms of distribution functions. If we assume that the species get heated up around the same rate that it loses its energy to collisions, the shape of this distribution function for a homogeneous plasma often follows a Maxwellian (also knows as Maxwell-Boltzmann) distribution.[102] If normalized such that the area under the curve of the isotropic distribution is unity, this Maxwellian energy distribution is given by:[101]

$$f(\varepsilon) = 2\sqrt{\frac{\varepsilon}{\pi k T^3}} \exp \frac{-\varepsilon}{kT}. \tag{2.1}$$

where ε represents each energy bin in the energy distribution, k is the Boltzmann constant having a value of $k = 1.38 \times 10^{-23}$ J K^{-1}, T is the temperature of the species. However, certain conditions such as infrequent collisions or the presence of high-energy electrons (e.g., from secondary emission) can cause deviations from the Maxwellian distribution.

The energy distribution of the electrons dictates some of the processes happening inside the plasma. That is, if the electron has an energy below ionization threshold but above the excitation threshold of a certain excited level, then excitation to that excited state will more likely happen. Moreover, at energies below the excitation threshold, elastic collision happens mostly.

2.1.2 Plasma density

Another parameter that defines plasma is its degree of ionization, or plasma density. At lengths longer than a Debye length, the plasma typically maintains a state of quasineutrality because ions and electrons cannot move independently without creating an electric field that acts to keep them together. However, in some regions, such as plasma sheaths, a positive space charge is usually maintained. Therefore, in general, the charge density of negative and positive ions in the bulk plasma can be assumed to be equal.

Plasma density can span over 28 orders of magnitude, from $10^6\ \mathrm{m}^{-3}$ in interstellar space to $10^{34}\ \mathrm{m}^{-3}$ within the cores of stars. Some technological applications, such as semiconductor manufacturing, do not require a very high degree of ionization, while discharges used in fusion typically involve high-density plasmas.

2.2 Radiofrequency capacitively-coupled plasmas

RF discharges usually operate in the frequency range of 1–100 MHz.[9] At such frequencies, the heavy ions are not able to follow the modulation of the oscillating electric field. This allow ions ions impact the surfaces with controlled energy near room temperature, enabling precise and directional processing.[103] The power coupling in RF discharges can be achieved by either capacitive coupling or inductive coupling.

A conventional RF CCP typically comprises three main components: an RF power source, an impedance matching network, and the reactor. The RF power source operates within a frequency band that is licensed for commercial use. Since the impedance of the plasma discharge often does not match the impedance of the power source (usually 50 Ω), a matching network is employed. This matching network adjusts the reactance components of the impedance of the plasma to ensure efficient power transfer and stable plasma generation.[9] A blocking capacitor is typically included in the matching network to block the DC component of the voltage. A CCP reactor typically has

two electrodes: one is usually grounded and the other powered by an RF generator with voltages in the hundreds. The whole system works by igniting plasma between the electrodes, forming a capacitor in the system's electrical circuit.[102]

Once the plasma is ignited, the faster electrons are lost to the walls forming a sheath positive space charge. During the positive half-cycle of the RF signal, electrons are attracted towards the powered electrode, leading to a momentary accumulation of negative charge. During the negative half-cycle, electrons are repelled, but due to their higher mobility, they leave the electrode region faster than ions can arrive to neutralize the charge. This creates a negative DC potential which is isolated in the plasma due to the presence of a blocking capacitor between the electrodes and the power supply.[9] A higher DC self-bias allows for a higher etching rate.[?]

The electron density can range from 10^{15}˘$10^{16}\mathrm{m}^{-3}$ in a CCP RF discharge and can reach up to $10^{17}\mathrm{m}^{-3}$ at higher frequencies.[9,104] At low pressures and with the same voltage settings, the density of the background gas is lower, resulting in fewer collisions between electrons and background gases. Consequently, the mean free path of electrons is longer, allowing them to be thermalized to higher energies. These low-pressure conditions are typically ideal for semiconductor applications.

As the pressure increases, the frequency of collisions between electrons and background gas molecules rises, shortening the mean free path of electrons. This increased collision rate leads to a greater transfer of energy from electrons

to background particles, depleting the population of high-energy electrons. At a constant voltage (not power), the electron and ion densities (which are nearly equal in a quasineutral plasma) increase with pressure due to a higher ionization rate at elevated pressures.

2.3 Fusion

Fusion energy has been a topic of interest for decades due to its many benefits. It offers high power densities, abundant fuel sources like deuterium and tritium, and minimal greenhouse gas emissions, resulting in a low carbon footprint. Fusion is inherently safe because it lacks chain reactions and can reduce high-level waste.[105–108] Since about 75% of global greenhouse gas emissions come from the energy sector, fusion energy could significantly help achieve sustainable development goals. Although commercial fusion is expected in the latter half of the 21st century, private companies and startups might speed up its integration into the energy mix.[109–112]

Fusion reactor design mainly focuses on two methods: magnetic confinement and inertial confinement. In magnetic confinement, magnetic fields hold the plasma ions and electrons in place, keeping them in thermal equilibrium so thermonuclear reactions can occur. Methods like neutral beam injection, radiofrequency heating, and electron cyclotron resonance heating are used to raise the plasma temperature and encourage fusion reactions. In inertial

confinement, small fuel pellets are compressed with lasers or particle beams, quickly heating them to initiate fusion reactions.[109,113]

2.3.1 Stellarators and Tokamaks

Magnetic confinement devices, such as tokamaks and stellarators, are widely-used to control plasma in fusion research. Tokamaks, which has become the more popular choice, use superconducting coils around a donut-shaped chamber to generate magnetic fields. These fields, along with electric currents, help stabilize the plasma. However, a significant challenge is maintaining continuous operation because plasma currents are generated intermittently. Well-known tokamaks worldwide include JET in the UK, ASDEX Upgrade in Germany, and EAST in China. ITER represents a major advancement toward achieving commercial fusion.[109,113–115]

On the other hand, stellarators take a different approach. They use twisted coils to control plasma without relying on electric currents. This design ensures inherent stability, enabling continuous operation and greater flexibility in plasma control compared to tokamaks. Notable stellarator projects include Wendelstein 7-X in Germany, HSX in the US, and the Large Helical Device in Japan. Private initiatives are also increasingly exploring stellarator concepts.[109,113–115]

2.3.1.1 LHD

The LHD at the National Institute of Fusion Science in Gifu, Japan is a type of stellarator designed to enhance plasma performance and study the physics of torus-shaped plasmas. It uses fully superconducting coils and several methods to heat the plasma, including injecting neutral beams and using electron cyclotron heating. The LHD can store magnetic energy up to 0.77 GJ, making it a vital tool for studying how fusion plasma behaves. The main heating method is neutral beam injection, which delivers a significant 23 MW of power through multiple beam lines. Additionally, electron cyclotron heating provides 3.7 MW for localized heating and adjusting power levels.[5,116]

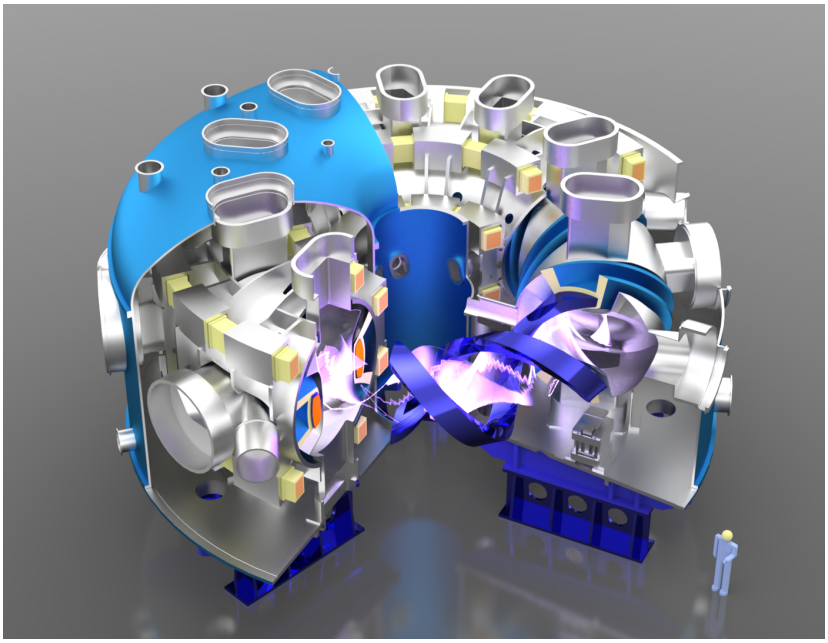

Figure 2.1: A diagram of the LHD. Image taken from Ref. 5

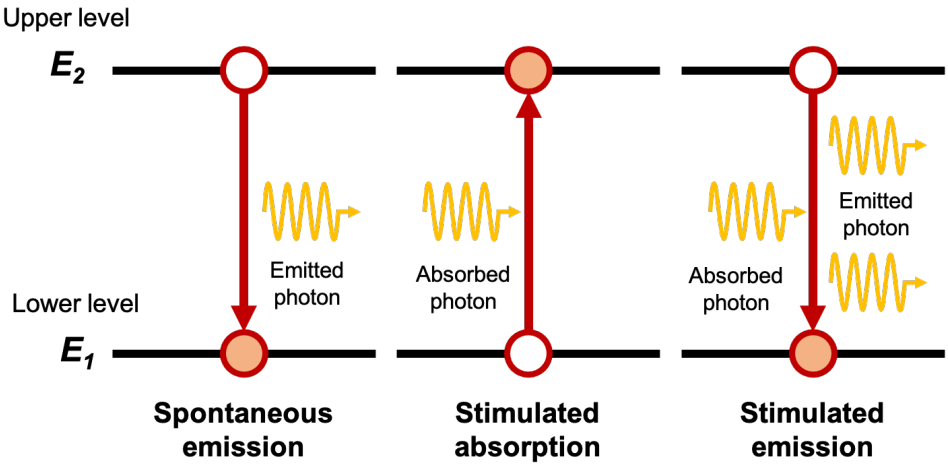

Figure 2.2: Three Radiative Transitions

2.4 Optical spectroscopy

Optical spectroscopic techniques measure the intensity of radiation emitted through three main processes involving quantum energy levels: spontaneous emission, absorption, and stimulated emission, as illustrated in Figure 2.2. Spontaneous emission occurs when an excited species at a higher energy level j releases a photon as it decays to a lower energy level i. Absorption takes place when a photon is absorbed, causing a species to move from levels i to j. In stimulated emission, a photon interacts with an excited species at a higher level j, inducing its transition to level i and emit a photon that is identical to the incoming photon.[50]

The wavelength of the intensity emitted in a spontaneous emission process is calculated from the energy E of the photon emitted by

$$\lambda = \frac{hc}{E}, \tag{2.2}$$

Here, h is the Planck's constant and c is the speed of light. E is given by the difference of E_j or the energy of the excited species at upper level j and E_i or the energy of the the species at lower level i as given by

$$E = E_j - E_i. \tag{2.3}$$

On the other hand, the absolute line intensity I_{ji} in units of photons ($m^3 s^{-1}$) is given by

$$I_{ji} = A_{ji} N_j \tag{2.4}$$

where A_{ij} is the Einstein-A coefficient (see Section 4.2.3.3) and N_j is the number density of species at the higher level j. This shows that the spectral data can be used as a method to calculate N_j. The line intensity can also be calculated in units of $W m^2 sr^{-1}$ using the line emission coefficient given by

$$\varepsilon_{ji} = N_j A_{ji} \frac{hc}{4\pi\lambda_0} \tag{2.5}$$

where 4π is the solid angle $d\Omega$ in steradians.[117]

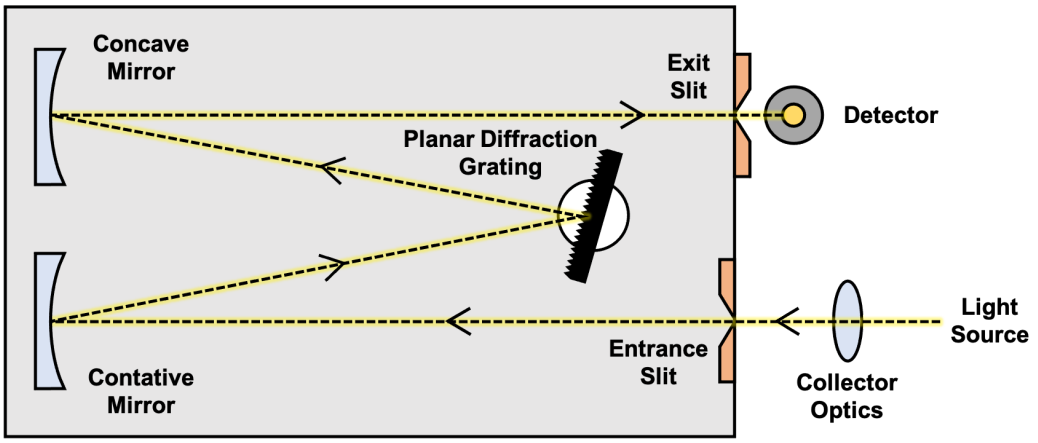

Figure 2.3: Schematics of a typical dispersive spectrometer. Figure adapted from Ref. 6

In optical emission spectroscopy, the focal wavelength range typically lies within the visible spectrum, from 380 to 780 nm. In this range, both the surrounding air and quartz glass remain transparent, enabling radiation to exit the chamber without distortion. To the naked eye, this radiation appears pink for argon or helium gas, red for neon, and purple for hydrogen.[117,118]

2.4.1 Spectrometers

Optical spectrometers are available in several types, each tailored for specific tasks and spectral ranges. Dispersive spectrometers, the most common type, use elements such as prisms or diffraction gratings to split light into its constituent wavelengths. Prism spectrometers rely on differences in refractive indices, while grating spectrometers utilize diffraction properties for dispersion. Interferometric spectrometers constitute another significant category, measuring spectral information through interference patterns. Examples

include Fabry–Pérot and Michelson interferometers, which manipulate light through multiple reflections or beam splitting and recombination.[119]

Filter-based spectrometers employ absorption or interference filters to isolate specific wavelengths for analysis. FTIR (Fourier Transform Infrared) spectrometers employ interferometry to simultaneously measure a broad range of wavelengths after light passes through a sample.

Each type of spectrometer has distinct advantages and limitations, with selection criteria including desired spectral range, resolution, sensitivity, and sample characteristics. Ongoing technological advancements continually enhance spectrometer sophistication and capabilities, driving progress in scientific research and industrial applications.[119]

2.4.2 Calibration

Calibration is a crucial step in ensuring the accuracy and reliability of spectroscopic measurements. Two main aspects of calibration are the calibration of the wavelength axis and the intensity axis. Wavelength calibration involves comparing measured values with known values using spectral lamps and wavelength tables, facilitating the verification of the grating angular position and wavelength designation to individual pixels.[117,120] On the other hand, intensity calibration can be either relative or absolute. For the calibration of intensity axis, it can either be an absolute or a relative calibration. In relative calibration, the spectral sensitivity of the system is calibrated along the wavelength axis. Absolute calibration on the other hand, converts the intensity

signals (usually given in counts or voltage) to Wm^2sr^{-1} or photons as given in Eq. 2.4 and 2.5 which allows calculation of parameters such as N_q. However, in absolute calibration, imaging of the plasma tends to be tedious as the solid angle needs to be conserved.[117] In relative calibration, the solid angle parameter is cancelled out.

2.4.3 Dispersive Spectrometers

As illustrated in Figure 2.3, dispersive spectrometers typically consist of an entrance slit, a dispersing element (usually prisms or gratings), an optical system, and a detector at the exit slit.[121,122] These spectrometers work by separating incoming radiation into its spectral components. The optical system captures an image of the plasma and disperses it into a spectrum at the entrance, often using optical fibers. The choice of grating determines the spectral resolution—the finer the grating, the clearer the spectrum. The entrance slit controls how much light enters, affecting optical resolution. Once through the entrance slit, the light beam spreads out and is straightened by a collimating mirror before hitting the diffraction grating (or prism). This component splits the light into its wavelengths through diffraction. Echelle gratings, a specific type, offer especially high spectral resolution. The detector at the exit slit, typically a photomultiplier tube (PMT) or a charge-coupled device (CCD) array, also impacts the system's sensitivity. PMT-based systems scan the spectrum, with the exit slit width affecting resolution, while CCD arrays record a specific wavelength range, with pixel size influencing resolution.[117,118,121–124]

2.4.4 Spatial heterodyne spectrometer (SHS)

An SHS operates similarly to a Michelson interferometer but utilizes diffraction gratings instead of mirrors. This allows the spectrometer to spatially encode spectral data, providing advantages in simplicity, stability, and sensitivity. It also incorporates prisms to widen the field of view and utilizes high-order diffraction gratings to enhance its capabilities for various applications. It is commonly employed in fields like astrophysics, planetary exploration, and atmospheric spectroscopy. The core principle of the SHS involves directing light from a source, splitting it into two paths using diffraction gratings, dispersing the light, then recombining it to generate Fizeau fringes. These fringes, captured by an imaging detector, encode wavelength-specific information into a spatial interferogram. Fourier transformation of this interferogram allows for spectrum recovery.[99,100,119]

2.4.5 Charge exchange spectroscopy (CXS)

CXS is characterized by the charge transfer from the impurity ions in the plasma to the neutral atoms coming from the neutral beam, leaving the impurity ion in the excited state.[125] For a fully ionized carbon, this reaction is given by

$$H^0_{beam} + C^{6+} \rightarrow H^+ + C^{5+}(n = 8). \tag{2.6}$$

The spontaneous emission of the excited impurity ion given by C^{5+}(n = 8 $\rightarrow$ 7) emits light at $\lambda = 529.05$ nm. This emitted radiation can then be measured

by the spectrometer. From the Doppler broadening and Doppler shift of the spectral line, the $T_{C^{6+}}$ and the V_f can be calculated.

Chapter 3

Experimental set-ups

In this section, the experimental details for the RF CCP and the SHS configuration in the LHD are discussed.

3.1 Radiofrequency CCP set-up

The OES intensity measurements were conducted in the Budapest v.3 Cell.[126] This RF CCP set-up consists of geometrically highly symmetric plane-parallel electrode CCP source that makes the experiments compatible with one-dimensional (1D) PIC/MCC simulation. In this system, the DC self-bias is estimated to be about 1% of the amplitude of the RF excitation voltage.The electrodes each having a diameter of 14.2 cm are set 4 cm apart and enclosed in a quartz cell. The chamber is evacuated to a base pressure of 10^{-5} Pa using a turbomolecular and a rotary pump. Argon gas is introduced at a flow rate of 1 sccm using a mass flow controller, with a needle valve on the pump side allowing fine control of the gas pressure, monitored by a capacitive gauge (Pfeiffer Vacuum CMR264). Measurements were taken across a pressure range of 2 to 100 Pa.

The upper electrode is powered by a 13.56 MHz generator (Tokyo HY-Power RF-150) through a matching network (Tokyo HY-Power MB-300), while the lower electrode is grounded. The RF voltage, maintained at a peak-to-

peak value of 300 V, is monitored near the electrode by a Solayl Vigilant RF Voltage-Current Probe. To ensure accuracy, sufficient time was allowed for the electrodes to reach a stable temperature after any change in gas pressure, with recent studies[127] indicating thermalization times of approximately 30-40 minutes. A diagram of the experimental setup is shown in Figure 3.1.

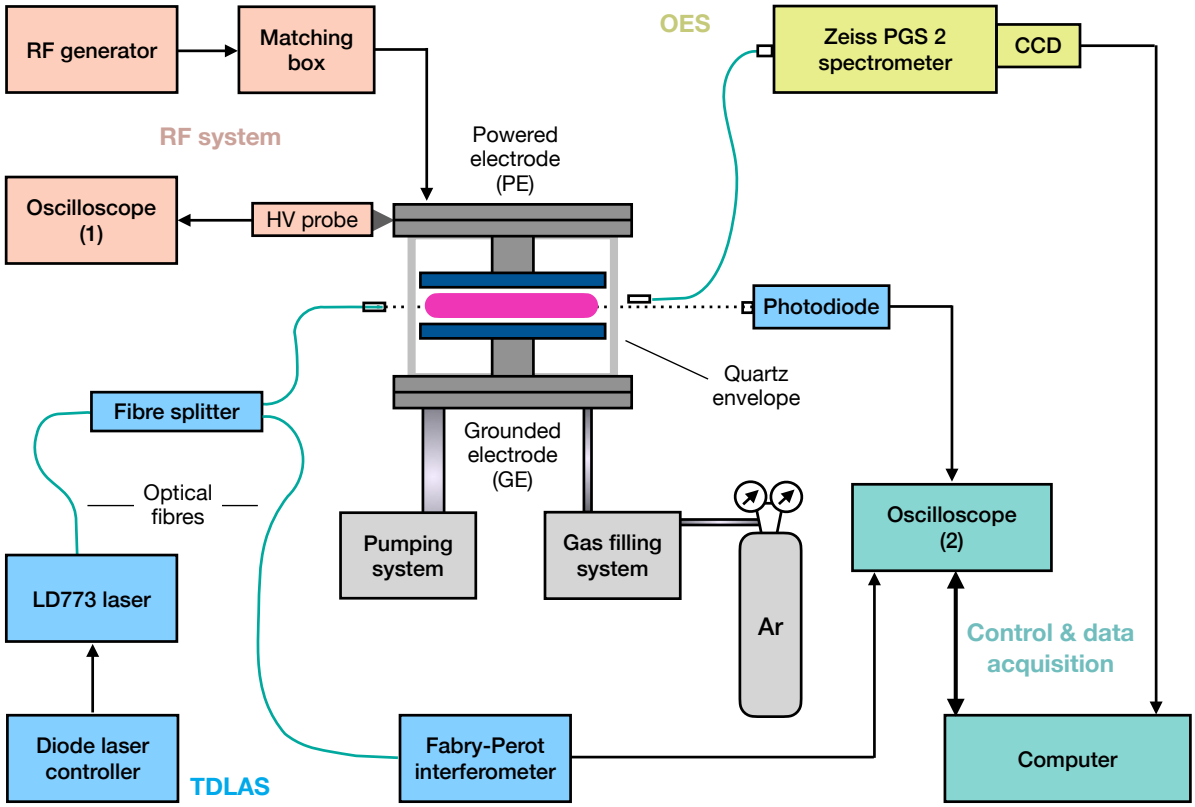

Figure 3.1: Schematic diagram of the experimental set-up for the TDLAS and OES measurements.

3.1.1 OES measurements set-up

In the OES experiments, a Carl Zeiss Jena PGS-2 spectrometer equipped with an APHALAS CCD-S3600-D-UV detector is used for the measurement

of the intensities of selected spectral lines belonging to the set of 2p $\rightarrow$ 1s (Paschen notation) transitions in the 696 - 826 nm wavelength domain. The procedure involves capturing the narrow spectral segments around the emission lines of interest. In this way the line intensities are recorded without taking complete spectra of the discharge. The wavelength-dependent sensitivity of the spectrometer is determined using an RS-15 Total Flux Calibration Light Source having a certified calibration report (that specifies the radiant flux of the lamp as a function of the wavelength in the range between 300 nm and 1100 nm) provided by Gamma Scientific. This calibration procedure is based on the measurement of the intensity of the radiation emitted by this lamp (at the conditions 12 V, 8.333 A), with the same optical components (including the quartz cylinder, fiber collimator lens, and fiber optic cable) as in the plasma OES measurements. Comparison of the measured intensity as a function of the wavelength with the certified calibration report data of the lamp allows us to derive the wavelength-dependent calibration factor that needs to be applied to the measured plasma OES recordings to eliminate the overall wavelength dependence of the sensitivity. No attempt is made to accomplish an absolute intensity calibration of the system. The OES measurements capture the light from the central, $\approx$1 cm-diameter region of the plasma, with the fiber oriented perpendicularly to the principal axis of the discharge.

Due to the relatively low intensity of some of the lines, the slit of the spectrometer is set to 100 μm. The spectral resolution achieved this way still allows for the separation of the closely-situated peaks 750.4 nm and 751.5 nm,

as well as 800.6 nm and 801.5 nm. However, the 772.38 nm and 772.42 nm lines are unresolved and the measured intensity values in this case represent the sum of the intensities of these two lines.

3.1.2 Tunable Diode Laser Absorption Spectroscopy

Tunable Diode Laser Absorption Spectroscopy (TDLAS) is applied to obtain the gas temperature and the density of the $1s_5$ metastable Ar atoms.[128–131] The approach relies on the determination of the absorption on a selected spectral line over which the laser wavelength is scanned through. In our case, we use the transition Ar($1s_5 \rightarrow 2p_6$) at a wavelength of 772.376 nm.

In the experimental setup the beam of a laser diode (Toptica LD-0773-0075-DFB-1) driven by a control unit (Toptica DLC DFB PRO L) is coupled into an optical fiber, and then transferred to a splitter so that only 10% of the laser power is directed towards the plasma reactor. It passes through the middle of the plasma horizontally and is detected at the other side of the chamber by a photodiode. The remaining 90% of the power enters an Fabry–Pérot interferometer (FPI) for wavelength calibration. Both the signal transmitted through the plasma and the reference signal of the FPI are recorded by an oscilloscope (Oscilloscope (2) in Fig. 3.1), which communicates with a computer that runs a LabVIEW control and data acquisition program. To perform proper background subtraction, detector signals are recorded with and without discharge, both with laser on and off states. Assuming a dominating Doppler broadening with a Gaussian spectral profile, the amplitude of the absorption provides

information about the line-integrated metastable density, while the width of the line conveys information about the gas temperature. For a more detailed description, the reader is referred to a recent publication of Ref. 132.

The Ar gas temperature T_g thus measured for the RF-driven Ar CCPs under our experimental conditions is plotted as a function of the gas pressure in Fig. 3.2. A best-fit line has been incorporated into the figure as a guide to the eye and as a measure for the scattering of the measured T_g values. The gas temperature data are used in the numerical simulations to have a better correspondence with the actual experimental conditions. The measured metastable density values obtained from TDLAS are compared with those obtained from the numerical simulations and thus will be presented later.

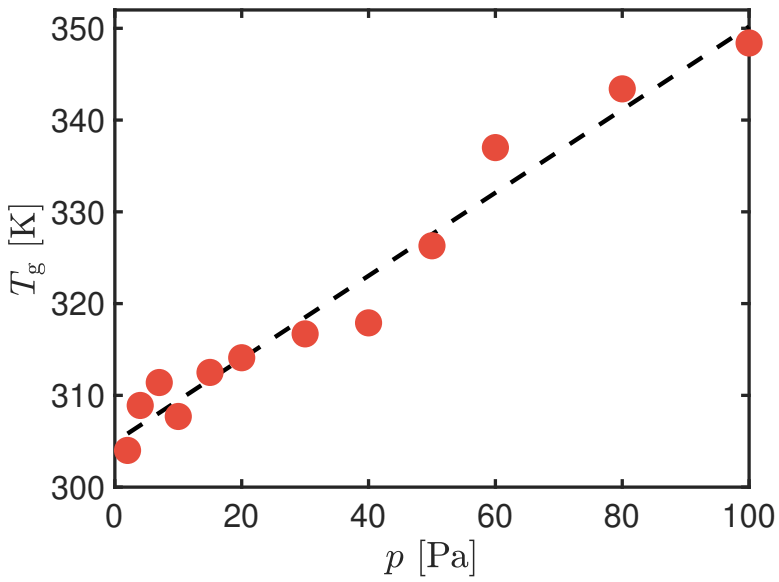

Figure 3.2: Gas temperature T_g of RF-driven Ar CCPs under our experimental conditions obtained from TDLAS as a function of the Ar gas pressure. The dashed curve is only a guide to the eye.

3.2 LHD set-up

3.2.1 SHS in LHD

Fig. 3.3(a) shows the schematic view of the LHD with the line-of-sight (LOS) of the DS and SHS systems. The LHD is a heliotron device consisting of three tangential beams (neutral beam (NB)#1-3) and two perpendicular beams (NB#4-5). The SHS is connected to the lens located at the viewing port 9-O. The NB#5, which is located at port 1-O, is used to induce the charge exchange reaction corresponding to the SHS measurements. NB#5 is oriented perpendicular to the magnetic flux surface along the major radius. Using mirrors, the LOS of the lens at port 9-O was arranged such that it intersected with NB#5 at an angle of 113.6°. The intersecting region spans from the magnetic axis to the outboard edge of the LHD plasma. However, in this study, SHS measurements were only done in the portion of the intersecting region near the magnetic axis, that is, at R = 3.66 m. The SHS was placed on an anti-vibration table to increase resilience to vibrations.

Charge exchange between fully ionized carbons and thermal neutrals in the plasma produces light emission which overlaps the wavelength range of the target emission. To measure the background emission coming from this charge exchange with the thermal neutrals, NB#5 was modulated on and off. The background emission corresponded to the intensity measured when the beam was off.

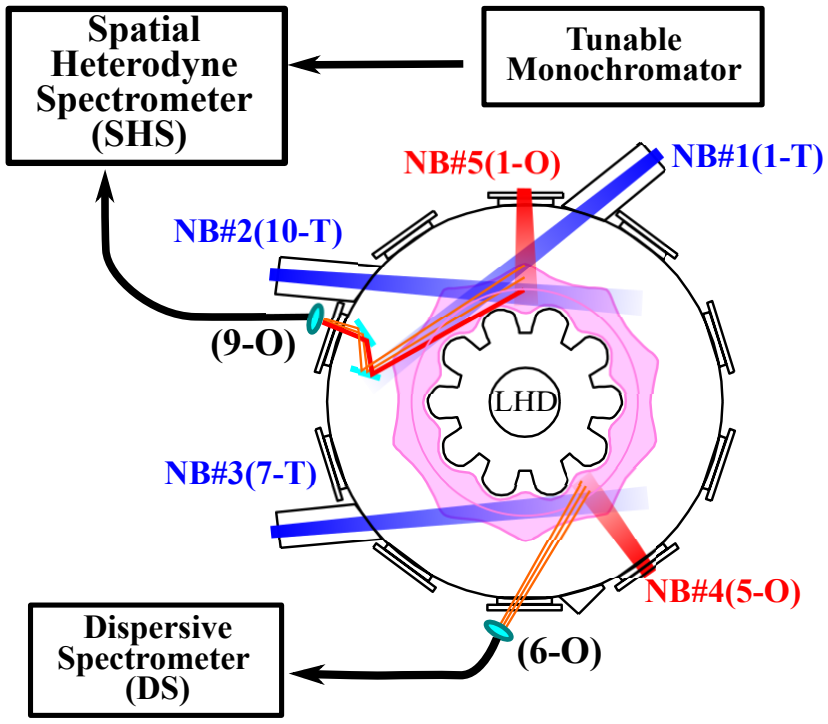

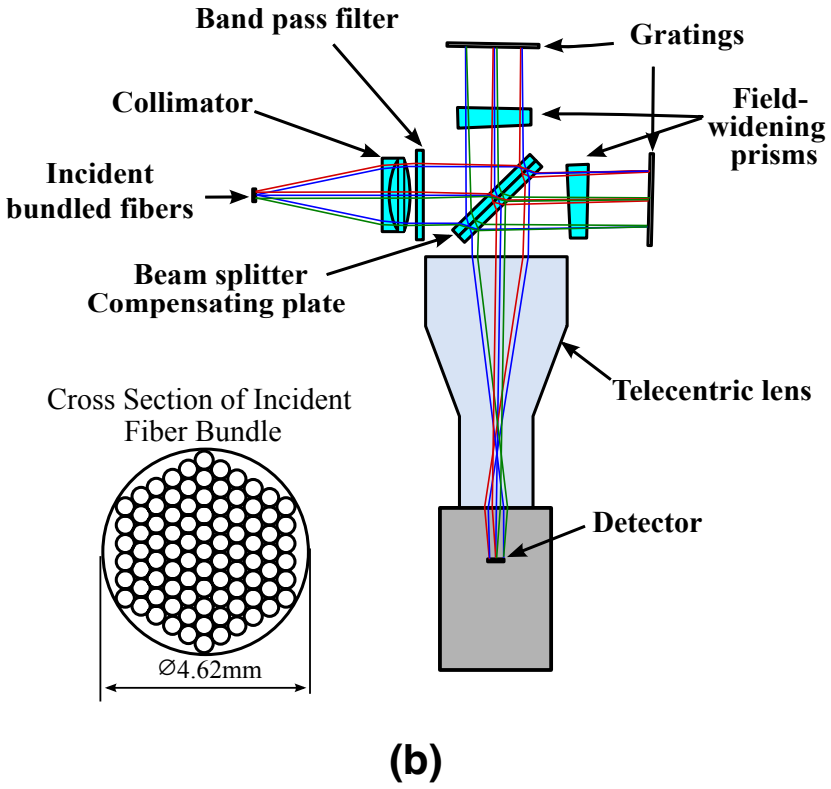

Figure 3.3: (a) SHS and DS configuration in the LHD and (b) the schematic diagram of SHS

For comparison purposes, the intensity of the charge exchange line collected using a DS (Bunkoukeiki Co., Ltd. CLP-400) was also measured. The DS is located at port 6-O, wherein the neutral beam CXS (NBCXS) is induced by NB#4. The LOS of the DS intersects with the NB#4 at an angle of 103°. Similar to the SHS measurements, the DS measurements used in this study were those measured at R = 3.66 m.

3.2.2 SHS set-up

The set-up of an SHS is fundamentally similar to a Michelson interferometer, but with diffraction gratings instead of mirrors. A schematic diagram of the SHS (Bunkoukeiki Co., Ltd. BSH-529P) used in this experiment is shown in Fig. 3.3(b).

The light collected by the lens at the LHD port 9-O is directed to the SHS fiber bundle. This fiber bundle contains 91 fiber cores with a bundle diameter of 4.62 mm. The divergent incident light is then collimated by an achromatic collimator lens and guided to a three-cavity band pass filter centered at 529.0 nm. After that, the light beam is split into two by the beam splitter and the resulting beams are directed to the two gratings. The synthetic quartz compensating plate on the beam splitter was compensated for the variation of optical path induced in one arm. Field widening prisms are inserted between the splitter and the gratings. Upon reaching the gratings, light is diffracted at an angle that is dependent on the wavelength. At a wavelength called the Littrow wavelength, light is returned to the same direction of incidence. The angle of

the tilt of the gratings with respect to the optical axis is called the Littrow angle. The SHS used in this study has a tunable Littrow wavelength.

On the way to the detector, light is made to pass through a telecentric lens to reduce perspective errors. For each wavelength that goes through the filter, two wavefronts with a wavelength-dependent crossing angle in between them reach the detector. The superposition of these two wavefronts leads to the formation of a Fizeau fringe pattern. The spatial frequency of the Fizeau pattern is dependent on the corresponding wavelength.

3.2.2.1 SHS Calibration

To calibrate the SHS, the intensity of the light coming from a tunable wavelength monochromatic light source (TLS) was measured and transformed into spectra. The wavelength of the TLS was tuned from 527-530.8 nm. The spectrum line width of the monochromatic light can be varied by changing the width of the exit slit of the TLS. Fig. 3.4(a)-(c) shows the Fizeau fringe image produced at the detector from the light at 528 nm, 529 nm, and 530 nm. Here, the spatial frequency of the fringe patterns is observed to decrease with increasing wavelength. The spectra given in Fig. 3.4(d) are then derived from the fast Fourier transform (FFT) of these fringe patterns. It can be observed from Fig. 3.4(d) that distinct peaks were successfully measured at each specific wavelength value. A zero spatial frequency was measured at 530.8 nm, setting it as the Littrow wavelength.

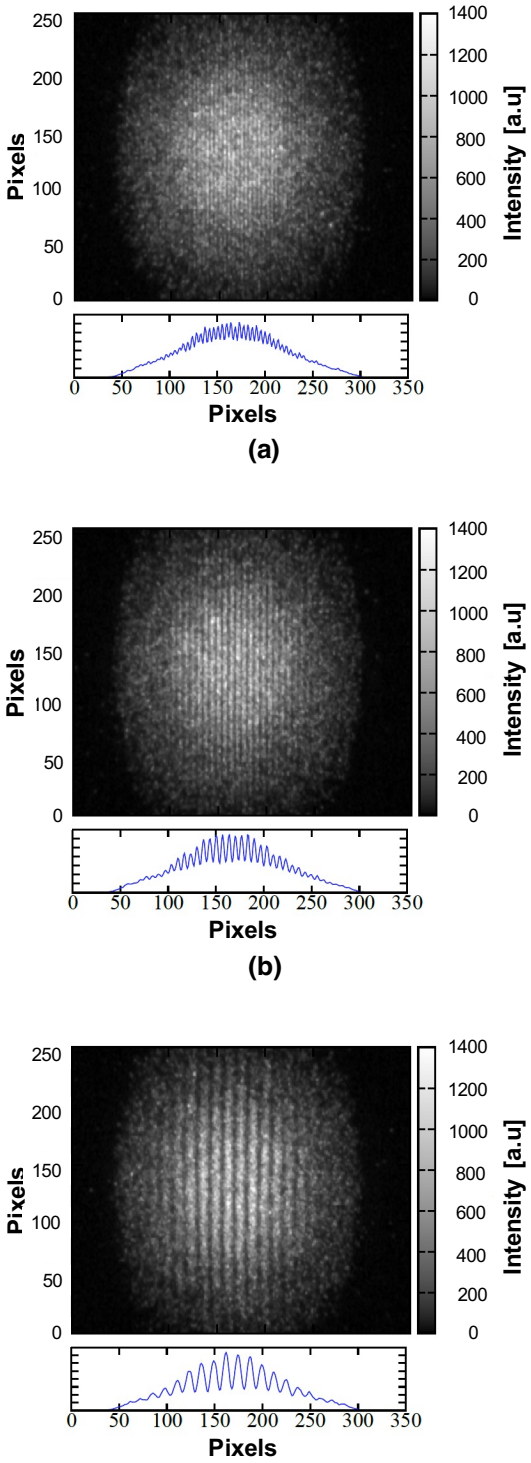

Figure 3.4: Measured fringe patterns at (a) 528 nm, (b) 529 nm, and (c) 530 nm

Chapter 4

Simulation Methods

4.1 PIC/MCC simulation

The distribution function $f(r, v, t)$ is fundamental quantity describing the behavior of a given species and represents the number of particles within a six-dimensional phase space (r, v) at time t. For collisional plasmas, this can be expressed using the Boltzmann Equation:[80,133]

$$[\frac{\partial}{\partial t} + a \cdot \nabla_v + v \cdot \nabla_r] f(r, v, t) = (\frac{\partial f}{\partial t})_{coll} \tag{4.1}$$

where a is the acceleration and $(\frac{\partial f}{\partial t})_{coll}$ is the collision term accounting for collision effects. The gradients taken in velocity space ∇_v and real space ∇_r are given by

$$\nabla_r = \hat{x}\frac{\partial}{\partial x} + \hat{y}\frac{\partial}{\partial y} + \hat{z}\frac{\partial}{\partial z} \tag{4.2}$$

$$\nabla_v = \hat{x}\frac{\partial}{\partial v_x} + \hat{y}\frac{\partial}{\partial v_y} + \hat{z}\frac{\partial}{\partial v_z} \tag{4.3}$$

Solving the Boltzmann equation (BE) can be complex and often necessitates approximations, such as the two-term approximation. One approach to solve it involves deriving moments of the BE, leading to macroscopic fluid equations. These equations, commonly used to simulate high-pressure plas-

mas with complex chemistry, depend on the drift-diffusion approximation for solving BE moments but have difficulty accurately modeling nonlocal and nonlinear effects.[134]

An alternative to solving the BE is using particle simulation methods, which can solve for the distribution function by tracking individual particles in the plasma.[80] The most prevalent particle simulation method is the Particle-in-Cell/Monte Carlo Collision (PIC/MCC) method, which employs two main approaches. The first approach uses a spatial numerical grid to solve the equations of motion and Poisson's equation, thereby avoiding the need to account for pairwise particle interactions.[134,135] The second approach uses superparticles, which represent groups of real particles, significantly reducing the number of particles to a manageable level.[80] Since the distance between particles is much smaller than both the typical molecular diameter and the de Broglie wavelength, RF CCP particle simulations primarily adhere to classical principles. Furthermore, with no external magnetic field applied and the skin effect only appearing in specific scenarios, these simulations are typically considered electrostatic.[118,134]

4.1.1 PIC/MCC simulation elementary steps

An electrostatic PIC/MCC simulation works by tracking the charged particles (i.e. electrons and ions) in the plasma and calculating how the electric field and collisions affects the particles. Figure 4.1 shows the elementary steps followed in an electrostatic PIC/MCC cycle.[88]

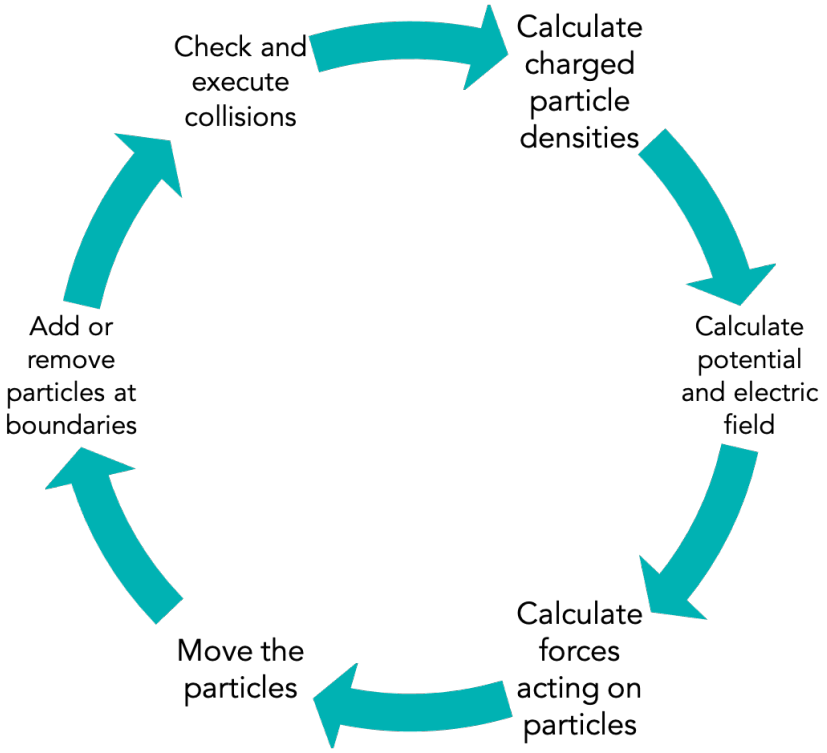

Figure 4.1: Elementary steps in a PIC/MCC simulation

Initially, the superparticles have a random spatial distribution inside the discharge gap. The numerical grid is divided into equidistant gridpoints by with distance Δx in between,

$$\Delta x = \frac{L}{N}. \tag{4.4}$$

Here, L is the length of the discharge gap and N is the number of gridpoints.

4.1.1.1 Calculate charged particle densities

The first step in a PIC/MCC cycle is calculating the densities on each grid points from nearby particles. The densities are assigned by a method called weighting. In this method, the densiies are assigned to surrounding grid points

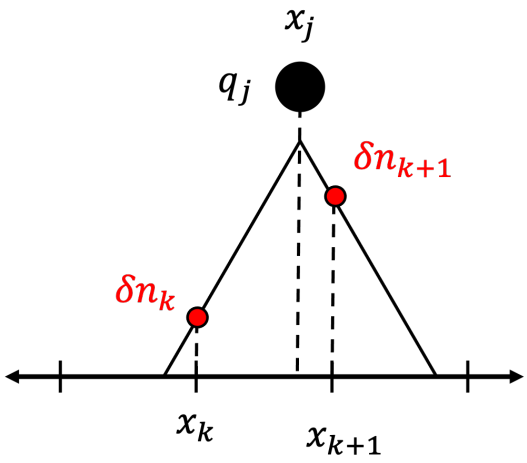

Figure 4.2: Assigning density to grid points through particle weighting in a 1D simulation

based on the distance between the particle and the grid point,[136] as shown in Figure 4.2.

If particle a located at x_a has a density of q_a, q_a will be divided to the surrounding grid points x_b and x_{b+1} by

$$\delta n_b = ((b+1)\Delta x - x_a)\frac{W}{A\Delta x^2} \tag{4.5}$$

$$\delta n_{b+1} = (x_b - k\Delta x)\frac{W}{A\Delta x^2} \tag{4.6}$$

where δn_b, δn_{b+1} gives the charged particle densities calculated at grid point k, W is the weight of a superparticle or the number of real particles represented by a superparticle, and A is the surface area of the electrode.

The corresponding charge density at grid point b, denoted as ρ_b is then calculated by

$$\rho_k = e(n_{i,b} - n_{e,b}). \tag{4.7}$$

where $n_{i,b}$ and $n_{e,b}$ are the densities of the single charge positive and negative ions and e is the elementary charge.

4.1.1.2 Calculate potential and electric field

From the charge distribution, potential ϕ is calculated from the charge density ρ using the Poisson's equation given by[80]

$$\nabla^2\phi = -\frac{\rho}{\varepsilon_0} \tag{4.8}$$

where ε_0 is the permittivity in free space with the value $8.854 \times 10{-}12\mathrm{Fm}^{-1}$. To implement Eq. (4.8) at the grid points x_k and x_{k+1}, finite difference is applied to obtain a discrete Poisson's equation given by[135]

$$\frac{\phi_{b+1} - 2\phi_b + \phi_{b-1}}{\Delta x^2} = \frac{\rho_b}{\varepsilon_0}. \tag{4.9}$$

Since the upper electrode ($b = 1$) is powered and the lower electrode ($b = N$) is grounded, potential difference between the electrodes is taken into account by implementing boundary conditions given by

$$\phi_1 = Vcos(2\pi ft) \tag{4.10}$$

$$\phi_N = 0 \tag{4.11}$$

where V is the peak amplitude of the voltage applied and f is the frequency of the power applied. Using Gauss's Law and Poisson's equation, electric field E

can be expressed by

$$E = -\nabla\phi. \tag{4.12}$$

Electric field at grid point x_b and at the boundaries are therefore given by

$$E_b = -\frac{\phi_{b+1} - \phi_{b-1}}{2\Delta x} \tag{4.13}$$

$$E_1 = \frac{\phi_1 - \phi_2}{\Delta x} - \rho_0 \frac{\Delta x}{2\varepsilon_0} \tag{4.14}$$

$$E_N = \frac{\phi_{N-1} - \phi_N}{\Delta x} + \rho_N \frac{\Delta x}{2\varepsilon_0}. \tag{4.15}$$

4.1.1.3 Calculate forces acting on particles

After calculating the electric field at grid point x_b, it is then applied back to the particle *a* using

$$E(x_a) = \frac{(b+1)\Delta x - x_a}{\Delta x} E(x_b) + \frac{x_a - b\Delta x}{\Delta x} E(x_{b+1}). \tag{4.16}$$

The force F exerted back on the particle is therefore

$$F_a = q_a E(x_a). \tag{4.17}$$

4.1.1.4 Move the particles

Due to the force applied, the particles are then given a new position and new velocity using the equations of motion[136]

$$m\frac{dv}{dt} = F \tag{4.18}$$

$$\frac{dx}{dt} = v \tag{4.19}$$

which are implemented through an integration scheme called the leap frog method. In this method, the particle position is calculated at integer time steps, while velocity is calculated at half-integer time steps ($\Delta t/2$)[135] as given by

$$\frac{v(t+\Delta t/2) - v(t-\Delta t/2)}{\Delta t} = \frac{q}{m}E(t) \tag{4.20}$$

$$\frac{x(t+\Delta t) - x(t)}{\Delta t} = v(t+\Delta t/2) \tag{4.21}$$

Since ions are much heavier than electrons, ions tend to move much slower. To address the extended time required to move ions, ion subcycling is used to ease computational demands. This method involves solving the equations of motion for ions less frequently compared to electrons. In this code, one electron time step matches a single RF cycle, whereas one ion time step corresponds to 20 electron time steps.

4.1.1.5 Add or remove particles at boundaries

After moving the particles, it is essential to verify if any have reached the electrodes or the walls. The boundary conditions that apply will vary based on which particles have exited the computational domain.

When an ion exits the domain, it may either be absorbed or it may trigger the emission of secondary electrons. If it is absorbed by the walls, the ion is simply removed from the ensemble. However, if it causes secondary electron emission, the ion is removed, and an additional electron is added to the system. This process involves comparing a randomly generated number to the pre-established secondary electron emission coefficient (SEEC) of the electrodes. Typically, the SEEC is assumed to be constant, regardless of the incident angle and energy of the particle.[137] In this implementation, a constant ion-induced SEEC of 0.07 is used, based on research indicating that SEEC generally remains around this value for ion energies below 1000 eV.[138]

Electrons, on the other hand, may either be absorbed or reflected when they exit the domain. Absorption results in the electron being removed from the system, while reflection involves the electron being elastically backscattered into the system. In this model, a constant electron reflection coefficient of 0.5 is used. The decision between absorption and reflection is made by comparing a randomly generated number to 0.5, similar to the process used for determining secondary electron emission.[118,139]

4.1.1.6 Check and execute collisions

The last step is to check if each particle experienced a collision after moving. The probability P_a that particle *a* undergoes a collision after a time step Δt is given by[74]

$$P_a = 1 - \exp[-n_{\mathrm{gs}}\sigma_{\mathrm{T}}(\varepsilon)v_a^{\mathrm{rel}}\Delta t]. \tag{4.22}$$

Here, n_{gs} refers to the density of the ground state Ar atom colliding with particle a, σ_{T} refers to the energy-dependent total cross section of particle *j*, and v_a^{rel} is the relative velocity of particle of the collision partners. For ion-atom collisions, v_a^{rel} is determined by randomly sampling a potential collision partner from the ensemble of thermal background gas atoms. In electron-atom collisions, due to the large difference in mass the target atoms are assumed to be stationary, following the 'cold-gas approximation'. A collision occurs if the randomly generated number is smaller than P_a.

In most Ar PIC/MCC simulations, we only trace the e^- and Ar^+ ions. However, we assume a homogenous background ground state Ar atoms, and the collisions of the charged particles with these ground state atoms are considered. Appendix C gives the list of reactions included in this model. Except for the ion-atom collisions, all cross-sections are taken from the Hayashi database in LXCat.[4] The isotropic and backscattering ion-atom cross-sections are obtained from Ref. 3.

4.1.2 Constraints

For most simulation techniques, achieving a balance between accuracy and speed is necessary. Therefore, in this study, we implemented specific parameter constraints in the PIC/MCC simulations in order to meet stability and accuracy criteria. This includes[80,134]

1. $\Delta x \approx \lambda_D$

   The Debye length (λ_D) is a key parameter in plasma, defining the shielding distance around a test charge where significant charge densities can exist. At a scale length less than λ_D, particle-particle effects are strongest and at distances greater than λ_D, collective effects dominate.[133,136] λ_D can be calculated by

   $$\lambda = \sqrt{\frac{\epsilon_0 T_e}{e n_e}} \tag{4.23}$$

   The spatial grid resolution must resolve phenomena up to the Debye length scale to prevent numerical heating due to finite grid instability.[140]

2. $\omega_p \delta t \leq 1$

   This constraint dictates that the time step Δt must be less than the inverse of the electron plasma frequency ω_p, which is defined as

   $$\omega_p = \sqrt{\frac{n e^2}{\varepsilon_0 m}}. \tag{4.24}$$

Therefore, $\Delta t < \omega^{-1}$. However, the leapfrog scheme mentioned in Section 4.1.1.4 is found to be numerically unstable when $\omega_p \delta t \geq 2$. Stability may be achieved at $1 \leq \omega_p \delta t \leq 2$, although this can result to significant numerical errors.[141] Therefore in this study, a constraint of $\omega_p \delta t \leq 0.2$ is maintained.

3. $\nu_{max} \Delta t \leq \Delta x$

This constraint is known as the Courant condition, which states that the individual particles must not travel a distance greater than Δx within a single time step to ensure proper charge assignment.[80] Here, ν_{max} denotes the maximum velocity of a charged particle.

4. $N_D >> 1$

Here, N_D is the number of particles in a Debye sphere. This constraint ensures that at least one superparticle is present in a Debye sphere and that there are enough superparticles present in a grid cell to maintain good statistical accuracy in the simulation.[80,134]

5. $P_a \leq 0.05$

This constraint assures that the collision probability P_a is kept below 0.05. By doing so, particle j will not experience more than one collision per time step, preventing the simulation from missing any collisions.[?,80,118,135]

4.2 Collisional-Radiative Model

Each spectral line measured in the spectra represents the radiative transition from a higher excited state level to a lower level. The intensity of this

spectral line is determined by the number density of the upper level, which is influenced by both the electron temperature and density.[59] A CRM encompasses a set of rate equations that describe the populating and depopulating processes—both collisional and radiative—of an excited state in a steady-state plasma. These equations enable the calculation of the density of excited species in each state.[58] By determining the number of excited species undergoing spontaneous emission, the spectral lines of an emission spectrum can be modeled. In this study, PIC/MCC combined with CRM was used to model specific spectral lines in the Ar emission spectrum.

4.2.1 Notations

Throughout this work, Paschen's notation is used. The Paschen's notation is an attempt to align the neon emission spectrum with hydrogen-like theory, thus using n' instead of the principal quantum number n. Each quantum level is denoted by $n'l_w$. In this system, the 4s states are labeled as 1s, and the 4p states are labeled as 2p. Here, l represents the angular momentum quantum number, and w indicates the order of energy levels within the orbital in descending order. For the 1s orbital, w = 5 represents the lowest energy level ($1s_5$) and w = 2 the highest ($1s_2$), while for the 2p orbital, w = 10 is the lowest energy level ($2p_{10}$) and w = 1 the highest ($2p_1$).

4.2.2 CRM used in this work

The numerical simulation code of the CRM developed in this study was derived from the work of Siepa *et al.*[58] The new code can take the EEDF obtained from PIC/MCC simulations as input information. The CRM calculates the population densities of the first 14 excited states of an Ar atom (1s and 2p states in Paschen's notation), which are given in Fig. 4.3 and Appendix B. For each of the excited state levels, it solves the following balance equations.

For Ar atoms in the 1s metastable states m, namely the $1s_5$ or $1s_3$, we have

$$\begin{aligned} & n_{\mathrm{gs}} Q_{\mathrm{gs}\to m} n_{\mathrm{e}} + n_{\mathrm{e}} \sum_{\substack{a=1\mathrm{s},2\mathrm{p} \\ a\neq m}} n_a Q_{a\to m} + \sum_{a=2\mathrm{p}} n_a A_{a\to m}\eta_{m\to a} \\ =& \left[(Q_{m\to\mathrm{gs}} + \sum_{\substack{a=1\mathrm{s},2\mathrm{p} \\ a\neq m}} Q_{m\to a} + Q_{m\to\mathrm{ion}}) n_{\mathrm{e}} + \sum_{a=1\mathrm{s}} \alpha_{a,m} n_a (1+\delta_{a,m}) + \tau_m^{-1} \right] n_m \end{aligned} \quad (4.25)$$

For Ar atoms in the 1s resonant states r, namely the $1s_4$ or $1s_2$ state, we have

$$\begin{aligned} & n_{\mathrm{gs}} Q_{\mathrm{gs}\to r} n_{\mathrm{e}} + n_{\mathrm{e}} \sum_{\substack{a=1\mathrm{s},2\mathrm{p} \\ a\neq r}} n_a Q_{a\to r} + \sum_{a=2\mathrm{p}} n_a A_{a\to r}\eta_{r\to a} \\ =& \left[(Q_{r\to\mathrm{gs}} + \sum_{\substack{a=1\mathrm{s},2\mathrm{p} \\ a\neq r}} Q_{r\to a} + Q_{r\to\mathrm{ion}}) n_{\mathrm{e}} + \sum_{a=1\mathrm{s}} \alpha_{a,r} n_a (1+\delta_{a,r}) + A_{r\to\mathrm{gs}}\eta_{gs\to r} \right] n_r \end{aligned} \quad (4.26)$$

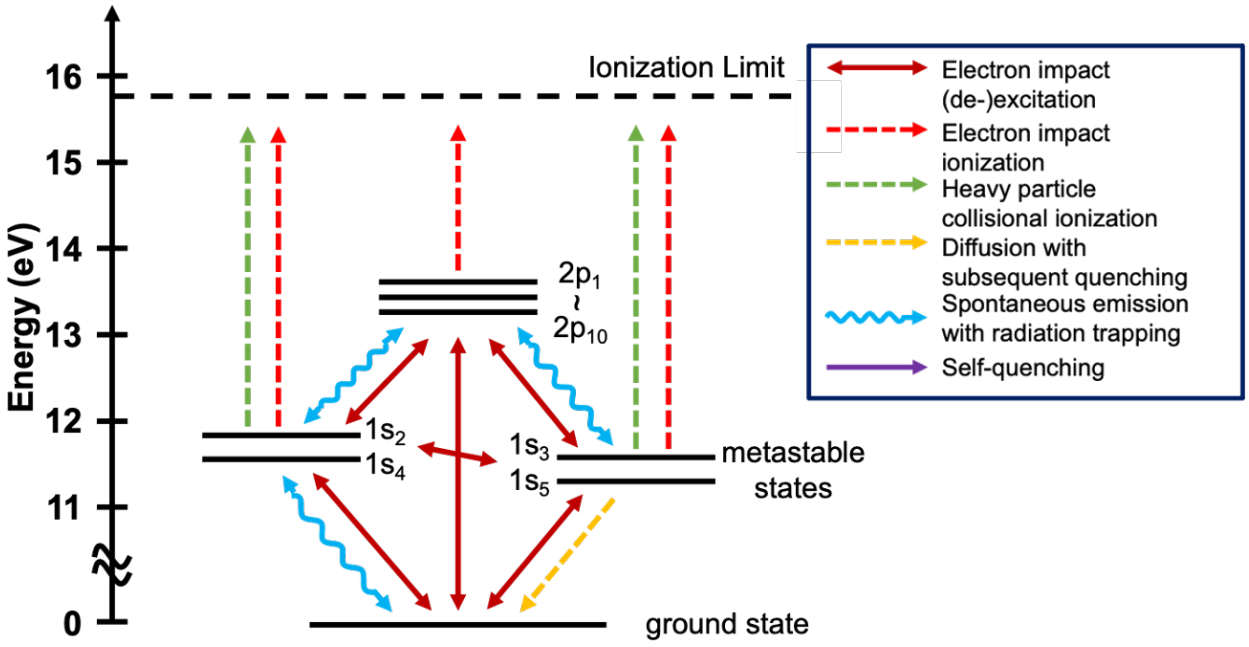

Figure 4.3: Processes included in this CRM

For Ar atoms in one of the 2p excited states, we have

$$n_{\rm gs}Q_{{\rm gs}\to 2p}n_{\rm e} + n_{\rm e}\sum_{a=1{\rm s}} n_{1s}Q_{1{\rm s}\to 2{\rm p}}$$
$$= \left[(Q_{2{\rm p}\to{\rm gs}} + \sum_{a=1{\rm s}} Q_{2{\rm p}\to a} + Q_{2{\rm p}\to{\rm ion}})n_{\rm e} + \sum_{a=1{\rm s}} A_{2{\rm p}\to a}\eta_{a\to 2p} + k_{{\rm q},2{\rm p}}n_{\rm gs}\right] n_{2{\rm p}}. \quad (4.27)$$

Here the subscripts "gs" and "ion" indicate that the corresponding values are those for the ground state of Ar atom and ions, $2p$ denotes any of the ten 2p states considered (e.g, $2{\rm p}_{10}$, $2{\rm p}_9$, $\cdots$, $2{\rm p}_1$), and n_a and $n_{\rm e}$ denotes the density of excited Ar atoms at level a and that of electrons. Among the various excited states, m refers to one of the metastable states (m = $1{\rm s}_5$ or $1{\rm s}_3$) and r denotes one of the resonant states (r = $1{\rm s}_4$ or $1{\rm s}_2$).

Table 4.1: Processes included in the CRM. Here 1s refers to one of the 1s states and 2p refers to one of the 2p states. The slash "/" refers to "or", e.g., "1s/2p" refers to one of the 1s or 2p states

Process name	Coefficient	Reactions	Equation	Reference
electron impact transitions from state i to state j	$Q_{i\to j}$	Ar(gs) + e $\leftrightarrow$ Ar(1s/2p) + e Ar(1s) + e $\leftrightarrow$ Ar(1s/2p) + e Ar(1s/2p) + e $\rightarrow$ Ar^+ + 2e	Eq. (4.28)-(4.31)	[142,143] [143] [144]
spontaneous emission from higher state j to lower state i with radiation trapping	$A_{j\to i}\ \eta_{i\to j}$	$Ar(1s_4/1s_2) \leftrightarrow Ar(gs) + h\nu$ $Ar(2p) \leftrightarrow Ar(1s)+h\nu$	Eq. (4.35)-(4.36)	Table 1.1, [145], [146]
diffusion time of metastables with $m = 1s_5$ or $1s_3$	τ_m	$Ar(1s_5/1s_3)$ + wall $\rightarrow$ Ar(gs)	Eq. (4.38)-(4.40)	[54, 63-147]
pooling ionization between two atoms in the 1s state	$\alpha_{1s,1s}$	Ar(1s) + Ar(1s) $\rightarrow$ Ar(gs) + Ar^+ + e	Eq. (4.41)-(4.43)	[54,148,149]
collisional quenching by Ar atoms	$k_{q,2p}$	Ar(2p) + Ar(gs) $\rightarrow$ Ar(gs) + Ar(gs)		Table 4.3, [1,2]

4.2.3 Processes included in the CRM

4.2.3.1 Electron Impact Excitation and De-excitation

The rate coefficient $Q_{i\to j}$ for an electron collision-induced excitation from a lower level i to a higher level j can be calculated using[50]

$$Q_{i\to j} = \sqrt{\frac{2}{m_e}} \int_{\varepsilon_{ij}}^{\infty} \sigma_{ij}(\varepsilon)\varepsilon^{1/2} f_{\mathrm{e}}(\varepsilon)\mathrm{d}\varepsilon \tag{4.28}$$

where m_{e} is the electron mass, ε_{ij} is the energy difference between level i and level j, and σ_{ij} is the collision cross-section.[50,66,150,151]

For the electron impact de-excitation, the rate coefficient $Q_{j\to i}$ is usually expressed as

$$Q_{j\to i} = Q_{i\to j}\frac{g_i}{g_j}\exp\frac{\varepsilon_i - \varepsilon_j}{k_B T_e} \tag{4.29}$$

wherein g_i and g_j are the statistical weights of the lower and upper state respectively. This equation is derived from principled of detailed balance which is given by[66,151]

$$\frac{N_j}{g_j} = \frac{N_i}{g_i}\exp(-\frac{\varepsilon_{ij}}{kT_e}). \tag{4.30}$$

However, in order to use a general form of the EEDF and not the T_{e} in calculating the rate coefficients, a more generalized form of $Q_{j\to i}$ is used

$$Q_{j\to i} = \frac{g_i}{g_j}\sqrt{\frac{2}{m_{\mathrm{e}}}}\int_{\varepsilon_{ij}}^{\infty}\sigma_{ij}(\varepsilon)\varepsilon^{1/2}\sqrt{\frac{\varepsilon}{\varepsilon-\varepsilon_{ij}}}f_{\mathrm{e}}(\varepsilon-\varepsilon_{ij})\mathrm{d}\varepsilon. \tag{4.31}$$

This expression follows from the relation between the cross sections for the forward and the reverse process, σ_{ij} and σ_{ji} i.e., $\varepsilon\sigma_{ji}(\varepsilon) = (\varepsilon+\varepsilon_{ij})\sigma_{ij}(\varepsilon+\varepsilon_{ij})$.

4.2.3.2 Electron Impact Ionization

While this model does not compute the population density of ionized states directly, it includes electron impact ionization to adjust for the decrease in population of excited states caused by step-wise ionization. The coefficient

for electron impact ionization $Q_{i\to ion}$ is given by

$$Q_{i\to\mathrm{ion}} = \sqrt{\frac{2}{m_\mathrm{e}}}\int_{\varepsilon_{i\to\mathrm{ion}}}^{\infty} \sigma_{i\to\mathrm{ion}}(\varepsilon)\varepsilon^{1/2}F(\varepsilon)d\varepsilon \tag{4.32}$$

wherein the ionization cross section $\sigma_{i\to ion}$ is calculated using

$$\sigma_{i\to\mathrm{ion}}(\varepsilon) = 4\pi a_0^2\left(\frac{\epsilon_1^\mathrm{H}}{\varepsilon_{i\to\mathrm{ion}}}\right)^2 \xi_i\alpha_i\left(\frac{\varepsilon}{\varepsilon_{i\to\mathrm{ion}}}\right)^{-2}\left(\frac{\varepsilon}{\varepsilon_{i\to\mathrm{ion}}}-1\right)\ln\left(1.25\beta_i\frac{\varepsilon}{\varepsilon_{i\to\mathrm{ion}}}\right). \tag{4.33}$$

Here, a_0 is the Bohr radius of the hydrogen atom, ϵ_1^H is the ionization energy of the atomic hydrogen from the ground state, $\varepsilon_{i\to ion}$ is the ionization energy from level i, ξ_i is the number of energetically equivalent electrons present in the shell i ($\xi_i = 6$ for the ground state and $\xi_i = 1$ for levels higher than the ground state), and α_i and β_i are level-dependent parameters.[51,144,151]

4.2.3.3 Radiative Processes

In general, the rate equation for the change in density of an excited atom in level j due to radiative processes is given by

$$\frac{dN_j}{dt} = -A_{ji}N_j + B_{ij}W(\omega)N_i - B_{ji}W(\omega)N_j. \tag{4.34}$$

Here, the Einstein-A coefficient A_{ji} and the Einstein-B coefficients B_{ij} and B_{ji} are the proportionality constants needed to calculate the rate of spontaneous emission, absorption, and stimulated emission respectively. $W(\omega)$ is the radia-

tion field describing the amount of radiation available for the absorption and stimulated emission to occur.[50]

The concept of absorption and stimulated emission is often simplified the concept of an escape factor η, in which the transition probability becomes $A_{ji}\eta$.[50,152] The escape factor is discussed in more detail in the Radiation Trapping subsection given below.

The Einstein-A coefficients used in this are taken from the NIST database.[153]

Allowed Radiative Transitions

For radiative transitions, selection rules for electronic dipole transitions are applied. The first rule is that the change in the angular momentum quantum number Δl is limited to ± 1. This implies that transitions from the 2p levels to the ground state are not allowed. Another rule limits the change in total angular momentum J to $\Delta J = \pm 1$, with the transition from $J = 0$ to $J = 0$ not allowed.[50,154] Appendix B lists the total angular momentum number J for each state.

Because of this, the 1s state can be categorized into two group. The first group is called the resonant states which includes the $1s_4$ and $1s_2$ since they have $J = 1$. That means their transitions to the ground state ($J = 0$) is allowed. On the other hand, $1s_5$ and $1s_3$ has a total angular momentum number of $J = 2$ and therefore their spontaneous emission to the ground state is forbidden. As an effect, $1s_5$ and $1s_3$, which are termed as metastable states, have significantly

longer lifetimes.

Radiation Trapping

Radiation trapping is the phenomenon wherein a photon emitted from spontaneous decay from upper level j to lower level i is reabsorbed by a species in i causing it to get excited to j.[155] This phenomenon is represented by the radiation escape factor η previously introduced above. The escape factor used in this study was from the equation given in Mewe (1967)[146]

$$\eta_{i\to j} = \frac{2 - \exp(-k_{ji}R/1000)}{1 + k_{ji}R}. \tag{4.35}$$

where R is the radius of the chamber and k_0 is the absorption coefficient given by

$$k_{ji} = \frac{\lambda_{ji}^3 n_{\mathrm{i}}}{8\pi} \frac{g_j}{g_{\mathrm{i}}} \frac{A_{\mathrm{j}\to\mathrm{i}} m_{\mathrm{Ar}}^{1/2}}{\sqrt{2\pi k_{\mathrm{B}} T_{\mathrm{g}}}} \ , . \tag{4.36}$$

Here, λ is the wavelength of the specific transition, m_{Ar} is the mass of the atom, and T_g is the gas temperature. The gas temperature values used in this CRM are taken from the work of Schulenberg,[156] and similar to that used in the PIC/MCC simulations. Table 4.2 shows the relation between the escape factor value and the dominant radiative process.[152]

This form of the escape factor in Eq. (4.35) has been preferred over other available alternatives, e.g. Ref. [64, 157–161] since its validity appears to have been verified in other studies (Ref. [162, 163]).

Table 4.2: η and the dominant radiative process

$\eta_{i\to j} = 1$	Absorption and stimulated emission can be neglected
$\eta_{i\to j} = 0$	No net radiative transfer
$\eta_{i\to j} < 0$	Absorption supersedes local emission
$\eta_{i\to j} < 1$	Stimulated emission dominates

Since k_0 depends on N_i, radiation trapping is stronger for states with higher N_i. This means that radiation trapping is strongest for transitions to the ground state due to the high ground state density. Metastable states have longer lifetimes and also tend to have high densities at low pressures, making radiation trapping strong for transitions to these states, especially at low pressures.

The transition parameters included in the CRM are taken from the NIST database[145] and are given in Table 1.1. The intensity of an emission line $I_{j\to i}$ (i.e., photon flux or photon counts) due to the radiative transition from state q to state p is given by

$$I_{j\to i} = n_j A_{j\to i} \eta_{i\to j}. \ , \tag{4.37}$$

The calculated intensities $I_{j\to i}$ are expressed in units of photons $(\mathrm{m^{-3}\,s^{-1}})$[117] and are proportional to the measured relative intensity.

4.2.3.4 Diffusion

As previously mentioned, metastable states have longer lifetimes and therefore, especially at low pressures, they tend to diffuse around inside the plasma. They can eventually collide with the walls and result to a loss in the density of the metastable sates.[59,144] Its rate coefficient is represented by the characteristic time of diffusion τ_m, which represents the amount of time it takes for the metastable states to reach the walls. It is given by[133]

$$\tau_m = \frac{\Lambda^2}{D_m} \ , \tag{4.38}$$

where Λ is dependent on chamber geometry and D is the diffusion coefficient. In this work, equations for Λ and diffusion coefficient were taken from Iordanova and Koleva (2007)[54] given by

$$\frac{1}{\Lambda^2} = \left(\frac{2.405}{R}\right)^2 + \left(\frac{\pi}{L}\right)^2 , \tag{4.39}$$

and D_m is the diffusion coefficient given by

$$D_m = D_{\mathrm{sc,m}} \frac{n_{\mathrm{sc}}}{n_{\mathrm{gs}}} \sqrt{\frac{T_{\mathrm{g}}}{T_{\mathrm{g}}^0}}. \tag{4.40}$$

Here $D_{\mathrm{sc,m}}$, n_{sc} are the diffusion coefficient for the metastable atoms in state "m" and Ar gas density at standard conditions. Following Refs. 54, 147, 63

the values of $D_{\mathrm{sc}} n_{\mathrm{sc}}$ for the $1\mathrm{s}_5$ and $1\mathrm{s}_3$ states are set to $1.8 \times 10^{18}\,\mathrm{cm}^{-1}\,\mathrm{s}^{-1}$ and $1.9 \times 10^{18}\,\mathrm{cm}^{-1}\,\mathrm{s}^{-1}$. T_{g}^{0} is set to 300 K and the electrode gap $L = 4\,cm$.[54,147]

4.2.3.5 Heavy Particle Ionization

Ionization usually happens when electrons collide with atoms. However, when two excited atoms collide, Penning ionization can occur. This process uses the combined energy of both excited atoms to ionize one atom and return the other to its ground state. In this model, ionization by heavy particles is only considered for the 1s states and is ignored for the 2p states due to their significantly lower densities. Rate coefficients α are given by[54,58,118,148,149]

$$\alpha_{r,r} = 1.14 \times 10^{-20} \sqrt{\frac{16 k_{\mathrm{B}} T_{\mathrm{g}}}{\pi m_{\mathrm{Ar}}}} \mathrm{m}^3\mathrm{s}^{-1} \tag{4.41}$$

$$\alpha_{r,m} = 2.10 \times 10^{-15} \mathrm{m}^3\mathrm{s}^{-1} \tag{4.42}$$

$$\alpha_{m,m} = 1.20 \times 10^{-15} \mathrm{m}^3\mathrm{s}^{-1}, \tag{4.43}$$

where α_{rr}, α_{rm} and α_{mm} are the rate coefficients for pooling ionization between two atoms with each being in one of the resonant states, one being in one of the resonant states and the other in one of the metastable states, and each atom being in one of the metastable states, respectively.[54,148,149]

Table 4.3: Constants used for collisional quenching of the $2p_n$ ($n = 1, \cdots, 10$) states by the background gas.[1,2]

2p state	$2p_{10}$	$2p_9$	$2p_8$	$2p_7$	$2p_6$	$2p_5$	$2p_4$	$2p_3$	$2p_2$	$2p_1$
$k_{q,2p}$ $[10^{-16}m^3s^{-1}]$	0.20	0.59	0.24	0.77	0.13	0.12	0.56	1.10	0.53	0.16

4.2.3.6 Collisional quenching

The excited level atoms could collide with the neutral gas and de-excite the excited atoms. The is can be expressed by adding a collisional quenching term, which is represented by the collisional quenching constants given in Table 4.3.

Chapter 5

Machine Learning Models

Machine learning is defined as "the science (and art) of programming computers so they can learn from data".[164] It encompasses three main categories: supervised learning, unsupervised learning, and reinforcement learning. Supervised learning involves training models on labeled data to predict outcomes for new, unlabeled data. This process utilizes algorithms such as decision trees, neural networks, and Bayesian classifiers to map inputs to outputs and minimize prediction errors. In contrast, unsupervised learning operates on unlabeled data to uncover hidden patterns or relationships, making it useful for tasks like clustering and dimensionality reduction, often using techniques such as principal component analysis. Reinforcement learning focuses on training agents to optimize their behavior in various environments to maximize rewards, drawing from optimal control theory and operations research. The choice of machine learning method depends on factors such as data complexity, available computational resources, and the nature of the problem.[165]

In plasma applications, supervised learning has been used to predict properties like chemical, physical, or electrical attributes of surfaces, as well as plasma characteristics like gas dissociation and electron energy. To make these predictions, machine learning uses input features such as optical emission spectra, current-voltage signals, and mass spectrometry data.[91,93,165,166]

In this study, three distinct machine learning models were utilized: two for predicting the EEDF and one for predicting n_e. Specifically, the Kernel Regression for Functional Data (KRFD) and artificial neural network (ANN) models were employed to predict the EEDF, while n_e was predicted using RFR. The hyperparameters for each model were optimized using Bayesian optimization with the Optuna Python library,[167] with 300 trials conducted for each model. Five-fold cross-validation was used to select the validation set and compute validation loss. This technique involves dividing the dataset (excluding the test subset) into five equal parts. The model is trained and tested five times, with each part serving as the test set once and the remaining parts used for training.

5.1 Kernel Regression for Functional Data (KRFD)

One approach employed by some machine learning models, such as Support Vector Machines (SVM) and kernel regression, to handle nonlinear problems involves making predictions based on a similarity function that measures the resemblance between instances. While utilizing similarity features can be highly beneficial, calculating these similarities for large datasets can be computationally intensive. To address this, these models often utilize the kernel trick. This involves using a kernel function that enables the computation of the dot product of two data points in a higher-dimensional space without explicitly transforming the input data.[164] For the kernels $k(t, t_i)$, we use the Gaussian

radial basis kernel function radial basis function (RBF) given by

$$k(t, t_i) = l \ \exp\left(-\frac{\|t - t_i\|^2}{2\sigma^2}\right). \tag{5.1}$$

where l is a length scale parameter, σ is the bandwidth parameter of the basis function, and $\|t - t_i\|$ is the Euclidean distance of the electron energy t from the ith kernel center t_i. While the use of other RBF can be explored as a future work, a Gaussian RBF was chosen due to its wide usage as a kernel function in kernel regression models. In this study, σ is used as a hyperparameter to be optimized for regularization. Increasing σ decreases the width of the Gaussian RBF, decreasing the range of influence of each instance.

The KRFD was originally developed in Ref. 168. The method allows to obtain a function $Y(t)$ from an input vector X. The predicted output $Y(X, t)$ is modeled by

$$Y(X, t) = \sum_{i=1}^{T} \beta_i(X) k_T(t, t_i) + \mu(t) + \delta. \tag{5.2}$$

Here, T is the total number of data points in t. In this study, t is set to be the electron energy, $Y(t; X)$ is assigned as the EEDF at that energy, while X represents the 16-dimensional input vector comprising OES intensities and pressure. A set of T positive definite kernel functions, $k(t, t_i)$ ($i = 1, \ldots, T$), is placed at arbitrarily specified centers t_i ($i = 1, \ldots, T$) within the support of the electron energy. The regression coefficient or weight parameter $\beta_i(X)$ is modeled as a function of X, which activate or deactivate each kernel. While in Ref. 168

the coefficients were modeled with ANNs, in this study kernel regressors are used to achieve more robust and cost-effective modeling. Additionally, $\mu(t)$ is a baseline function that relies only on t, and δ is the noise term. Unlike ordinary regression, where the output is typically given as a scalar variable or relatively low-dimensional vector, the output variable here is treated as a function of t. Such a task is called functional output regression.

The coefficient functions $\beta_i(X)$ ($i = 1, \ldots, T$) are modeled with additional kernel regressors. Specifically, Eq. (5.2) is expressed as

$$Y(X,t) = \sum_{k=1}^{N}\sum_{l=1}^{T} \theta_{kl} k_G(X, X_k) k_T(t, t_l) + \sum_{m=1}^{N} c_m k_M(X, X_m) + \delta. \tag{5.3}$$

Here, θ_{kl} and c_m represent the regression coefficients, k_G(X,X_k) and k_M (X,X_m) denote the Gaussian RBF kernels on variable X, k_T(t,t_l) is the RBF kernel on t, and N denotes the number of the kernel functions for X. This can be obtained by setting $\beta_i(X) = \sum_{k=1}^{N} \theta_{ki} k_G(X, X_k)$ in Eq. (5.2).

In this study, ridge regression with ℓ_2 regularization was performed to estimate the coefficient parameters, θ_{kl} and c_m, where the objective function O to be minimized during model training is given by

$$\begin{aligned} O(\boldsymbol{\Theta}, \boldsymbol{c}) =& \|\boldsymbol{Y} - \boldsymbol{G}\boldsymbol{\Theta}\boldsymbol{T} - \boldsymbol{M}\boldsymbol{c}\boldsymbol{1}^T\|_F^2 + \alpha_G \|\boldsymbol{G}^{1/2}\boldsymbol{\Theta}\boldsymbol{T}\|_F^2 \\ &+ \alpha_T \|\boldsymbol{G}\boldsymbol{\Theta}\boldsymbol{T}^{1/2}\|_F^2 + \alpha_G\alpha_T \|\boldsymbol{G}^{1/2}\boldsymbol{\Theta}\boldsymbol{T}^{1/2}\|_F^2 + \alpha_M \|\boldsymbol{M}^{1/2}\boldsymbol{c}\boldsymbol{1}^T\|_F^2. \end{aligned} \tag{5.4}$$

where $\boldsymbol{Y}$, $\boldsymbol{G}$, $\boldsymbol{\Theta}$, $\boldsymbol{T}$, and $\boldsymbol{M}$ are $N \times T$, $N \times N$, $N \times T$, $T \times T$, and $N \times N$ matrices whose entries are given by $\boldsymbol{Y}_{ij} = Y(X_i, t_j)$, $\boldsymbol{G}_{ij} = k_G(X_i, X_j)$, $\boldsymbol{\Theta}_{kl} = \theta_{kl}$, $\boldsymbol{T}_{ij} = k_T(t_i, t_j)$, $\boldsymbol{M}_{ij} = k_M(X_i, X_j)$, and $\boldsymbol{c} = (c_1, \cdots, c_N)^{\mathrm{T}}$. Here, $\mathbf{1}$ denotes a T-dimensional vector whose entries are all one and a square matrix raised to the power $1/2$ is another square matrix whose product with itself gives the original matrix. Additionally, $\| \|_F$ represents the Frobenius norm. The optimal solutions for $\boldsymbol{\Theta}$ and $\boldsymbol{c}$ were determined by solving the system of equations obtained by setting $\frac{\partial O(\boldsymbol{\Theta}, \boldsymbol{c})}{\partial \boldsymbol{\Theta}} = 0$ and $\frac{\partial O(\boldsymbol{\Theta}, \boldsymbol{c})}{\partial \boldsymbol{c}} = 0$.

In this study, each of the 16 input variables was standardized to have a mean of 0 and a standard deviation of 1 in the training dataset. About 20% of the total data was randomly selected for the test set, and the remainder was used as the training set. The hyperparameters were selected using Optuna through five-fold cross-validation within the training set. The parameters to be selected were σ_G, σ_T, and $\sigma_M \in \{1, \ldots, 100\}$ which is the bandwidth parameters for the Gaussian RBF kernels $k_G(X, X_k)$, $k_T(t, t_l)$, and $k_M(X, X_m)$, and the regularization coefficients α_G, α_T, and $\alpha_M \in \{10^{-6}, \ldots, 1\}$. For the regularization coefficients, the values were sampled from the logarithmic domain. The best hyperparameters were selected to be σ_G = 90.079, σ_T = 98.626, σ_M = 24.894, $\alpha_G = 1.141x10^{-4}$, $\alpha_T = 3.965x10^{-6}$, and $\alpha_M = 0.128$.

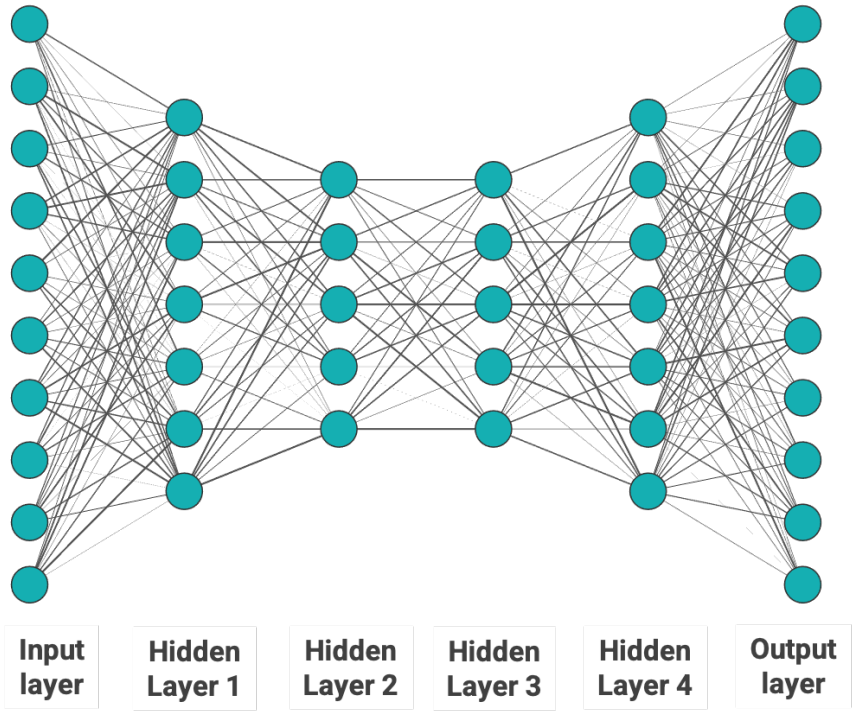

Figure 5.1: A sample artificial neural network (ANN)

5.2 Artificial neural network (ANN)

In recent years, the use of Artificial Neural Networks (ANNs) has surged across various applications, including image and speech recognition. The concept of ANNs dates back to 1943 when McCulloch and Pitts introduced a computational model that simulates how neurons work together to perform complex calculations. Their model featured a basic artificial neuron with one or more binary inputs and a single binary output. In 1957, Frank Rosenblatt advanced this idea by developing the perceptron, a model where a step function is applied to the weighted sum of input values to generate an output. The work on ANN however died down after a while until some slow progress in

the 1980s and led to now in which the increase in the amount of data and computational power motivated its further use.[164]

An ANN is composed of interconnected nodes organized into layers, as illustrated in Fig. 5.1. The input data is fed into the input layer, and the predictions come out in the output layer. In between these two layers are the hidden layers where the core calculations take place. A fully connected layer, also known as a dense layer, consists of neurons or nodes that are linked to every node in the preceding layer. The input data is passed from a node in the input layer to a node in the next layer, and each value that the node in the next layer receives get multiplied to a weight, and these weighted values are summed up and a bias value is added up.

$$z_a = (\sum_{q=1}^{Q} \omega_{a-1} y_{a-1}) + b_a, \tag{5.5}$$

where a corresponds to the current layer, q corresponds to each node a value is received from and Q is the total number of these nodes. ω_{a-1} is the weight associated with the input data or output from a previous node y_{a-1}, and b_a is the bias term. Each calculated z_a is then fed to an activation function Υ such that the final value y_a that a node in layer a gets is

$$y_a = \Upsilon(z_a). \tag{5.6}$$

The activation function plays a crucial role by determining whether a neuron activates, thereby influencing the propagation of information to subsequent

layers and introducing nonlinear transformations to the data. Commonly used activation functions include the logistic function $\zeta(y_a) = \frac{1}{1+\exp(-y_a}$, hyperbolic tangent function $tanh(y_a) = 2\zeta(2y_a) - 1$ and the rectified linear unit function $ReLU(y_a) = \max(0, y_a)$. The calculated y_a is then passed to the next layer in the same manner until it eventually reaches the output layer and makes a prediction. The error of the predicted output with respect to the expected output is then calculated. The next step would be determining how much each weight and bias in each layer contributed to the error. This is done getting the partial derivative of the error to each weight and bias by chain rule.

Gradient descent is then applied to see how much the values of the weights and biases is changed to reduce the error, and is usually determined by the value of the learning rate. Each iteration containing this forward pass and backward pass is called an epoch.[164]

The design of the hidden layers, including the number of layers and nodes, greatly affects performance. ANNs with more layers are better at handling complex and nonlinear problems, but care must be taken to avoid overfitting the model to the data. Key settings, called hyperparameters, such as the number of layers, nodes per layer, activation functions, learning rate, and optimization algorithm, shape the ANN's architecture and impact its ability to learn complex data patterns. These hyperparameters are set before training and are crucial for the network's performance.[169,170]

In this study, a conventional ANN with backpropagation was utilized for the EEDF prediction. The model architecture comprises of four hidden layers

positioned between the input and output layers. As with the KRFD approach, the input variable X encompasses the 15 spectral intensities from OES and the pressure, while the output variable Y comprises a vector of EEDF values at 1999 different energies. Each layer was constructed by a fully connected network and the ReLU activation function. About 20% of the total data was randomly selected for the test set, and the remainder was used as the training set. By performing the five-fold cross-validation within the training set, the hyperparameters were selected using Optuna; the parameters to be selected were the number of neurons for each layer $\in \{16, \ldots, 1800\}$, and the learning rate $\in \{10^{-6}, \ldots, 10^{-2}\}$. The number of neurons for each hidden layer and the learning rate were optimized to be 355 neurons and $3.633x10^{-4}$. Each model was trained using the stochastic gradient descent algorithm. The number of iterations (epochs) was set to 1000 for both the hyperparameter optimization and the final model training with the selected hyperparameters.

5.3 Random Forest Regression (RFR)

A decision tree is a versatile algorithm widely used for classification and regression tasks of single or multioutput data. By aggregating multiple predictors such as decision trees during training and then combines their results, one can create an ensemble learning algorithm such as Random Forest. To create a diverse set of trees, one can use different training algorithms for each or use a different random subset of data in training each tree.[164] Their results can then

be combined by using the most frequent prediction for classification or the average prediction for regression. Random Forest is particularly useful because it can handle large datasets with many features while still providing accurate predictions. It also has built-in methods for selecting important features and managing missing values. Additionally, it is resistant to noisy data and outliers, making it suitable for various real-world applications.[171–175]

When using Random Forest, you can tune several hyperparameters to optimize its performance for a specific task. Some of the most important hyperparameters include: $\mathrm{n\_estimators}$ or the number of trees in the forest, $\mathrm{max\_depth}$ or the maximum depth of each tree in the forest, $\mathrm{min\_samples\_split}$ or the minimum number of samples required to split an internal node, $\mathrm{min\_samples\_leaf}$ or the minimum number of samples required to be at a leaf node, and the $\mathrm{max\_features}$ or the number of features to consider when looking for the best split. By adjusting these hyperparameters, one can fine-tune the Random Forest algorithm to achieve optimal performance for their particular dataset and problem domain.[174,175]

RFR was used to predict a discrete scalar value of n_{e}. Although two RFR models were created, each attached to the KRFD and ANN, they yielded almost the same results. Therefore, for the remainder of this paper, only the RFR model attached to the KRFD was included. By hyperparameter optimization using Optuna, the best value for the number of trees $\in \{10, \ldots, 500\}$, and a number of features in each tree $\in \{3, \ldots, 15\}$ were selected. This optimization resulted

in 89 trees and 15 features as best hyperparameter values. The branches of the tree were expanded until each leaf contained less than 2 samples.

5.4 Data Preparation

This study used the intensities of 15 spectral lines as the input vector to predict the EEDF and n_e as the output data. In addition to the OES intensities, the pressure was also included as an input variable, resulting in a 16-dimensional input vector. The functional variable EEDF was discretized on an equidistant grid having 1,999 points, while n_e was given as a discrete scalar variable. The preparation of the input vectors from calculated and measured data is outlined in the following.

5.4.1 PIC+CRM simulation data

The simulation dataset used for ML was generated through the PIC+CRM. Fro the training data, the pressure was varied from 2-100 Pa and the peak-to-peak voltage from 200 - 500 V. A total of 108 sets of OES intensities and plasma parameters were generated for the training and testing of the ML models. For each pair of input and output data, all other parameters are the same except for the EEDF, n_e, the gas temperature T_g and the pressure. The values used for T_g ranged from 304 K to 348.4 K and were interpolated from experimental tunable diode laser absorption spectroscopy (TDLAS) measurements done in Ref. [8].

Out of the 108 data sets that we generated, 80% were randomly selected for training, and the rest samples were reserved for testing. The logarithm of the EEDFs was taken and these resulting EEDFs were used as the training data, as it was observed that predictions in linear scale tend to neglect the higher energy region. Additionally, to ensure that even zero values could be transformed into the logarithmic scale, a small constant value of 10^{-10} was added to each data point in the EEDF.

5.4.2 Experimental data

The experimentally measured OES intensities served as a second set of input test data for the evaluation of the predictive performances of the ML models. Similar to the treatment applied to calculated intensities, the measured relative intensities were also normalized using Eq. (6.4). The measured T_{g} data were interpolated and employed as input parameters for both the PIC/MCC simulations and the CRM. On the other hand, the measured $1\mathrm{s}_5$ density data served as reference data for additional validation of the predicted results.

Chapter 6

Results: Simulation of optical emission spectra and its experimental validation

In this chapter, the validation results for the PIC+CRM for an Ar RF CCP are presented. It starts with the discussion of some of the results of the PIC/MCC simulations that is used in the CRM, specifically the n_e and the EEDF. Following this, we conduct a sensitivity analysis of the CRM in response to these input parameters. We then compare the measured and simulated intensities, providing a detailed analysis of potential sources of discrepancies between the intensities under specific conditions.

6.1 PIC/MCC results relevant to the CRM

For better comparison with the experimental data, the information about the same spatial region of about 1 cm in the middle of the discharge is extracted from the PIC/MCC simulation. The essential input data for the CRM are the EEDF $f_\mathrm{e}(\varepsilon)$ and electron density n_e. The electron density and a function related to the EEDF defined as

$$f_\mathrm{p}(\varepsilon) = \varepsilon^{-1/2} f_\mathrm{e}(\varepsilon) \ , \tag{6.1}$$

are plotted in Fig. 6.1 at various pressures for discharges with a voltage amplitude of 300 V peak-to-peak. The function f_p is often called an electron energy

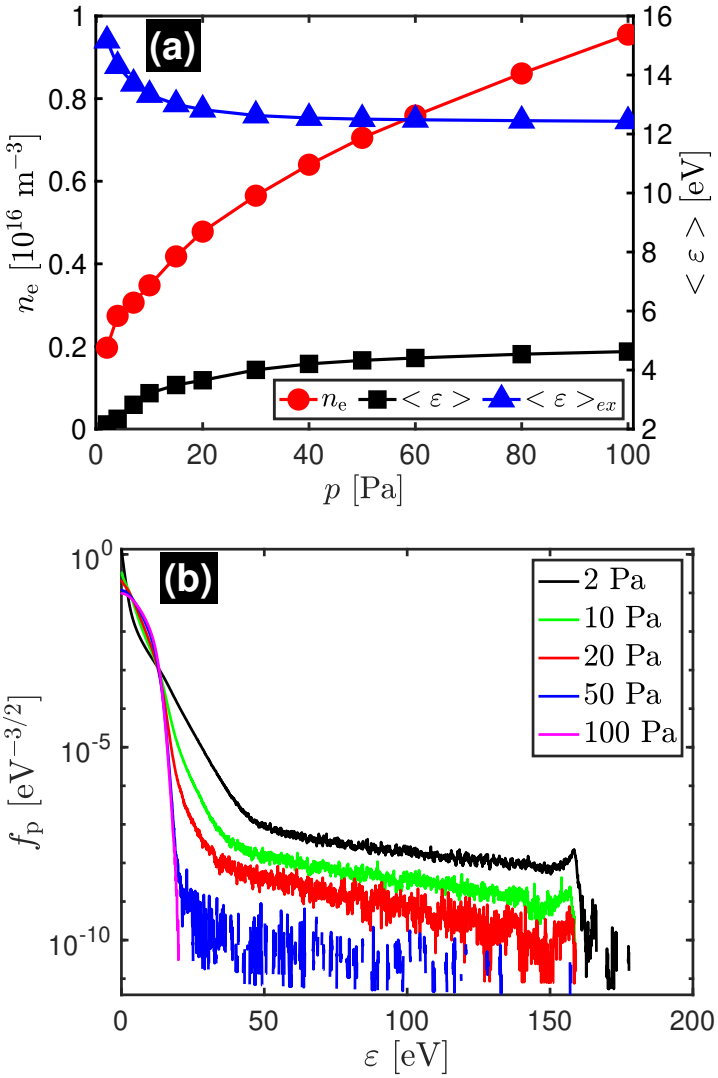

Figure 6.1: PIC/MCC simulation results for the central (1-cm-wide) region of 13.56 MHz RF-driven Ar CCPs with a sinusoidal voltage waveform with a peak-to-peak voltage (V_{pp} of 300 V. (a) The electron density (circles), mean electron energy for the total electron population $\langle\varepsilon\rangle$ (squares), and that for the energetic electrons above the excitation threshold voltage of 11.55 eV $\langle\varepsilon\rangle_{ex}$ (triangles), as functions of the Ar gas pressure. (b) The EEPF at different Ar gas pressures. Because $V_{pp} = 300$ eV, a sudden drop of the EEPF is seen above 150 eV (i.e., about a half of V_{pp}, corresponding to the sheath voltage) at low pressures. It should be noted that the only ionization and excitation taken into account in the simulation here are those by electron impact with ground-state Ar atoms.

probability function (EEPF).[176] Also plotted in Fig. 6.1(a) are the mean energy of the bulk electrons

$$\langle \varepsilon \rangle = \int_0^\infty \varepsilon f_\mathrm{e}(\varepsilon) \mathrm{d}\varepsilon \tag{6.2}$$

and that of the energetic electrons above the threshold energy ε_1

$$\langle \varepsilon \rangle_\mathrm{ex} = \frac{\int_{\varepsilon_1}^\infty \varepsilon f_\mathrm{e}(\varepsilon) \mathrm{d}\varepsilon}{\int_{\varepsilon_1}^\infty f_\mathrm{e}(\varepsilon) \mathrm{d}\varepsilon} \quad . \tag{6.3}$$

Here we set $\varepsilon_1 = 11.55\,\mathrm{eV}$, i.e., the excitation threshold energy of the lowest excited state of Ar atoms, to represent energetic electrons that can excite ground-state Ar atoms.

It is seen in Fig. 6.1(a) that the mean energy of bulk electrons $\langle \varepsilon \rangle$ increases and that of energetic electrons $\langle \varepsilon \rangle_\mathrm{ex}$ decreases rather steeply up to about 20 Pa. The decrease of $\langle \varepsilon \rangle_\mathrm{ex}$ causes a corresponding decrease in excitation and ionization at higher pressures. As discussed earlier, the only ionization and excitation mechanisms used in the PIC/MCC simulation presented here are the electron-impact ionization and excitations of ground-state Ar atoms. At higher pressures, this lower ionization rate balances the decreased particle losses, and leads to lower energy per ion-electron pair created, thus allowing higher plasma density to be sustained.

It is seen in Fig. 6.1(b) that, above a certain energy, a slowly decaying energetic component is present. It reflects the "runaway" secondary electrons released from the electrodes due to ion bombardment. The density of these

"runaway" secondary electrons in the middle of the discharge decreases with an increasing pressure due to a decrease in their mean free path. At 100 Pa, the energetic tail is completely extinguished by collisions and the electron energy does not go beyond 20 eV.

6.2 Sensitivity of calculated line intensities to input parameters of the CRM

It is also important to verify to what extent the output of the models, i.e. the spectral intensities are sensitive to a variation of the input parameters (electron density and distribution). For that, a sensitivity analysis is carried out to quantify the effect. Figure 6.2(a) shows the result for the variation of the electron density used as an input parameter to the CRM at 20 Pa. Three n_e values are used for this comparison, i.e., the n_e value calculated from the PIC/MCC simulation ($n_\mathrm{e,PIC} = 4.78 \times 10^{15}\mathrm{m}^{-3}$), its half ($0.5 n_\mathrm{e,PIC} = 2.39 \times 10^{15}\mathrm{m}^{-3}$), and its double ($2 n_\mathrm{e,PIC} = 9.56 \times 10^{15}\mathrm{m}^{-3}$). Here, the CRM used the EEDF from the same PIC/MCC simulation at 20 Pa. In the consequent discussions, the emission line denoted as 772.4 nm in Fig. 6.2(a)–(b) corresponds to the sum of the intensities of 772.38 nm and 772.42 nm lines.

The intensities are expected to increase with increasing n_e due to the increase of electron impact excitation rate to the 2p states. This becomes evident if one considers the balance for the population density of a given 2p state (Eq. (4.27)). Both the direct and the stepwise excitation processes (left-hand side of

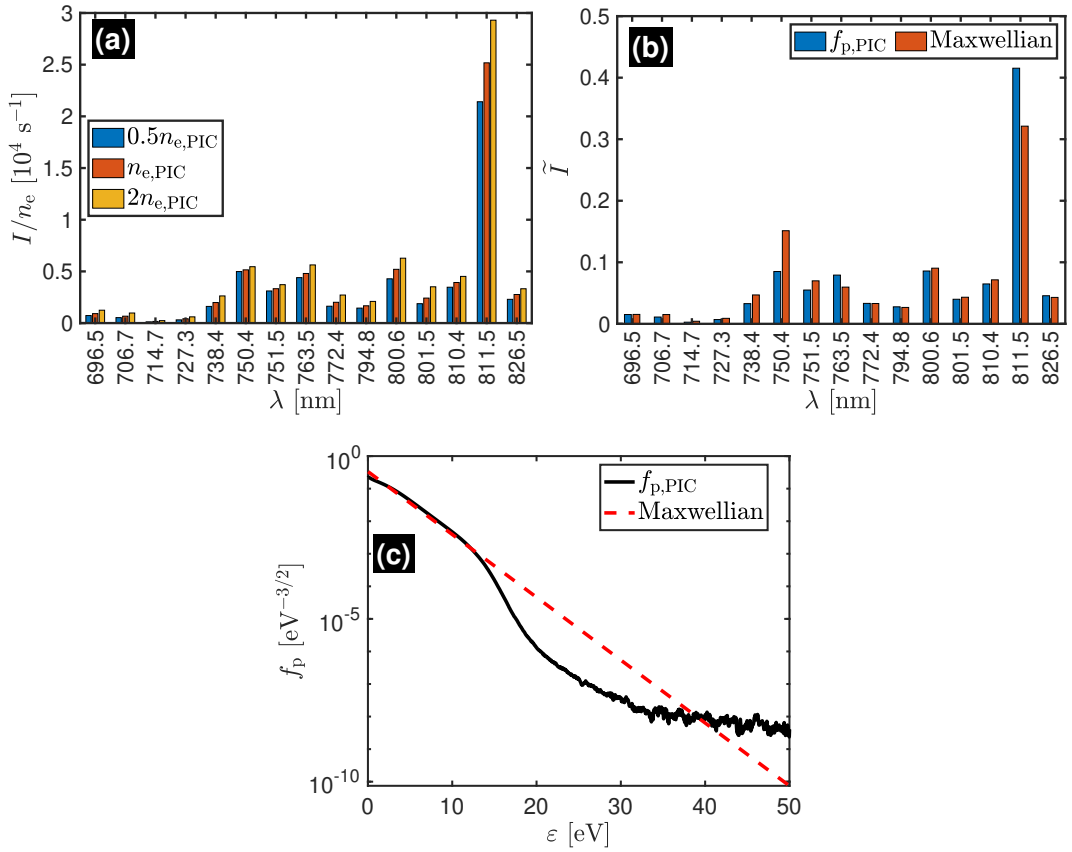

Figure 6.2: (a) The emission intensity I defined by Eq. (4.37) and obtained from the CRM divided by the electron density n_e with 3 different electron density values, i.e., $n_e = 0.5n_{e,PIC}$, $n_{e,PIC}$, and $2n_{e,PIC}$, where $n_{e,PIC}$ denotes the electron density obtained from the PIC/MCC simulation at 20 Pa. (b) The normalized intensity $\widetilde{I}$, defined in Eq. (6.4), obtained from the CRM with $n_e = n_{e,PIC}$ and two different EEPFs; one from the PIC/MCC simulation at 20 Pa, denoted by $f_{p,PIC}$ and given by the solid curve in (c), and a Maxwellian distribution, given by the dotted line in (c).

the equation) are proportional to the electron density, whereas the losses (the right-hand side) are usually dominated by the radiative transitions (the second to the last term on the right-hand side). Consequently, the emission intensity for transitions from this state varies nearly linearly with the electron density, with slight deviations due to non-linearities, introduced by the dependence of the population in the 1s block on n_e as well as the contribution of collisions to the losses of the 2p state. To amplify these more subtle nonlinear effects, the linear dependence on the plasma density is canceled out by dividing the intensity values by n_e. These 'reduced' values are shown in Fig. 6.2(a). For most of the lines, i.e. for most of the 2p states only a weak dependence on the plasma density of the order of about 10% or less remains. This dependence is also almost linear, indicating that the contribution of the stepwise and cascade processes to the population of the 2p states has a linear dependence on n_e, and the collisions with electrons have a negligible contribution for the losses.

The sensitivity of the CRM to the EEPF used is also tested and shown in Fig. 6.2(b). In this figure, the resulting CRM intensities I_k (where the index k represents the individual lines for transition $q \rightarrow p$) are normalized with respect to the total intensity of the spectral lines shown, such that

$$\widetilde{I} = I_k / \sum I_k \ . \tag{6.4}$$

Here "$f_{\mathrm{p,PIC}}$" denotes the case when the EEPF calculated from the PIC/MCC simulation is used in the CRM, while the "Maxwellian" labels the case when a

Maxwellian distribution with a T_e equal to the estimated bulk T_e of the EEPF from the PIC/MCC simulation is taken as the input for the CRM. Both these EEPFs are presented in Fig. 6.2(c). The two distribution functions coincide up to around 11 eV, which is near the excitation threshold energy of the lowest excited state ($\varepsilon_1 = 11.55$ eV). Beyond 11 eV, the Maxwellian has a higher electron distribution up to around 40 eV. Since the excitation and ionization processes from the ground state occur in this energy region, a significantly higher intensity for the 750.4 nm line ($2p_1 \rightarrow 1s_2$) is observed when a Maxwellian EEPF is used. This is due to the large electron impact collision cross section of the $2p_1$ state from the ground state. This change in the shape of the spectra shows the importance of the accurate description of a non-Maxwellian EEDF for reliable intensity values.

6.3 Comparison between measured and calculated intensities

The comparison between measured and calculated intensities is presented in Fig. 6.3, for pressures of 2 Pa, 20 Pa, and 50 Pa. The data are again normalized according to Eq. (6.4), for a straightforward comparison.

The general trend of the dominant kinetic mechanisms for these pressure cases is first discussed. At low pressures, the plasma tends to be in the corona regime where the dominant processes are electron collision with the ground-state atoms and subsequent spontaneous emission from the higher excited states to the lower excited states resulting to a high intensity for the 750.4 nm

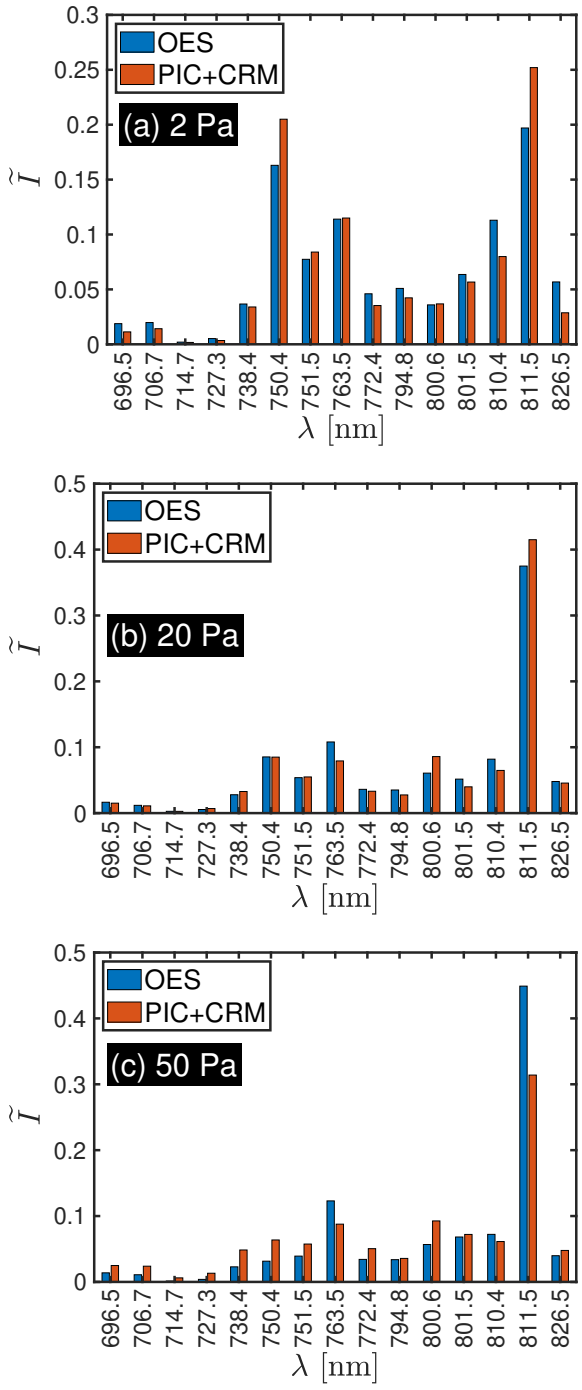

Figure 6.3: Measured and calculated normalized intensities at (a) 2 Pa, (b) 20 Pa, and (c) 50 Pa. As discussed earlier, the intensity line denoted as 772.4 nm corresponds to the sum of the intensities of 772.38 nm and 772.42 nm lines.

line at 2 Pa for both measurements and simulations. Similarly, the 811.5 nm line is strong due to the high statistical weight of the $2p_9$ state, which also has a large cross section from the ground state.

The changes in the spectrum at 20 Pa with respect to the previous case of 2 Pa originate mainly from the decrease of $< \varepsilon >_{ex}$ with the increase in pressure as shown in Fig. 6.1(a). As a result of this, a lower percentage of the excitation occurs from the ground state and stepwise excitation from the excited states becomes important. In this low-pressure non-equilibrium regime,[46] the intensity of the 750.4 nm line therefore decreases relatively strongly as compared to other lines which are also populated by electron impact from excited states. The 'metastable-dependent' lines i.e., the ones excited by low-energy electrons from the metastable levels include 763.5 nm ($2p_6 \rightarrow 1s_5$), 800.6 nm ($2p_6 \rightarrow 1s_4$), and 811.5 nm ($2p_9 \rightarrow 1s_5$), since the $2p_6$ and the $2p_9$ states have a large collision cross section from the $1s_5$ state.

For the 50 Pa case, the 763.5 nm and 811.5 nm lines dominate the emission spectrum. The calculated intensities of these lines are significantly lower than the measured ones, while the calculated intensity of the 800.6 nm line is significantly higher than the measured line. Unlike the 800.6 nm line, the 763.5 nm and 811.5 nm lines are nonlinearly dependent on the population of the $1s_5$ state through radiation trapping since these lines also decay to the $1s_5$ state. A high $1s_5$ density (n_{1s_5}) can therefore cause a depletion of the calculated intensities by radiation trapping.

Generally, it appears that the model results tend to overestimate at higher pressures the intensities of lines for which the self-absorption is not significant, i.e. 706.7 nm, while at lower pressures they are underestimated. Simultaneously, lines with relatively high contribution of the radiation trapping, i.e. 763.5 nm, exhibit the opposite trend. This is related to an overestimation of the population of the states in the 1s block with the pressure increase, demonstrated and discussed later in Section 6.4.1. The effect of this overestimation for the lines in the first group is higher step-wise excitation than present in the experiment, leading to higher densities of the corresponding 2p states. For the lines in the second group the radiation trapping effect manifests itself stronger than actually present experimentally.

These trends are also visible in Fig. 6.4 where we present the ratios of the measured (OES) and calculated (PIC+CRM) line intensities such that

$$r_k = I_{\mathrm{OES}}(\lambda_k)/I_{\mathrm{PIC+CRM}}(\lambda_k) \quad . \tag{6.5}$$

For this comparison, the line intensities have been scaled so that the average of the r_k values is 1.0. In an ideal case, i.e., in the case of a perfect agreement between the OES measurements and the PIC+CRM results, $r_k = 1$ would be recovered for each k. The data exhibit, of course, some deviations from this case, which vary as a function of the gas pressure.

In the 2 Pa case, the lines originating from the $2\mathrm{p}_2$ state, namely the 696.5 nm, 727.3 nm, and 826.5 nm lines have higher intensities from the OES

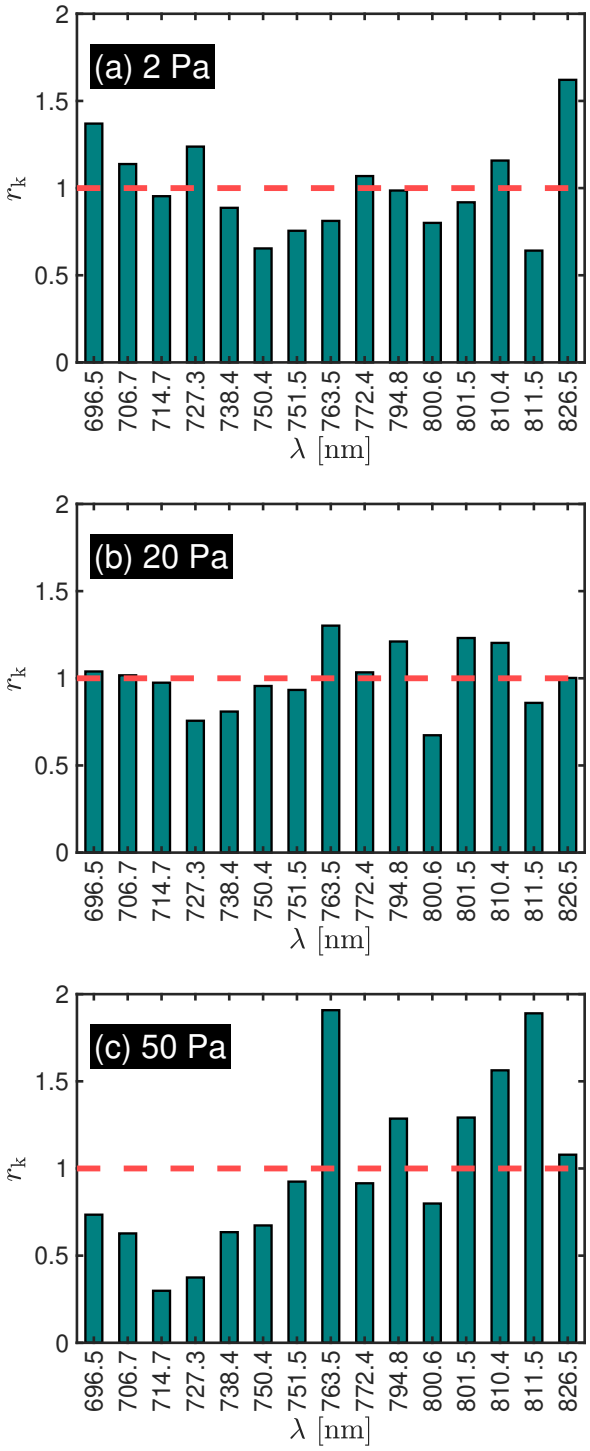

Figure 6.4: Normalized ratios of the intensities of the spectral lines measured using OES and calculated from PIC+CRM, at (a) 2 Pa, (b) 20 Pa, and (c) 50 Pa. As discussed earlier, the intensity line denoted as 772.4 nm corresponds to the sum of the intensities of 772.38 nm and 772.42 nm lines.

as compared to the calculated values. The common behavior of these lines suggests that the PIC+CRM may underestimate the population of the $2p_2$ state. No such conclusion can be drawn, however, for the densities of the other states as lines originating from those do not necessarily show deviations in the same 'direction'. The best agreement is observed for p = 20 Pa, where the intensity ratios deviate less than $\approx$ 20% from the unit value. At 50 Pa, very strong deviations are observable, indicating the breakdown of the modeling approach, as will be discussed later. In this case, the 763.5 nm and 811.5 nm lines exhibit particularly strong deviations. The lower level of these lines is the $1s_5$ state, which typically has the highest concentration among the excited states. The situation at this pressure is further complicated by the fact that radiation trapping from all the 1s states is expected to become significant. At this pressure, excitation from all 1s states becomes important in the "medium-pressure non-equilibrium" regime.[46]

To quantify these deviations the RMSE of the r_k values is calculated as

$$RMSE = \sqrt{\frac{1}{N}\sum_{k=1}^{N}(r_k - 1)^2}, \tag{6.6}$$

where $N = 15$ is the number of spectral lines. (The case of a perfect agreement between the OES and the PIC+CRM data would correspond to RMSE = 0.)

For the 2 Pa case, a relatively low RMSE of 0.26 is obtained. The agreement further improves with increasing pressure, up to 20 Pa. Beyond that value, however, the RMSE starts to increase rapidly and shows the inability

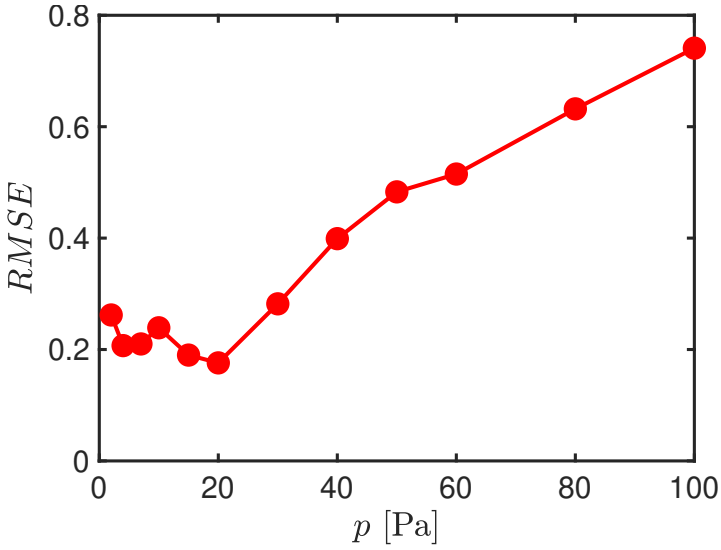

Figure 6.5: RMSE of the standard deviation of the OES/PIC+CRM ratio r_k to the average ratio of 1

of the PIC+CRM approach to predict line intensities correctly. This failure of the approach at elevated pressures is suspected to be related to the presence of the excited states in the discharge, in particular the $1s_5$ state, with significant concentrations. Therefore, in the next sections we analyse the pressure dependence of the density of this state as obtained experimentally and in the CRM, and address the influence of this state on the ionization in the plasma.

6.4 Effects of the $1s_5$ metastable state

6.4.1 Density measurement and comparison with the simulation results

The comparison of the measured and computed $1s_5$ density (n_{1s5}) is given in Fig. 7.10 as functions of the Ar gas pressure. The laser absorption measurements show that n_{1s_5} increases with a pressure up to around 10 Pa and saturates

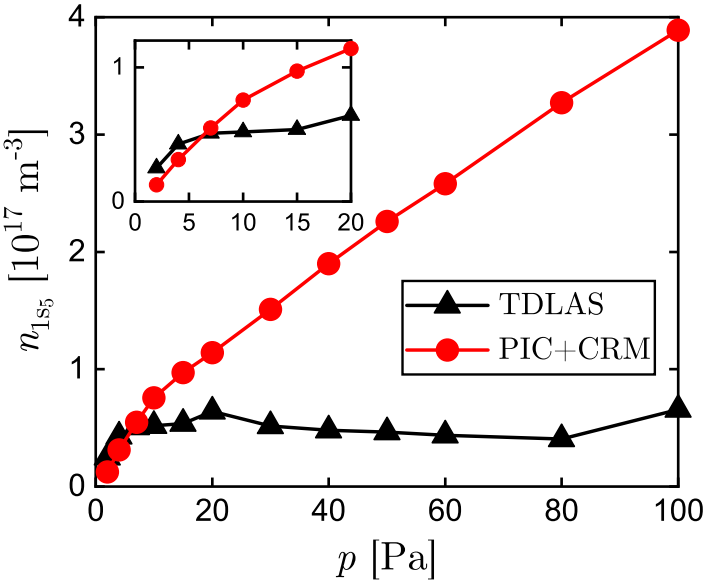

Figure 6.6: The densities of the $1s_5$ state Ar atoms measured with TDLAS and evaluated from the PIC+CRM simulations as functions of the gas pressure. The inset shows the same data at low pressures.

at around 4×10^{16} m^{-3}. Below this pressure, the measured n_{1s_5} values agree closely with the computed ones. However, above this pressure, the simulation results show a continuous increase of the n_{1s5}. Because the electron-impact excitation to the $1s_5$ state from the ground state requires a minimum energy of 11.55 eV, Fig. 7.10 indicates that our PIC/MCC simulation either overestimates the density of the energetic electrons or underestimates the loss processes of the metastable states in our simulations.

6.4.2 Ionization from the 1s$_5$ state

To further check the effect of the $1s_5$ metastable state on ionization, the contributions of the ground state and the $1s_5$ state to the ionization process

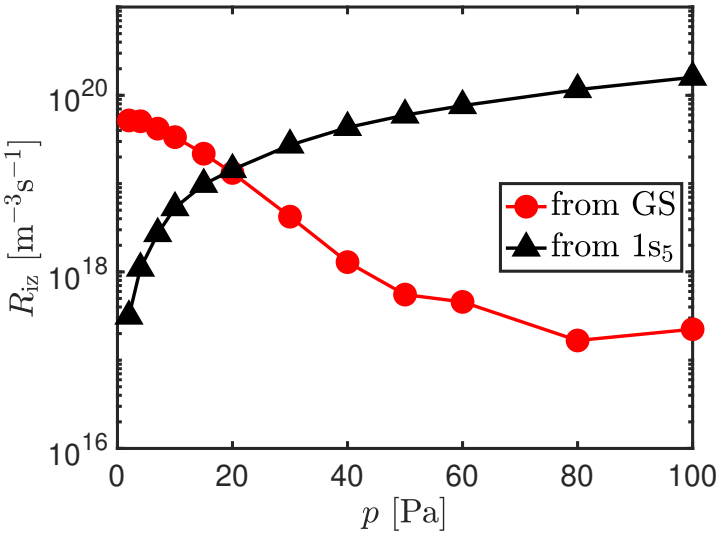

Figure 6.7: Rates of ionization from the ground state (denoted by "GS" and filled circles) and the $1s_5$ metastable state (filled triangles). The ionization energy from the ground state is 15.8 eV and that from the $1s_5$ metastable state is 4.2 eV

were evaluated in the CRM. While the CRM described in Eqs. (4.25), (4.26), and (4.27) does not account for the ionization originating from the ground state, its rate of ionization is determined using Eq. (4.28), as is done for the excited states. Figure 6.7 shows a comparison of the number of ions generated per unit volume and unit time by the ionization from the ground state and the $1s_5$ metastable state calculated from the PIC+CRM simulation. This figure shows that, below 20 Pa, the ionization rate from the ground state is higher than that from the metastable state. This changes as the pressure increases and the ionization originating from the ground state decreases until it is approximately three orders of magnitude lower than that from the metastable state at 100 Pa.

Such a trend is supported by the mean energy results from Fig. 6.1(a), where the $< \varepsilon >_{\mathrm{ex}}$ is shown to decrease to energies lower than the ground-state ionization threshold as the pressure increases. On the other hand, above 20 Pa, $< \varepsilon >$ saturates at around 4 eV, at which ionization from the $1\mathrm{s}_5$ metastables becomes significant as the ionization energy from the $1\mathrm{s}_5$ metastable state is 4.2 eV. It should be noted that the simulation results presented in Fig. 6.7 used the electron density and EEDF data obtained from the PIC/MCC simulation that does not include the ionization from the $1\mathrm{s}_5$ state. Therefore it clearly shows an inconsistency between the premise and the simulation results. Under our discharge conditions, at pressures above 20 Pa, the $1\mathrm{s}_5$ state plays a dominant role in ionization and should not be ignored even in PIC/MCC simulations.

6.4.3 Comparison with a Corona model

The effect of the $1\mathrm{s}_5$ state on the excitation dynamics is investigated next. Within the framework of the corona model expected at the lower pressures, only the electron impact excitation from the ground state and the spontaneous emission from the 2p states (with $\eta_{i \to j} = 1$) are included. Then the balance equation for each of the 2p states in Eq. (4.27) simplifies to

$$n_{\mathrm{gs}} Q_{\mathrm{gs} \to 2\mathrm{p}} n_{\mathrm{e}} = \frac{n_{2\mathrm{p}}}{\tau_{2\mathrm{p}}}. \tag{6.7}$$

In this equation, $2p$ denotes any of the ten 2p states, and $\tau_{2\mathrm{p}}$ is the lifetime of the corresponding 2p state defined by $1/\tau_{2\mathrm{p}} = \sum_{i=1s} A_{2\mathrm{p} \to i}$, where the summation is

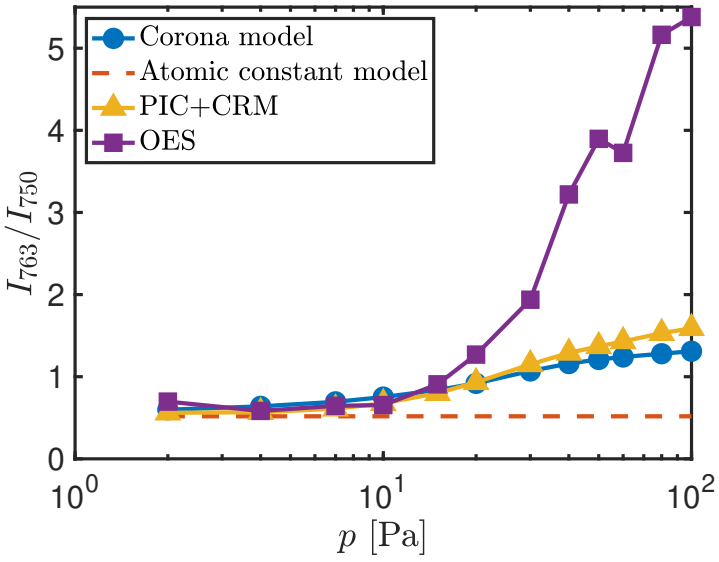

Figure 6.8: Intensity ratios of the 763.5 nm and 750.4 nm lines obtained from the experimental OES data (squares), calculated with the corona model (circles), PIC+CRM simulations (triangles), and the atomic constant model (dotted line).

taken over all 1s states. Since n_{e} as well as n_{gs} cancel out, the ratio of intensities of two lines can be expressed as

$$\frac{I_1}{I_2} = \frac{A_1 n_{2p}}{A_2 n_{2p}} = \frac{A_1 \tau_1 Q_{\mathrm{gs}\to 2\mathrm{p}_i}}{A_2 \tau_2 Q_{\mathrm{gs}\to 2\mathrm{p}_j}}, \tag{6.8}$$

The subscript 1 above represents the spontaneous emission $2\mathrm{p}_i \to 1\mathrm{s}_x$ while 2 represents that for $2\mathrm{p}_j \to 1\mathrm{s}_y$. Here s_x and s_y denote some 1s states. The rate coefficients $Q_{\mathrm{gs}\to 2\mathrm{p_i}}$ and $Q_{\mathrm{gs}\to 2\mathrm{p_j}}$ (i.e.,$Q_{\mathrm{gs}\to 2\mathrm{p_i}/2\mathrm{p_j}}$) can be expressed as in Eq. (4.28). Considering that the excitation threshold energies of the 2p states and their corresponding energies at the largest collision cross-section value, denoted as $\sigma_{\mathrm{gs}\to 2\mathrm{p}_i/2\mathrm{p}_j,\mathrm{max}}$, are close to one another, the intensity can be roughly

approximated in terms of the atomic constants:

$$\frac{I_1}{I_2} = \frac{A_1\tau_1 \int_0^\infty \varepsilon^{1/2}\sigma_{\mathrm{gs}\to 2\mathrm{p}_i} f_\mathrm{e}\mathrm{d}\varepsilon}{A_2\tau_2 \int_0^\infty \varepsilon^{1/2}\sigma_{\mathrm{gs}\to 2\mathrm{p}_j} f_\mathrm{e}\mathrm{d}\varepsilon} \simeq \frac{A_1\tau_1\sigma_{\mathrm{gs}\to 2\mathrm{p}_i,\mathrm{max}}}{A_2\tau_2\sigma_{\mathrm{gs}\to 2\mathrm{p}_j,\mathrm{max}}}. \tag{6.9}$$

In the last step it is further assumed that the two cross-sections have nearly identical shape and deviate only in their amplitudes (maximal values), $\sigma_{\mathrm{gs}\to 2\mathrm{p}_i,\mathrm{max}}$and $\sigma_{\mathrm{gs}\to 2\mathrm{p}_j,\mathrm{max}}$, respectively. Equations (6.8) and the right-most hand side of the (6.9) for the 763.5 nm/750.4 nm line ratio are plotted in Fig. 6.8, referred to as a "corona model" and an "atomic constant model." These data are presented along with the line ratios calculated from the PIC+CRM simulation and measured from the OES. As previously discussed in Sec. 6.2 and 6.3, the 763.5 nm and 750.4 nm lines strongly depend on the $n_{1\mathrm{s}_5}$ and n_gs densities, which led to the selection of this specific line ratio.

The good agreement among all cases up to around 10 Pa shows that, at these low pressures, the intensity ratio does not depend much on the plasma conditions but is rather determined by the atomic constants alone. Consequently, this ratio should not be used for diagnostic purposes of discharge at low pressures (few Pa and less). On the other hand, this provides good opportunity for checking the quality of the spectral calibration of the detector. At higher pressures, however, the line ratio becomes more sensitive to the plasma conditions. This increased sensitivity is mostly brought up by the density of the $1\mathrm{s}_5$ state, on which the 763.5 nm line intensity is highly dependent. This shows

that for a plasma with the given conditions having a pressure higher than 20 Pa, electron collisions with the metastable states already play an important role in determining optical emission and, therefore, PIC/MCC simulations is expected to yield accurate predictions for line intensity ratios only when these processes are incorporated in the numerical model self-consistently.

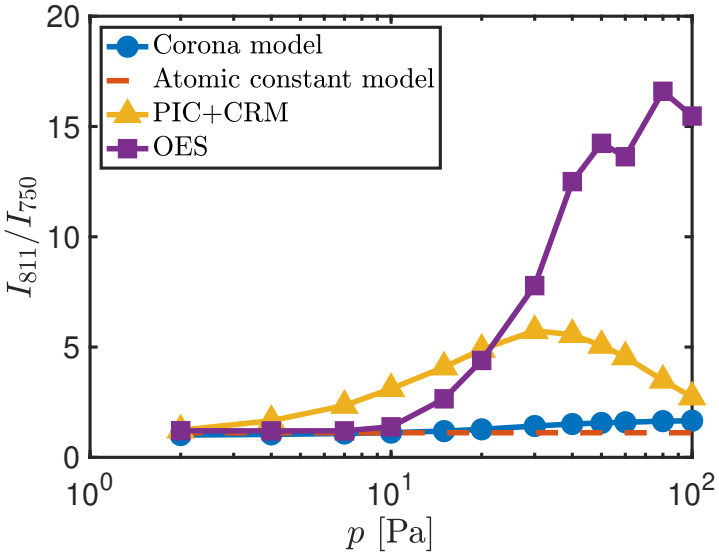

Figure 6.9: Intensity ratio of the 811.5 nm and 750.4 nm lines as measured from the OES, calculated using the corona model, PIC+CRM, and as estimated based on atomic data (see text).

Although the corona model well reproduces the line ratio I_{763}/I_{750} value obtained from the PIC+CRM simulation for pressures up to 20 Pa, this good agreement between the two models does not apply to all the intensity ratios. Figure 6.9 shows the same set of results for another intensity ratio, namely that of the 811.5 nm and 750.4 nm lines (I_{811}/I_{750}). For this line ratio, the results show that the corona model also reproduces well the experimental ratio. However, the predictions of the full PIC+CRM model show deviations already at

lower pressures. This is likely due to the behaviour of the 811.5 nm line. Indeed, this is the only line from the $2p_9$ state. Further, its lower level is the $1s_5$ metastable state so that the line is subject to self-absorption. As demonstrated in Fig. 7.10, the density of the $1s_5$ state and consequently the self-absorption for this line are not correctly represented by the PIC+CRM simulation presented in this study, which causes a poor agreement between the measured and predicted (relative) intensities for the 811.5 nm line. Naturally, other lines whose lower level is the $1s_5$ state experience the same overestimation of the radiation trapping. However, all other 2p states have alternative radiative transitions to other 1s states that generally have a lower population than the $1s_5$ state. Consequently, their populations are less influenced by the overestimation of the $1s_5$ density. This suggests that the 811.5 nm line can be a sensitive indicator to assess how well the metastable density is reproduced by the model.

6.5 Conclusions

In this work, 1D PIC/MCC simulations were conducted for symmetrical capacitively-coupled RF Ar plasma discharges with pressure ranging from 2 Pa to 100 Pa. The electron density and EEDF calculated from PIC/MCC simulation were used as input parameters to the CRM in order to model the Ar spectral line intensities. In the PIC/MCC simulations used in this study, the only ionization and excitation mechanisms taken into account were the electron-impact ionization and excitation of the ground-state Ar atoms. This is based on the

fact that at low pressure, the metastable Ar density is typically smaller by a few orders of magnitude than the ground-state Ar density and, therefore, it is commonly assumed that the stepwise ionization from excited Ar atoms, including metastables, could be neglected in PIC/MCC simulations, which allowed a significant reduction of computation time. It should be noted that, unlike the PIC/MCC simulation used here, the CRM of this study includes the stepwise ionization from all levels of excited Ar atoms included in the model.

Comparison of the simulated intensities to the OES measurements has shown that this one-way coupling of the results from the PIC/MCC simulations into the CRM simulation (i.e., the PIC+CRM simulation) can model the spectra reasonably well up to 20 Pa. At pressures above 20 Pa, however, the calculated $1s_5$ density (n_{1s_5}) continued to increase with pressure, in contrast with the measured n_{1s_5} that was found to reach saturation. Investigation of the effect of the $1s_5$ state to the ionization and excitation dynamics of the discharge has revealed that the neglect of the loss processes of the long-lived $1s_5$ metastable state in the PIC/MCC simulation can be one of the main sources for this large n_{1s_5} discrepancy in the higher pressure range. It indicates that the EEDF and the electron density obtained from the PIC/MCC simulation of this study (without the stepwise ionization), which are used as input parameters for the CRM, are not consistent with the measured optical emission spectra in this higher pressure range. The incorporation of Ar metastables (possibly along with a number of additional excited states) in the PIC/MCC simulation code[177–179] is therefore considered necessary to achieve a better agreement be-

tween the measured and computed optical emission spectra over a wide range of pressure.

The full integration of a CRM into the PIC/MCC simulation would require much longer computational time to simulate plasma dynamics as well as optical emission spectra. In contrast, the proposed PIC+CRM simulation can offer a practical solution for the prediction of optical emission spectra as long as the PIC/MCC simulation provides sufficiently accurate electron density and EEDF at a reasonable computational cost. The determination of the minimum number of Ar excited states that need to be included in such PIC/MCC simulations in the pressure range of our interest is deferred to a future study.

Chapter 7

Results: Machine learning-based prediction of plasma parameters from the optical emission spectra

In this chapter, the ML predictions of the the EEDF and n_{e} from the intensities are presented. The ML models are trained using data from the PIC+CRM method discussed in the previous chapters, with the peak-to-oeak voltage varied from 200 - 500 V to increase the dataset. These models are then used to predict test simulation data. The resulting EEDFs predicted using KRFD and ANN are presented first, followed by the n_{e} predicted by RFR. These predicted EEDFs and n_{e} are then used as input parameters for the CRM to yield intensities, which are compared to the input test intensities.

As an additional test, since experimental intensities measured for the validation of PIC+CRM are available, the ML models are also used to predict from these experimental intensities. This is presented in Sec. 7.2.

7.1 Prediction from simulated data

7.1.1 EEDF prediction

Figure 7.1 compares the EEDFs predicted by KRFD and ANN with the test EEDF data. The KRFD and ANN predictions agree very well with the test data. The excellent agreement extends over more than six orders of magnitude. The

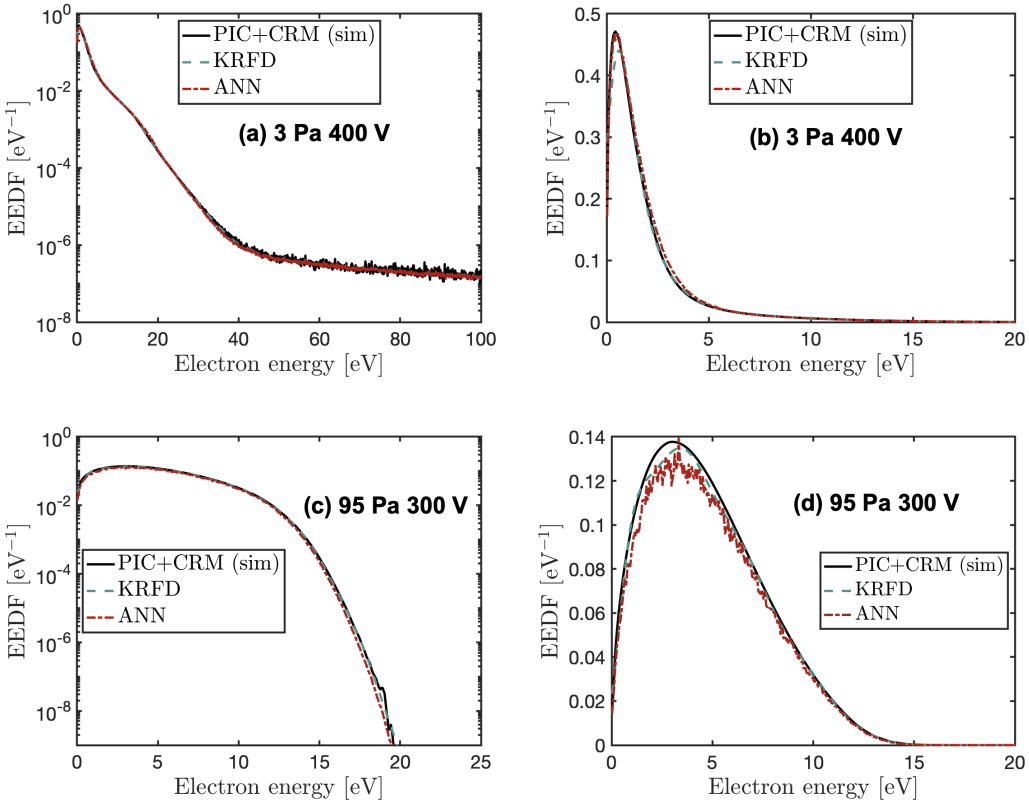

Figure 7.1: EEDF predictions at 3 Pa 400 V (a and b) and 95 Pa 300 V (c and d), presented on the logarithmic scale (a and c) and the linear scale (b and d). Each subfigure shows the EEDF predicted by KRFD, by ANN, alongside the test EEDF data from simulations, labeled as 'PIC+CRM (sim)'.

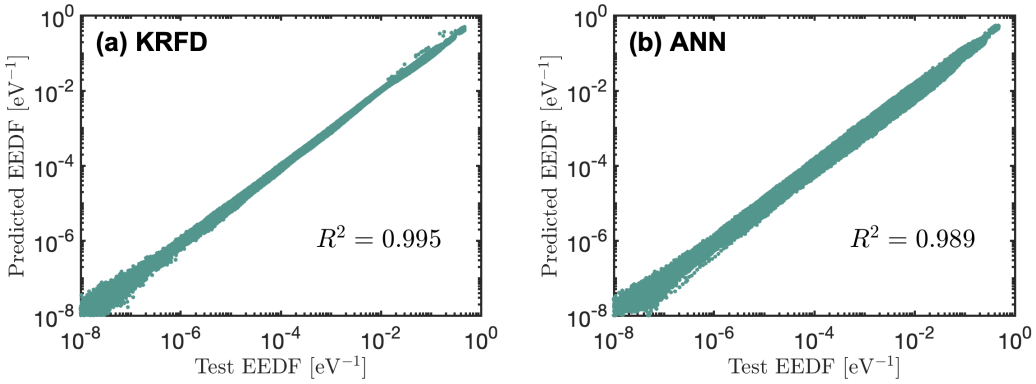

Figure 7.2: Comparison of each predicted data point of the EEDF to its corresponding test data point, as predicted using KRFD (a) and ANN (b). A perfect prediction would give a diagonal line with an R^2 of 1.

small deviations observed at low energies (below about 10 eV) are likely due to the fact that the electrons in this energy range do not participate in excitation collisions of ground-state atoms. Consequently, the emission intensities are less sensitive to this region of the EEDF and, naturally, the uncertainty here is larger. Note, however, that the low-energy electrons still participate in stepwise excitations and deexcitation collisions. Therefore, the intensities are not entirely insensitive to this population of electrons and relatively reliable information about the low-energy part of the EEDF can still be obtained.

To assess the overall performance of the EEDF prediction for all test data, predicted data points were compared to their corresponding test data values. The excellent agreement is demonstrated in Fig. 7.2. Here, each predicted point of the EEDF is plotted against the corresponding test data for both KRFD and ANN. A good model would produce a data cloud concentrated around the

$x = y$ line, with an R^2 value close to 1. The coefficient of determination R^2 is calculated by

$$R^2 = 1 - \frac{\sum_{i=0}^{n-1}(x_i - y_i)^2}{\sum_{i=0}^{n-1}(x_i - \bar{x})^2} \tag{7.1}$$

wherein x_i is a test value, y_i is a predicted value, and $\bar{x}$ is the mean of all test values. In general, both models are shown to predict the EEDF well with high R^2 values. Still, the KRFD exhibits a slightly better accuracy. Further, it is observed that the scattering around the diagonal line in Fig. 7.2 is the largest in the region of low EEDF values (below 10^{-6} eV) for both methods. This corresponds to the EEDF at high electron energies (typically above the ionization energy of the argon atoms). There the influence of the noise both in the training data as well as in the test data used for comparison is the largest, resulting in the observed larger deviation between predicted and test EEDF. Nevertheless, it is remarkable that both models are able to achieve good predictions on an arbitrary function even with a limited dataset for training.

7.1.2 Electron density prediction

In addition to the EEDF, ML is also used to predict n_e. Figure 7.3a shows the results from an RFR model. Here, the predicted n_e values are compared against the entire simulated n_e dataset used for training and testing. Overall, the predictions from the RFR model agree well with the test data, with minor deviations from the corresponding trend lines. Figure 7.3b quantifies how well

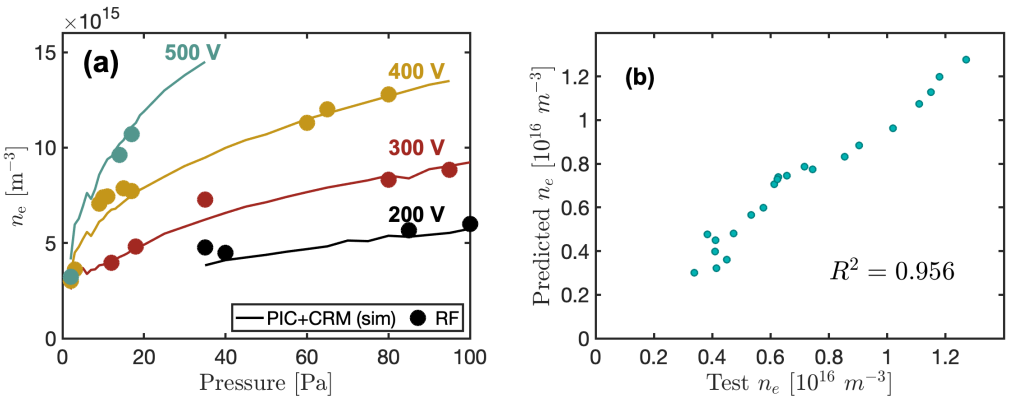

Figure 7.3: (a) The electron density n_e predicted by the RFR for each test case, plotted alongside the entire n_e training dataset. (b) Comparison of each predicted n_e value to its corresponding test data point. A perfect prediction would give a diagonal line with R^2 of 1.

these n_e predictions agree with the test data by getting the R^2 of the predicted n_e as a function of the test n_e, as is done for the EEDF.

7.1.3 Calculating spectral intensities from predicted plasma parameters

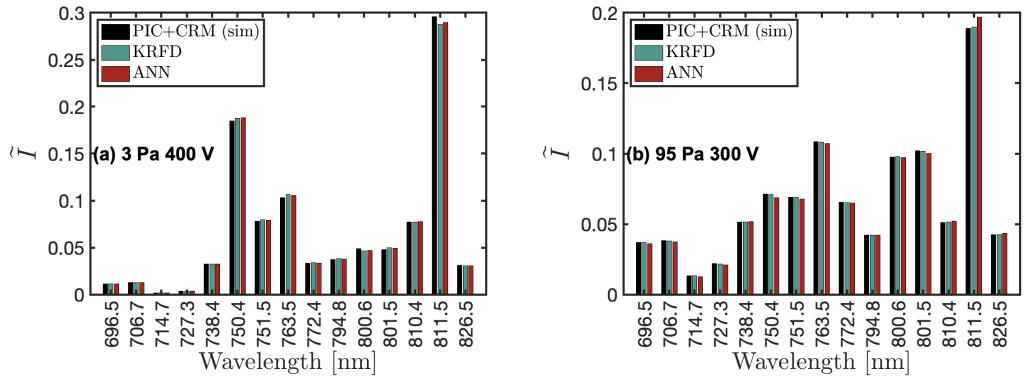

Figure 7.4: Normalized spectral line intensities at 3 Pa 400 V (a) and 95 Pa 300 V (b) calculated from the predictions of KRFD and ANN, alongside the test input spectral data from simulations, labeled as 'PIC+CRM (sim)'.

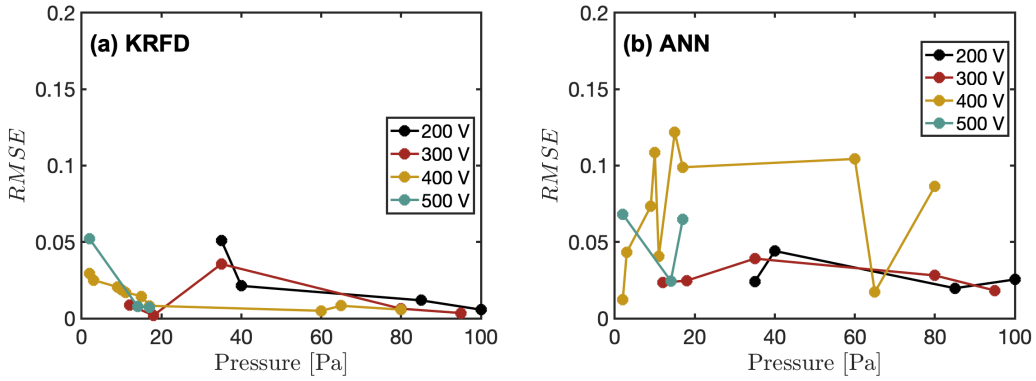

Figure 7.5: Root Mean Square Error (RMSE) of the standard deviation of the line ratios r_k (Eq. (7.2)) from the average ratio of 1 for the intensities calculated using the EEDF and n_e predicted by (a) KRFD and (b) ANN at different V_{pp} and pressures.

One test for easy assessment of the effectiveness of the ML model in accurately inverting the CRM involves feeding the predicted values of the EEDF and n_e back into the CRM and checking if the model reproduces the same intensities used for predicting these input EEDF and n_e. Figure 7.4 shows such a comparison between the input spectra and the spectra generated by the CRM using the predicted EEDF and n_e from both the KRFD and ANN at example conditions (3 Pa 400 V and 95 Pa 300 V). It is seen from the figure that both the KRFD and the ANN models effectively predict plasma parameters that reproduce the test spectral data. This strong agreement highlights the models' ability to successfully invert the CRM and accurately predict the plasma parameters for test data within the training scope.

To evaluate the agreement of the predicted line intensities with the test input data, their discrepancy is quantified similar to what was done in Ref. [8].

This is achieved by taking the ratio of the experimental relative intensities I_{OES} to the intensities calculated from simulations I_{CRM} for the wavelength values λ_k given in Appendix B, such that

$$r_k = I_{\mathrm{OES}}(\lambda_k)/I_{\mathrm{CRM}}(\lambda_k). \tag{7.2}$$

The line ratios r_k are then scaled such that the average of all r_k values in a given spectrum is unity. The root mean square error (RMSE) of the corresponding intensities to the experimental one is then calculated by:

$$RMSE = \sqrt{\frac{1}{N}\sum_{k=1}^{N}(r_k - 1)^2}, \tag{7.3}$$

where $N = 15$ is the number of spectral lines. A lower value of the RMSE shows better agreement and an RMSE of 0 means perfect agreement between the experimental and calculated intensities. Figure 7.5 shows the calculated RMSE of the predicted intensities with respect to the input test data. Relatively low RMSE values are calculated for both KRFD and ANN, with the average for KRFD generally slightly lower than that of ANN.

7.2 Prediction from experimental data

The previous section shows the predictions of the ML models when applied to test data belonging to a similar simulation dataset. In this section, the prediction results are presented for the experimentally measured intensi-

ties using the same ML models trained with the simulation data. However, as reported in Ref. [8], it is known that the simulation data deviate from the experimental data, particularly at pressures higher than 20 Pa.

7.2.1 EEDF predictions

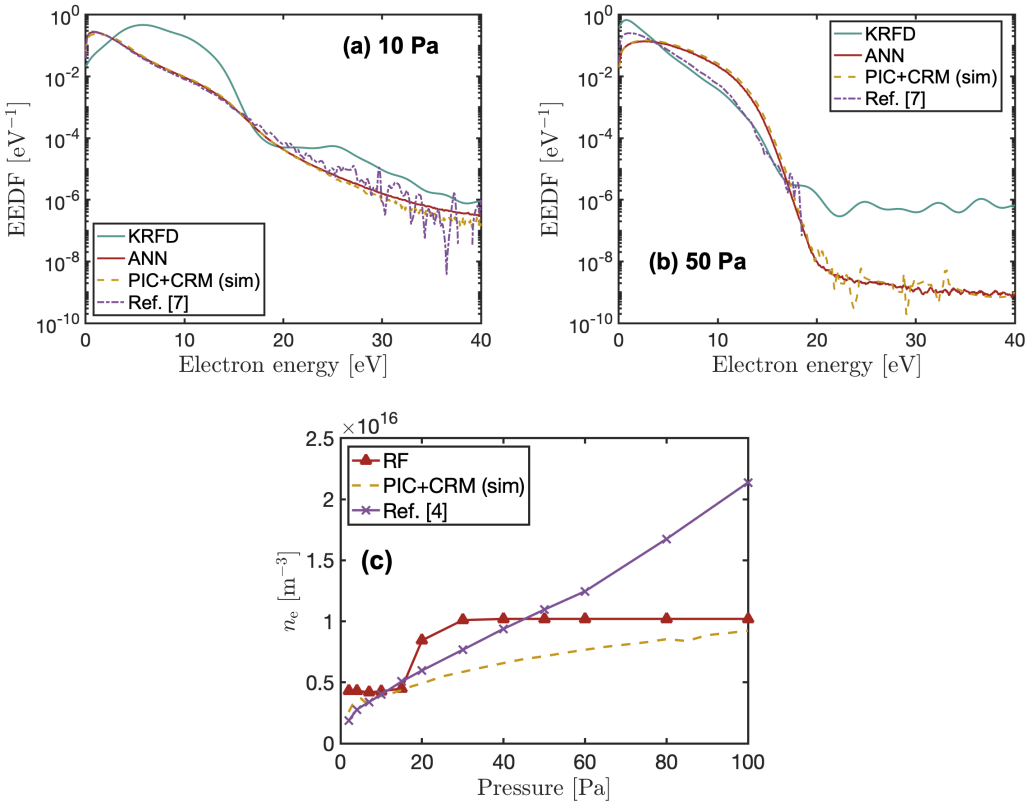

Figure 7.6: Prediction results from experimentally measured input data: predicted EEDFs using KRFD and ANN at 10 and 50 Pa, plotted alongside the EEDF from PIC+CRM simulations and from simulations by Donko, et al. ('Ref. [7]') at (a) 10 Pa, 300 V and (b) 50 Pa, 300 V. (c) n_e predicted using RF, along with the corresponding n_e from PIC+CRM simulations and from simulations by Donko, et al. ('Ref. [7]') at 300 V.

Similar to the simulation data, the EEDF and n_e are predicted from the experimentally measured spectra. Figures 7.6(a) and (b) present the EEDFs predicted from experimental spectra at 10 Pa and 50 Pa, alongside the EEDF from PIC+CRM simulations for the same experimental conditions. The comparison is made for data at a peak-to-peak voltage of 300 V since experimental spectra are available only at this condition. For reference, the EEDFs under the same conditions and calculated from the PIC/MCC+DRR simulations taken from Donko, et al.,[7] (hereby denoted as 'Ref. [7]'), are also added. Compared to the PIC/MCC simulations, the PIC/MCC+DRR model in Ref. [7] couples a basic PIC/MCC code with a diffusion-reaction-radiation (DRR) model to take into account all the processes involving the excited states. This approach demonstrates a good agreement of the calculated intensities with the experimentally measured ones.

The ANN predictions closely replicate the EEDFs from the PIC+CRM simulation (Figures 7.6(a) and (b)). Even at 50 Pa (Figure 7.6(b)), where the simulated intensities do not agree well with the experimentally measured ones, the ANN reproduces the EEDF from the corresponding simulation well. It is possible that the ANN has learned to place a higher weight on the pressure during its training. At 10 Pa, the EEDF calculated from Ref. [7] agrees closely with that from PIC+CRM simulations and therefore with the ANN predictions. On the other hand, the EEDFs predicted by KRFD do not agree well with the simulation data it is trained with. At 10 Pa, the KRFD predicted an EEDF that deviates from both simulation results. Moreover, the EEDFs appear "bumpy"

in contrast to the ANN predictions. This is likely an artefact of the chosen kernel function (Eq. (5.1)). At 50 Pa, however, the KRFD predictions agree closer to that from Ref. [7] than that from PIC+CRM simulations. This is an interesting effect, considering that the training of the KRFD involved EEDFs with a rather different shape at these conditions (see the PIC+CRM curve in Fig. 7.6(b)).

7.2.2 Electron density predictions

Similar to the simulation data, an RFR model was used to predict n_e from experimentally measured spectra. Fig. 7.6(c) shows n_e values predicted by RF, along with the training data and n_e obtained in Ref. [7]. In this case, we do not observe the same pressure dependence of the predicted n_e as seen in the PIC+CRM or that from Ref. [7]. Instead, the predicted n_e values seem to fall into two distinct regions: low pressure (below 20 Pa) and high pressure (above 20 Pa). In each region, n_e values remain nearly constant. It was already demonstrated that the developed ML models provide a good inverse of the CRM. The unexpected behaviour of n_e predicted from experimental spectra likely hints towards the fact that the CRM itself might not provide a good description of the actual processes in the experiment and would require an extension. However, this goes beyond the scope of the current work.

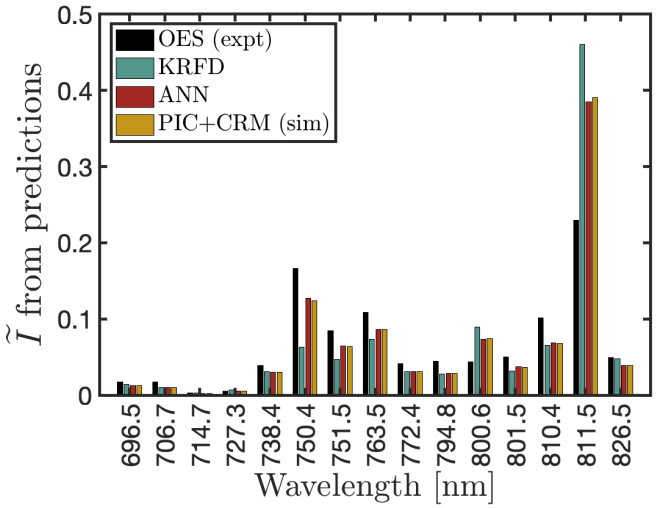

Figure 7.7: Normalized intensities at 10 Pa and 300 V peak-to-peak voltage calculated from the predictions of KRFD and ANN obtained by feeding the experimental spectra. For comparison, the underlying experimentally measured intensities denoted as 'OES (expt)' together with the spectrum from simulations 'PIC+CRM (sim)' with the same conditions are also presented. The latter data were also part of the training dataset.

7.2.3 Calculating spectral intensities from predicted plasma parameters

The prediction for the EEDF and n_e from the experimental intensities are fed back into the CRM to calculate the corresponding intensities. This is done to investigate to what extent the inversion of the CRM by the ANN and the KRFD works with experimental spectra. An example of these results is shown in Fig. 7.7, that is for the 10 Pa case. As is the case for the predicted EEDF, the intensities from the ANN predictions yield intensities that closely agree with the PIC+CRM simulations. Given that the simulations show better agreement

with experiments at low pressures, the ANN is also able to yield good results at low pressures.

The close agreement between the ANN predictions and the simulation spectra might seem surprising at first, given that for pressures below 20 Pa there is a factor of about 2 discrepancy between the electron densities used for generating these spectral data (Fig. 7.6(c)). However, as demonstrated in Ref. [8], the emission intensities calculated by this CRM have a strong linear dependence on n_e and a much weaker non-linear contribution. Then using a normalization of the emission intensities to their sum removes the strong linear dependence on n_e, leaving only the much weaker non-linear contribution which makes for the slight differences in the intensities by ANN and PIC+CRM seen in Fig. 7.7.

The intensities obtained from the KRFD predictions at 10 Pa significantly deviate from the experimental values (Fig. 7.6(a)). This is likely due to the non-negligible differences in the EEDF predicted by KRFD from the actual EEDF (Fig. 7.6(a)). Particularly the deviations in the region of electron energies close to the excitation thresholds for Ar (11-15 eV) are probably the main cause for the discrepancies observed in the spectral intensities.

In the pressure range above 20 Pa, it is known[8] that the intensities calculated by PIC+CRM deviate from the experimental measurements. It is thus of relevance to investigate how the intensities calculated from the CRM with the EEDF and n_e predicted by the ANN and KRFD from the experimental intensities compare to the actual experimental spectra, i.e. to what extent the ANN

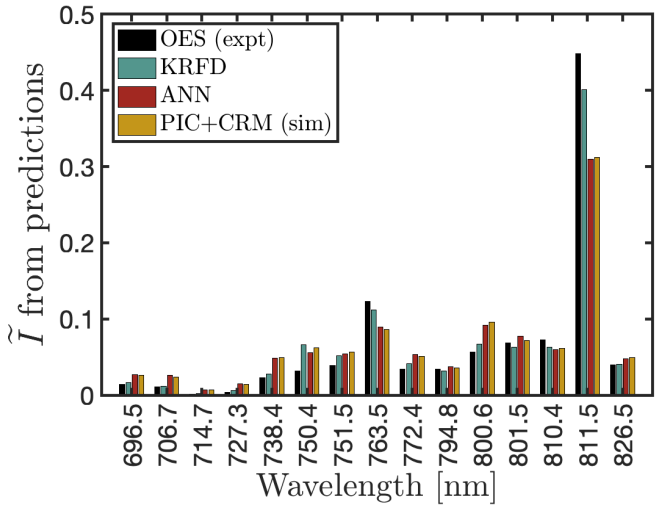

Figure 7.8: Normalized intensities at 50 Pa and 300 V peak-to-peak voltage calculated from the predictions of KRFD and ANN obtained by feeding the experimental spectra. For comparison, the underlying experimentally measured intensities denoted as 'OES (expt)' together with the spectrum from simulations 'PIC+CRM (sim)' with the same conditions are also presented. The latter data were also part of the training dataset.

and the KRFD can invert the CRM for spectra from the experiment. Such a comparison is plotted in Fig. 7.8 for the 50 Pa case. Here, similar observations can be made about ANN as before: it replicates the PIC+CRM results. Notably, it does so even with the larger difference in n_e in this pressure range (Figure 7.6(c)). This is again likely an artefact of the normalization of the intensities. However, since at higher pressures the PIC+CRM data deviate from the experimental data, the resulting intensities from ANN do not agree with the experimental one at 50 Pa. Surprisingly, the KRFD predictions result in intensities that are in better agreement with the experimental intensities. This is likely related to the

better agreement of the KRFD prediction for the EEDF with the more realistic simulations of Ref. [7].

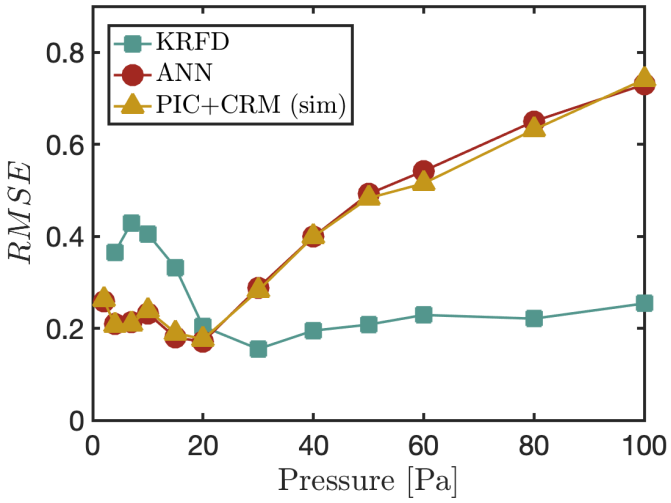

Figure 7.9: Root Mean Square Error (RMSE) of the ratios r_k of the intensities from 'PIC+CRM' and from KRFD and ANN predictions, to the the experimentally measured intensities at a peak-to-peak voltage of 300 V.

The differences in the calculated spectra from the experimentally measured ones is quantified through the RMSE (Eq. (7.3)). The resulting RMSE for KRFD, ANN and the PIC+CRM case are shown in Fig. 7.9. As expected, the ANN results closely follow the trend of PIC+CRM while KRFD shows a different behavior. It shows poorer agreement (a higher RMSE) at low pressures and better consistency (a relatively lower RMSE) with the experimental spectra at higher pressures (above about 20 Pa). At the lowest pressure (2 Pa), the EEDF predicted by KRFD did not allow the CRM code to converge and a data point is thus missing for this case.

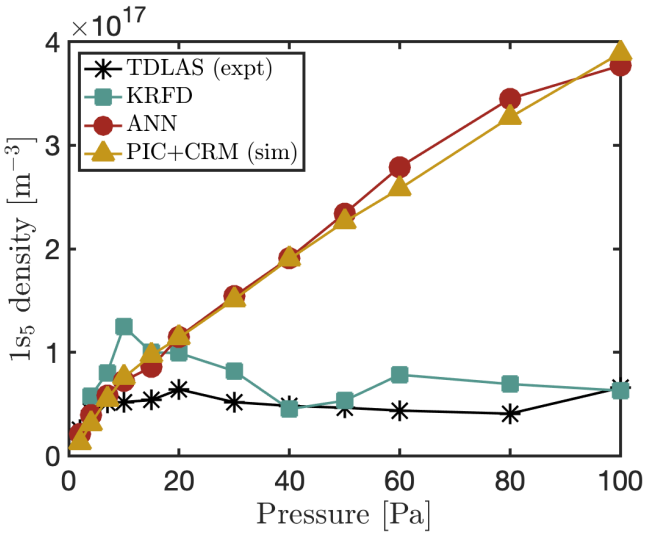

Figure 7.10: The Ar $1s_5$ metastable density as measured by TDLAS,[8] simulated using PIC+CRM,[8] and calculated from the predictions from KRFD and ANN via the CRM at a peak-to-peak voltage of 300 V.

In addition to the intensities, the density of the lowest excited state of argon, $1s_5$, is also calculated from the CRM. In Ref. [8], $1s_5$ density from the PIC + CRM simulations and the TDLAS experiments are compared. Figure 7.10 shows the same TDLAS data, which is given along with the resulting $1s_5$ density obtained from PIC+CRM simulations and those predicted using plasma parameters from ML. Unsurprisingly, the ANN and the PIC+CRM values are very close. At low pressures, they also follow the TDLAS data. However, at high pressures (above 20 Pa), the predicted $1s_5$ density from ANN continuously increases and deviates from the experimental measurements. Conversely, the KRFD predictions show poor agreement with the experiment at low pressures but surprisingly good agreement at high pressures.

7.3 Conclusions

In this study, ML models were developed to predict the normalized EEDF and n_{e} of Ar plasma from its relative (i.e., normalized) optical emission line intensities at various gas pressures. The models were trained on 86 sets of numerical simulation data obtained from the 1D PIC/MCC simulation code coupled with a CRM code described in Ref. [8] for Ar CCPs under various discharge conditions. Two different types of models, i.e., KRFD and an ANN were used to predict the normalized EEDF and the RFR was used to predict n_{e}. The input data for the ML models are the gas pressure and the relative emission line intensities. When the simulated OES data were used for the input data, the ML models predicted the corresponding EEDF and n_{e} with high accuracy. In other words, the ML models developed in this study performed well for what they were trained for.

The simulation data of Ref. [8] are known to agree well with experimental data at a gas pressure of up to about 20 Pa. However, even under these conditions, some discrepancy always exists between the simulated and experimentally measured OES data. The discrepancy stems from various reasons, ranging from the inaccuracy of the CRM to the profile effects of the three-dimensional actual plasma. If the developed ML models are robust enough, they may also work for the experimentally measured OES data used as their input data for a gas pressure of up to about 20 Pa. The robustness of the ML models developed in this study was then tested. It was found that the ANN-based ML model was

able to predict the normalized EEDF reasonably well at a pressure of 20 Pa or lower for the experimentally obtained relative line intensities and the gas pressure. However, under the same conditions, the predictions by the KRFD-based ML model exhibited relatively large errors. The RFR model for n_{e} was not able to show the pressure dependence under the same conditions and therefore not satisfactory. The results show that, in general, the ML models, which were trained only with the simulation data and performed well with simulated OES data, were not robust enough to handle the discrepancy between the simulated and experimental OES data.

Therefore the future direction of this study includes the improvement of the robustness of the ML models. However, a fundamental question remains as to whether the relative emission line intensities contain sufficient information on the electron density and its energy distribution. Although the optical emission's relative line intensity spectrum may depend on n_{e}, the dependence may be too subtle to be detected if other effects modify the spectrum shape. Furthermore, the emission spectra are likely to be affected more sensitively by a particular energy range of the EEDF than the others. Therefore, different EEDFs can give rise to similar OES spectra. These issues will also be addressed in future work.

The recent study of Ref. [7] performed 1D PIC/MCC simulations with stepwise excitation and ionization and a self-consistent CRM, which produced OES line intensity data in good agreement with the experimental data for Ar CCPs at a gas pressure up to 100 Pa. Training of the ML models presented here

with large-scale simulation data generated by the simulation code of Ref. [7] can make these models valid in all pressure ranges.

Using the EEDF presented in Ref. [7], we also tested the current ML models of this study at a high pressure of up to 100 Pa with experimentally obtained relative optical emission line intensities. As discussed earlier, the current ML models were not trained for the actual plasma at a pressure higher than 20 Pa (where the training simulation data do not agree well with the experimental data) Therefore, it is not surprising that most predictions failed under these conditions. However, the KRFD-based ML model predicted the EEDF and other plasma properties similar to those data obtained from the latest numerical simulations given in Ref. [7] at a pressure above 20 Pa. The KRFD-based ML model was not trained for such discharges and therefore these predictions should not be trusted. Nevertheless, the KRFD-based ML model's seemingly good performance at high pressure reflects some nature of optical emission spectra of Ar discharges and its discussion is deferred to a future study.

Chapter 8

Results: Optical emission analysis of carbon impurity ion parameters in fusion plasmas

In this study, the potential of using the SHS for CXS in order to achieve a higher optical transmission-to-spectral resolution ratio is investigated. The SHS is used to measure the toroidal flow velocity V_f and carbon impurity ion temperature $T_{C^{6+}}$ in the LHD by CXS. The results are compared to that from a DS, which is typically used in CXS in the LHD.

To characterize the spectral resolution, the IW of both the DS and SHS are first compared. The characteristics of the LHD shot in which this study is conducted are then presented. This is followed by the analysis and transformation of the interferogram measured by the SHS. Lastly, the resulting V_f and $T_{C^{6+}}$ from both spectrometer types are compared.

8.1 Comparison of instrumental width of DS and SHS

The spectral resolution of a spectrometer can be characterized by a parameter called the IW. IW is defined to be the full width at half maximum (FWHM) of the instrumental line profile (ILP).

In this study, the FWHM of the ILP is measured for both the SHS and the DS by adjusting the spectrum line width of the light from the TLS at 529 nm. A single optical fiber is used to transfer the light from the TLS to the SHS and DS.

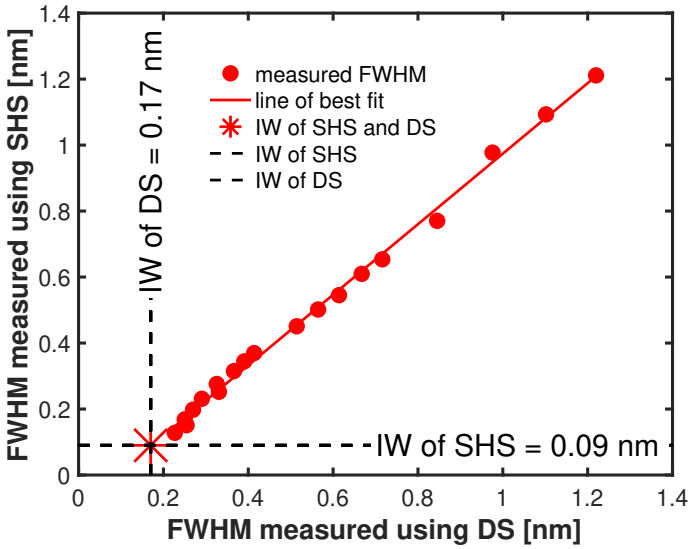

Figure 8.1: FWHM measured with the SHS and the DS along with the IW values

The IW is extrapolated to be the value of the FWHM when the spectrum line width is zero, and is given in Fig. 8.1 for both spectrometers.

In Fig. 8.1, the FWHM measured using the DS and the SHS are plotted along with its line of best fit. The almost linear behavior of the fitted line shows a good agreement between the FWHM measured from both spectrometers. Therefore, the SHS has the ability to measure the FWHM correctly as well as a DS does. The IW of the SHS was extrapolated to be 0.09 nm, which is almost half of that of the DS (IW = 0.17 nm). Comparing the optical transmission of the two optical systems, the aperture size of the SHS and the DS are calculated to be 16.77 mm^2 and 2.6 mm^2 respectively. Another way to express the optical

transmission is through a parameter called etendue (G) which is calculated by

$$G = S\sigma = S\frac{\pi}{4F^2} \tag{8.1}$$

where S is the aperture size, σ is the solid angle, and F is the F-number. The F-number of the SHS and the DS are 2.1 and 2.8 respectively. The values of the etendue of the SHS and the DS are therefore calculated to be 2.9867 mm^2sr and 0.2605 mm^2sr respectively. These significant differences in the etendue and the instrumental width presents the SHS as a suitable instrument for measurements requiring high spectral resolution and high optical transmission.

8.2 Discharge characteristics

SHS and DS measurements were done using Shot # 164208 of the LHD. Fig. 8.2 shows the discharge characteristics of this shot. The first subfigure shows the beam power of the neutral beams. Here, 'NB#1-3' is the sum of the power from neutral beams 1-3. NB#4, NB#5, and ECH represent the power from NB#4, NB#5, and the electron cyclotron heating (ECH) respectively. It can be seen that during beam modulation, NB#4 and NB#5 were turned on for a longer duration than they were turned off. This allowed for more time-resolved data of the ion parameters. The second subfigure shows the power of the NB#5 plotted alongside the time-dependent intensity derived from the SHS interferogram after FFT. The intensity values were calculated by integrating the spectra from 528.5 nm to 529.7 nm. This shows how the intensity is directly

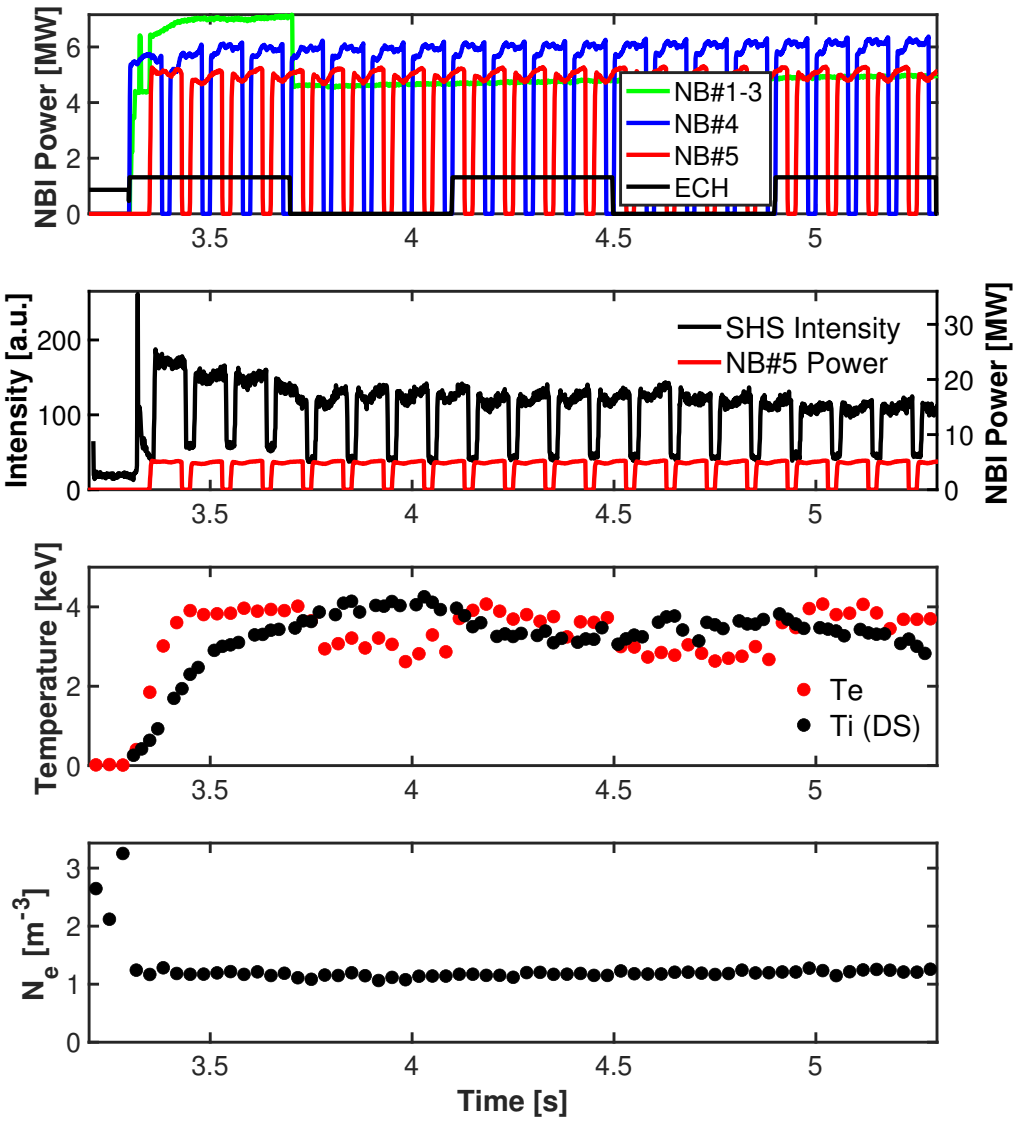

Figure 8.2: Parameters of LHD Shot # 164208

proportional to the NB#5 power. The third and fourth subfigures show the $T_{C^{6+}}$, the electron temperature (T_e) and the electron density (n_e). Here, the T_e and the n_e were measured by Thomson scattering while the $T_{C^{6+}}$ was measured using the DS. The T_e and $T_{C^{6+}}$ are observed to increase and decrease following the ECH modulation.

8.3 Interferogram and corresponding spectra measured using SHS

Fig. 8.3 shows the resulting SHS interferogram and spectra from Shot # 164208. Measurements were taken at t = 3.4 s (Fig. 8.3(a)) and t = 4.0 s (Fig. 8.3(b)). The first subfigures show the raw interferograms directly measured from the SHS. The second subfigures show the intensity derived after FFT('Background+NBCXS'), along with the background emission ('Background'). The background emission is calculated by interpolating the neighboring time frames when the NB#5 was turned off. This background emission is then subtracted from the raw intensity to get the CXS intensity induced by NB#5 ('NBCXS Intensity') shown in the third subfigures. The resulting spectra are then fitted to a Gaussian curve.

The Gaussian fit of a spectrum is represented by the equation

$$F(\lambda) = I\exp[-\frac{(\lambda-\lambda_p)^2}{w^2}] + A, \tag{8.2}$$

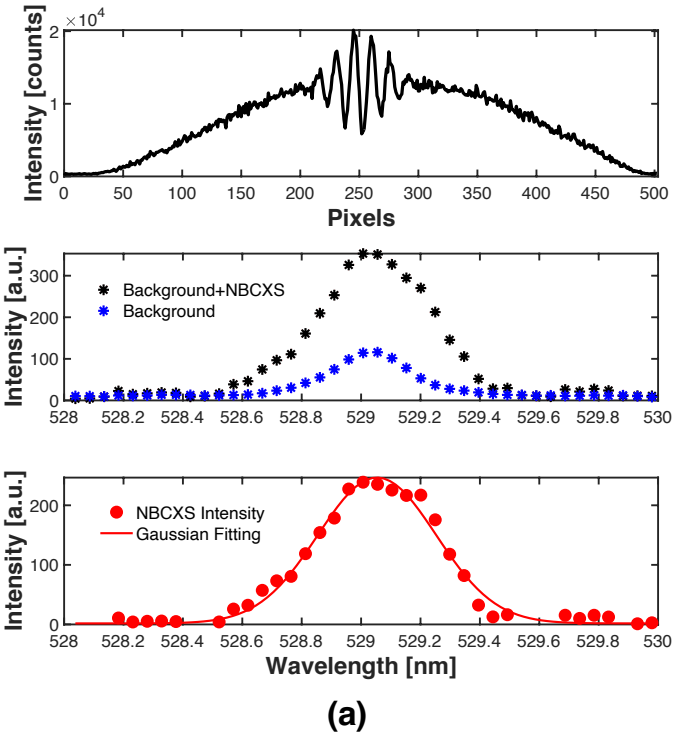

Figure 8.3: SHS signal and spectra at (a) t = 3.4 s ($T_{C^{6+}}$ = 2.76 keV) and (b) t = 4.0 s ($T_{C^{6+}}$ = 4.38 keV)

where I is the height of the spectrum peak, λ is the corresponding wavelength, λ_p is the peak position, w is the width of the Gaussian curve, and A is the vertical offset from 0. Non-linear least square fitting was done in order to fit the values of I, λ_p, w, and A into Eq. 8.2. The V_f and the $T_{C^{6+}}$ can then be calculated from the resulting λ_p and w values. The distance of the λ_p from the standard charge exchange line peak (λ_C) at 529.05 nm yields the Doppler shift. From this value, V_f can be calculated using the equation

$$V_f = c\frac{\mid \lambda_p - \lambda_C \mid}{\lambda_C} \tag{8.3}$$

where c is the speed of light.

Similarly, w gives the width of the spectrum after Doppler broadening. From this width value, the $T_{C^{6+}}$ is calculated using the equation

$$T_{C^{6+}} = \frac{Am_p[(w^2 - w_{SHS}^2)^{0.5}c/\lambda_C]^2}{2}. \tag{8.4}$$

where A is the atomic mass of carbon, m_p is the proton mass, and w_{SHS} is the Gaussian width induced by instrumental broadening. w_{SHS} is directly related to the IW calculated in Sec. 8.1. However, in the case of the w_{SHS}, instead of using the FWHM, the half-width at the height of e^{-1} is used. w_{SHS} is therefore calculated from the IW using the equation

$$w_{SHS} = \frac{IW}{2\sqrt{ln2}}. \tag{8.5}$$

In Fig. 8.3, the measurements from t = 3.4 s and t = 4.0 s were taken because the calculated $T_{C^{6+}}$ is observed to be lowest at t = 3.4 s and highest at t = 4.0 s. Actually, if the figure is looked into closer, one can see that the relative level of the $T_{C^{6+}}$ can already be observed even from the interferogram given on the first subfigure of Fig. 8.3(a) and Fig. 8.3(b). Higher sine wave modulation (given at the peak of the interferogram) is present when a lower Doppler width is measured (t = 3.4 s), while a lower sine wave modulation is present at a higher Doppler width (t = 4.0 s). The Doppler width is then observed more clearly after FFT, shown by the width of the spectral line in the second and third subfigures. This observation allows for a relative guess of the $T_{C^{6+}}$ even just from the measured interferograms.

Wavelength values for the derived spectrum are then calculated using the equation

$$\frac{1}{\lambda}[nm^{-1}] = (\frac{M\sigma_D}{4\text{tan}\theta - (8\text{tan}\beta_i/n\sigma_0)(dn/d\lambda)} + \sigma_0) \times 10^7 \tag{8.6}$$

where M is the magnification of the telecentric lens, σ_D is the spatial frequency of the waveform (in mm^{-1}), σ_0 is the Littrow wavenumber corresponding to the Littrow wavelength λ_0, n is the refractive index of the grating at λ_0, β_i is the angle of incidence, and $dn/d\lambda$ is the rate of change of the refractive index at λ_0. The resulting SHS spectrum is shown in Fig. 8.4(a), and is plotted along with that of the DS. Here, the SHS and the DS spectra are both passive and were taken at a pulse around t = 4.0 s from another LHD shot (Shot # 163968).

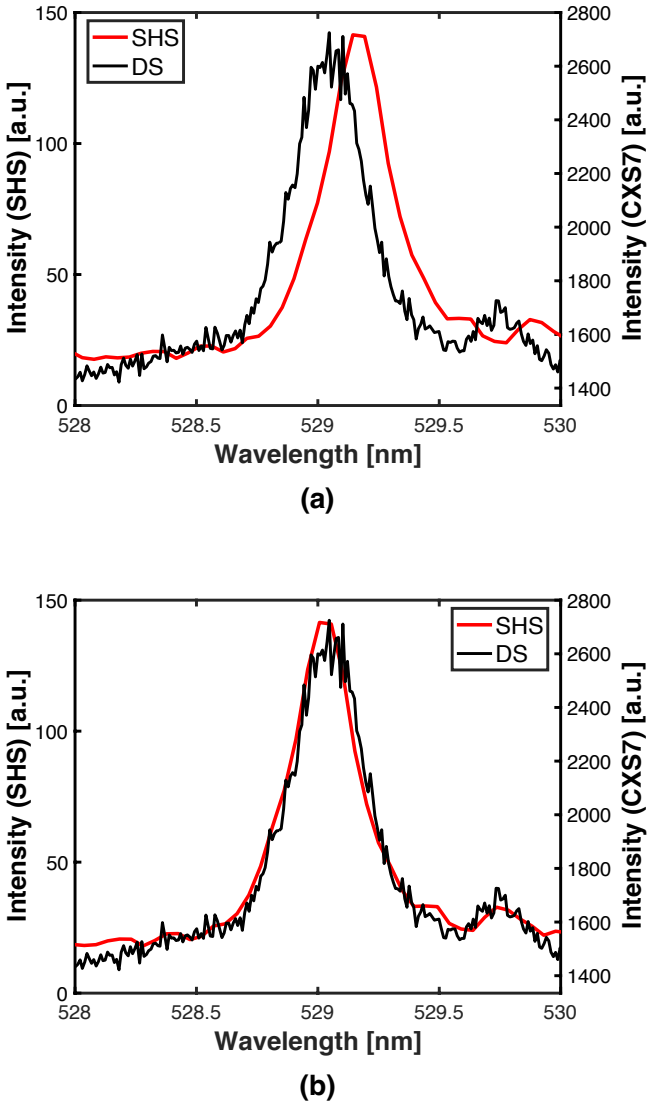

Figure 8.4: SHS and DS spectra (a) before adjustment ($\lambda_0 = 530.8$ nm) and (b) after adjustment ($\lambda_0 = 530.66$ nm)

From this figure, it can be seen that the peaks of the SHS and DS spectra do not match. The Littrow wavelength used in Eq. 8.6 is therefore adjusted in such a way that the SHS peaks matched those of the DS, resulting in the figure given in Fig. 8.4(b). Here, the Littrow wavelength of 530.8 nm measured from the calibration is adjusted to 530.66 nm to match the peaks. The Littrow angle for Eq. 8.6 is then calculated from this new Littrow wavelength value using the equation

$$\theta = sin^{-1}(\frac{N\lambda_0}{2}), \tag{8.7}$$

where N is the grating groove density. This discrepancy in the peak position is attributed to the changes in the Littrow wavelength caused by environmental temperature and pressure changes.

Wavelength adjustment was chosen to be done in such a manner due to the sensitivity of the SHS to environmental conditions. Although the SHS and the DS are measuring the toroidal flow from opposite directions, the position of the DS peak shows that the Doppler shift due to the cold component is < 0.01 nm, which is small compared to the 0.14 nm adjustment applied on SHS spectra.

8.4 Comparison of flow velocity and ion temperature measured using DS and SHS

Fig. 8.5 shows the resulting time-dependent V_f and $T_{C^{6+}}$ values, along with the values measured from the DS. The V_f and $T_{C^{6+}}$ values from the SHS

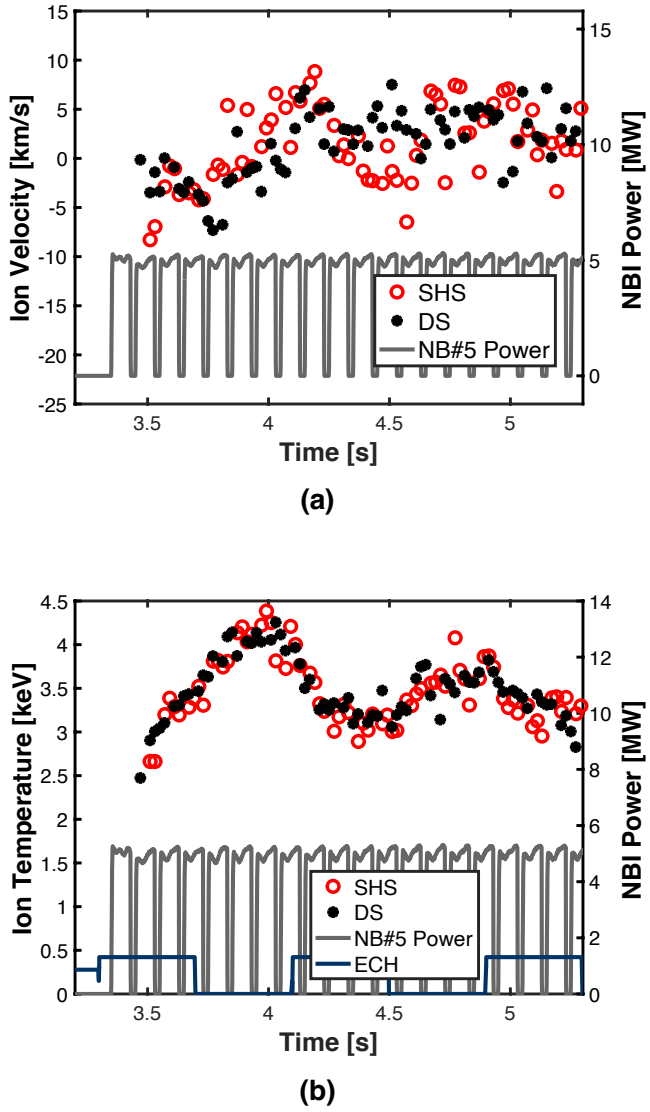

Figure 8.5: (a) Toroidal flow velocity (V_f) and (b) carbon impurity ion temperature ($T_{C^{6+}}$)

are averaged for every 20 ms interval. It can be observed that the resulting $T_{C^{6+}}$ measured from the SHS has the same trend and is in good agreement with that measured using the DS. Both $T_{C^{6+}}$ measurements show the alternating high-low temperature that went with the ECH modulation. In the case of V_f, values measured from the SHS and DS are observed to be scattered, but the two measurements are found to be in the same range and same general trend. This good agreement shows how the SHS can be used for CXS measurements with the advantage of having a higher resolution at higher optical transmission than a traditional DS.

8.5 Conclusion

In this study, charge exchange spectroscopy (CXS) in the Large Helical Device (LHD) is performed using a spatial heterodyne spectrometer (SHS) in order to achieve higher spectral resolution even at higher optical transmission. To characterize the spectral resolution, the IW of the SHS is measured and compared to that of a traditional dispersive spectrometer (DS). The instrumental width of the SHS (IW = 0.09 nm) is extrapolated to be almost half of that of the DS (IW = 0.17 nm) even though the SHS (aperture size = 16.77 mm^2, etendue = 2.9867 mm^2sr) has a higher optical transmission than the DS (aperture size = 2.6 mm^2, etendue = 0.2605 mm^2sr). Additionally, the SHS was used to measure the toroidal flow velocity (V_f) and the ion temperature ($T_{C^{6+}}$) of the C^{6+} impurity present in the LHD. The interferogram measured from the SHS is transformed

into spectra using Fourier transform. V_f and $T_{C^{6+}}$ are then calculated from the Doppler shift and Doppler width of the Gaussian fitting of the spectra derived. The calculated V_f and $T_{C^{6+}}$ are shown to be in good agreement with the values measured using the DS.

Chapter 9

Conclusions

In this work, we addressed specific challenges related to the determination of plasma parameters by optical spectroscopy. First, the accuracy of existing models in simulating spectral intensities given a set of plasma parameters was initially validated by comparing the normalized spectral intensities to measured ones. A PIC/MCC simulation code was utilized to calculate electron density n_e and electron energy distribution function, which were then used as input parameters for the CRM. Comparing the simulated intensities to OES measurements demonstrated that this one-way coupling of results from PIC/MCC simulations and CRM simulation works reasonably well up to 20 Pa. However, at pressures exceeding 20 Pa, the loss processes of metastable states (which are neglected in basic PIC/MCC simulations) become significant. Subsequent research revealed that accounting for the loss processes of these excited states in a 1D PIC/MCC-DRR simulation resulted in intensities that could model the spectra effectively.

After establishing the relationship between plasma parameters and spectral line intensities using simulation models, these models were utilized to generate additional data required for training a supervised ML model capable of predicting plasma parameters using spectral lines. ML models demonstrated high accuracy in predicting the normalized EEDF and n_e when simulated OES

data were employed as input data. When experimentally obtained OES data were used as input, the ANN reasonably predicted the normalized EEDF under plasma conditions where simulation data align well with experimental observations. Although the ML models performed well for the data similar to what they were trained on (simulation data), further development and increase in training data in order to build a more robust model that can extend to a more diverse dataset (i.e., experimental data).

Subsequently, we tackled the challenge of employing spectroscopic techniques to measure plasma parameters amidst fluctuations and instabilities occurring in magnetically confined plasmas over short periods (approximately $100\mu s$). An SHS was utilized in the measurement of the toroidal flow velocity and temperature of the C^{6+} impurity ion by charge exchange spectroscopy. This was done to achieve higher spectral resolution, even at higher optical transmission rates. To characterize the spectral resolution, the instrumental width of the SHS was measured and compared to that of a traditional Dispersive Spectrometer (DS). The instrumental width of the SHS (IW = 0.09 nm) was measured to be half of the DS (IW = 0.17 nm), despite having a much larger aperture size. Comparison of the toroidal flow V_f and ion velocity $T_{C^{6+}}$ of the C^{6+} ion between the two spectrometers showed a good agreement.

Our contributions propel us closer to achieving more precise real-time monitoring of plasma in both low-temperature and fusion environments. Especially in low-temperature plasma, where non-invasive monitoring and feedback are crucial for virtual metrology, our advancements improve production

yield and reduce product loss. We see this work as a significant stride towards this objective. While there is still much to accomplish, we aspire for our efforts to encourage further exploration in this critical research direction.

REFERENCES

[1] N Sadeghi, DW Setser, A Francis, U Czarnetzki, and HF Döbele. Quenching rate constants for reactions of ar (4p+[1/2], 4p [1/2], 4p [3/2] 2, and 4p [5/2] 2) atoms with 22 reagent gases. *The Journal of Chemical Physics*, 115(7):3144–3154, 2001.

[2] RSF Chang and DW Setser. Radiative lifetimes and two-body deactivation rate constants for ar ($3p^5$, 4p) and ar ($3p^5$, 4p+) states. *The Journal of Chemical Physics*, 69(9):3885–3897, 1978.

[3] Av V Phelps. The application of scattering cross sections to ion flux models in discharge sheaths. *Journal of applied physics*, 76(2):747–753, 1994.

[4] Hayashi database. `www.lxcat.net`. Accessed: 2022-07-20.

[5] Large helical device (lhd) project. `https://www-lhd.nifs.ac.jp/pub/LHD_Project_en.html`. Accessed: May 2, 2024.

[6] Principle of icp optical emission spectrometry (icp-oes). `https://www.hitachi-hightech.com/global/products/science/tech/ana/icp/descriptions/icp-oes.html`. Accessed: 2010-09-30.

[7] Zoltan Donkó, Tsanko Vaskov Tsankov, Peter Hartmann, Fatima Jenina Tolentino Arellano, Uwe Czarnetzki, and Satoshi Hamaguchi. Self-consistent calculation of the optical emission spectrum of an argon capacitively coupled plasma based on the coupling of particle simulation with a collisional-radiative model. *Journal of Physics D: Applied Physics*, 2024.

[8] Fatima Jenina Arellano, Márton Gyulai, Zoltán Donkó, Peter Hartmann, Tsanko V Tsankov, Uwe Czarnetzki, and Satoshi Hamaguchi. First-principles simulation of optical emission spectra for low-pressure argon plasmas and its experimental validation. *Plasma Sources Science and Technology*, 32(12):125007, 2023.

[9] H Conrads and M Schmidt. Plasma generation and plasma sources. *Plasma sources science and technology*, 9(4):441, 2000.

[10] Gottlieb S Oehrlein and Satoshi Hamaguchi. Foundations of low-temperature plasma enhanced materials synthesis and etching. *Plasma Sources Science and Technology*, 27(2):023001, feb 2018.

[11] Klaus-Dieter Weltmann, Juergen F. Kolb, Marcin Holub, Dirk Uhrlandt, Milan Simek, Kostya (Ken) Ostrikov, Satoshi Hamaguchi, Uros Cvelbar, Mirko Cernak, Bruce Locke, Alexander Fridman, Pietro Favia, and Kurt Becker. The future for plasma science and technology. *Plasma Processes and Polymers*, 16(1):1800118, 2019.

[12] Igor Adamovich, Sumit Agarwal, Eduardo Ahedo, Luís Lemos Alves, Scott Baalrud, Natalia Babaeva, Annemie Bogaerts, Anne Bourdon, PJ Bruggeman, C Canal, et al. The 2022 plasma roadmap: low temperature plasma science and technology. *Journal of Physics D: Applied Physics*, 55(37):373001, 2022.

[13] Karsten Arts, Satoshi Hamaguchi, Tomoko Ito, Kazuhiro Karahashi, Harm Knoops, Adriaan Mackus, and Wilhelmus MM Kessels. *Plasma Sources Sci. Technol.*, 31:103002, 2022.

[14] Jan Benedikt, Holger Kersten, and Alexander Piel. Foundations of measurement of electrons, ions and species fluxes toward surfaces in low-temperature plasmas. *Plasma Sources Science and Technology*, 30(3):033001, 2021.

[15] R Engeln, B Klarenaar, and O Guaitella. Foundations of optical diagnostics in low-temperature plasmas. *Plasma Sources Science and Technology*, 29(6):063001, 2020.

[16] Alfven case study – pulsed rf plasma monitoring critical for 7nm and beyond. `https://www.impedans.com/case-study-pulsed-rf-plasma-monitoring-critical-for-7nm-and-beyond` Accessed: 2024-02-04.

[17] PKS Prakash and Sean F McLoone. Plasma etch process virtual metrology using aggregative linear regression. In *2011 International Conference of Soft Computing and Pattern Recognition (SoCPaR)*, pages 538–543. IEEE, 2011.

[18] Y Kasashima, H Kurita, N Kimura, A Ando, and F Uesugi. Monitoring of inner wall condition in mass-production plasma etching process using a load impedance monitoring system. *Japanese Journal of Applied Physics*, 54(6):060301, 2015.

[19] Masanaga Fukasawa, Atsushi Kawashima, Nobuyuki Kuboi, Hitoshi Takagi, Yasuhito Tanaka, Hiroyuki Sakayori, Keiji Oshima, Kazunori Nagahata, and Tetsuya Tatsumi. Prediction of fluctuations in plasma–wall interactions using an equipment engineering system. *Japanese Journal of Applied Physics*, 48(8S1):08HC01, 2009.

[20] Seolhye Park, Hyun-Joon Roh, Yunchang Jang, Sangmin Jeong, Sangwon Ryu, Jae-Myung Choe, and Gon-Ho Kim. Vacuum pump age effects by the exposure to the corrosive gases on the cr etch rate as observed using optical emission spectroscopy in an ar/o2/cl2 mixed plasma. *Thin Solid Films*, 603:154–159, 2016.

[21] Ariane Ferreira, Agnès Roussy, and Lamine Condé. Virtual metrology models for predicting physical measurement in semiconductor manufacturing. In *2009 IEEE/SEMI Advanced Semiconductor Manufacturing Conference*, pages 149–154. IEEE, 2009.

[22] Ryan Yang and Rongshun Chen. Real-time plasma process condition sensing and abnormal process detection. *Sensors*, 10(6):5703–5723, 2010.

[23] Sang Jeen Hong and Gary S May. Neural-network-based sensor fusion of optical emission and mass spectroscopy data for real-time fault detection in reactive ion etching. *IEEE Transactions on Industrial Electronics*, 52(4):1063–1072, 2005.

[24] Real-time insight into spontaneous and plasma enhanced si etching processes with semcion process solutions. `https://www.tofwerk.com/real-time-process-monitoring-etch/`. Accessed: 2023-11-08.

[25] HJ Yeom, Min Young Yoon, Gwang-Seok Chae, Jung Hyung Kim, ShinJae You, and Hyo-Chang Lee. Real-time monitoring of the plasma density distribution in low-pressure plasmas using a flat-cutoff array sensor. *Applied Physics Letters*, 122(11), 2023.

[26] Kye Hyun Baek, Youngjae Jung, Gyung Jin Min, Changjin Kang, Han Ku Cho, and Joo Tae Moon. Chamber maintenance and fault detection technique for a gate etch process via self-excited electron resonance spectroscopy. *Journal of Vacuum Science & Technology B: Microelectronics and Nanometer Structures Processing, Measurement, and Phenomena*, 23(1):125–129, 2005.

[27] Andreas Steinbach, Martin Sussiek, Siegfried Bernhard, Stefan Wurm, Christian Koelbl, Daniel Köhler, and Dirk Knobloch. Real-time plasma etch control by means of physical plasma parameters with seers. In *In-Line Characterization, Yield Reliability, and Failure Analyses in Microelectronic Manufacturing*, volume 3743, pages 180–193. SPIE, 1999.

[28] M Sternheim, W Van Gelder, and AW Hartman. A laser interferometer system to monitor dry etching of patterned silicon. *Journal of The Electrochemical Society*, 130(3):655, 1983.

[29] Benjamin M Goldberg, Tomáš Hoder, and Ronny Brandenburg. Electric field determination in transient plasmas: in situ & non-invasive methods. *Plasma Sources Science and Technology*, 31(7):073001, 2022.

[30] HH Busta and RE Lajos. Ellipsometric end point detection during plasma etching. In *1977 International Electron Devices Meeting*, pages 12–15. IEEE, 1977.

[31] Tsanko V Tsankov and Uwe Czarnetzki. Information hidden in the velocity distribution of ions and the exact kinetic bohm criterion. *Plasma Sources Science and Technology*, 26(5):055003, 2017.

[32] Ji-Won Kwon, Sangwon Ryu, Jihoon Park, Haneul Lee, Yunchang Jang, Seolhye Park, and Gon-Ho Kim. Development of virtual metrology using plasma information variables to predict si etch profile processed by sf6/o2/ar capacitively coupled plasma. *Materials*, 14(11):3005, 2021.

[33] Shane Lynn, John Ringwood, Emanuele Ragnoli, Sean McLoone, and Niall MacGearailty. Virtual metrology for plasma etch using tool variables. In *2009 IEEE/SEMI Advanced Semiconductor Manufacturing Conference*, pages 143–148. IEEE, 2009.

[34] Shane Lynn, John V Ringwood, and Niall MacGearailt. Weighted windowed pls models for virtual metrology of an industrial plasma etch process. In *2010 IEEE International Conference on Industrial Technology*, pages 309–314. IEEE, 2010.

[35] T Motomura, Y Kasashima, O Fukuda, F Uesugi, H Kurita, and N Kimura. Note: Practical monitoring system using characteristic impedance measurement during plasma processing. *Review of Scientific Instruments*, 85(2), 2014.

[36] MNA Dewan, PJ McNally, T Perova, and PAF Herbert. Determination of sf6 reactive ion etching end point of the sio2/si system by plasma impedance monitoring. *Microelectronic engineering*, 65(1-2):25–46, 2003.

[37] Mark A Sobolewski. Monitoring sheath voltages and ion energies in high-density plasmas using noninvasive radio-frequency current and voltage measurements. *Journal of applied physics*, 95(9):4593–4604, 2004.

[38] Shicong Wang, Amy E Wendt, John B Boffard, Chun C Lin, Svetlana Radovanov, and Harold Persing. Noninvasive, real-time measurements of plasma parameters via optical emission spectroscopy. *Journal of Vacuum Science & Technology A: Vacuum, Surfaces, and Films*, 31(2):021303, 2013.

[39] John B Boffard, Chun C Lin, and Amy E Wendt. Application of excitation cross-section measurements to optical plasma diagnostics. In *Advances In Atomic, Molecular, and Optical Physics*, volume 67, pages 1–76. Elsevier, 2018.

[40] G Gifford. Applications of optical emission spectroscopy in plasma manufacturing systems. In *Advanced Techniques for Integrated Circuit Processing*, volume 1392, pages 454–465. International Society for Optics and Photonics, 1991.

[41] Vincent M Donnelly. Plasma electron temperatures and electron energy distributions measured by trace rare gases optical emission spectroscopy. *Journal of Physics D: Applied Physics*, 37(19):R217, 2004.

[42] Elisabeth Restrepo and A Devia. Optical emission diagnostic of a pulsed arc discharge. *Journal of Vacuum Science & Technology A: Vacuum, Surfaces, and Films*, 22(2):377–382, 2004.

[43] Noriyasu Ohno, M Abdur Razzak, Hiroshi Ukai, Shuichi Takamura, and Yoshihiko Uesugi. Validity of electron temperature measurement by using boltzmann plot method in radio frequency inductive discharge in the atmospheric pressure range. *Plasma and fusion research*, 1:028–028, 2006.

[44] DAO Hope, TI Cox, and VGI Deshmukh. Langmuir probe and optical emission spectroscopic studies of ar and o2 plasmas. *Vacuum*, 37(3-4):275–277, 1987.

[45] T Mehdi, PB Legrand, JP Dauchot, M Wautelet, and M Hecq. Optical emission diagnostics of an rf magnetron sputtering discharge. *Spectrochimica Acta Part B: Atomic Spectroscopy*, 48(8):1023–1033, 1993.

[46] Xi-Ming Zhu and Yi-Kang Pu. A simple collisional–radiative model for low-temperature argon discharges with pressure ranging from 1 pa to atmospheric pressure: kinetics of paschen 1s and 2p levels. *Journal of Physics D: Applied Physics*, 43(1):015204, 2009.

[47] DV Lopaev, AV Volynets, SM Zyryanov, AI Zotovich, and AT Rakhimov. Actinometry of o, n and f atoms. *Journal of Physics D: Applied Physics*, 50(7):075202, 2017.

[48] Yuri Ralchenko. *Modern methods in collisional-radiative modeling of plasmas*. Springer, 2016.

[49] JAM Van der Mullen. Excitation equilibria in plasmas; a classification. *Physics Reports*, 191(2-3):109–220, 1990.

[50] GJ Tallents. *An introduction to the atomic and radiation physics of plasmas*. Cambridge University Press, 2018.

[51] J Vlcek. A collisional-radiative model applicable to argon discharges over a wide range of conditions. i. formulation and basic data. *Journal of physics D: Applied physics*, 22(5):623, 1989.

[52] Ursel Fantz and D Wünderlich. Atomic and molecular collisional radiative modeling for spectroscopy of low temperature and magnetic fusion plasmas. *AIP Conference Proceedings*, 1344(1):204–216, 2011.

[53] Hiroshi Akatsuka. Optical emission spectroscopic (oes) analysis for diagnostics of electron density and temperature in non-equilibrium argon plasma based on collisional-radiative model. *Advances in Physics: X*, 4(1):1592707, 2019.

[54] S Iordanova and I Koleva. Optical emission spectroscopy diagnostics of inductively-driven plasmas in argon gas at low pressures. *Spectrochimica Acta Part B: Atomic Spectroscopy*, 62(4):344–356, 2007.

[55] A Palmero, ED Van Hattum, H Rudolph, and FHPM Habraken. Characterization of a low-pressure argon plasma using optical emission spectroscopy and a global model. *Journal of Applied Physics*, 101(5):053306, 2007.

[56] Xi-Ming Zhu and Yi-Kang Pu. A simple collisional–radiative model for low-pressure argon–oxygen mixture discharges. *Journal of Physics D: Applied Physics*, 40(17):5202, 2007.

[57] Zdeněk Navrátil, Pavel Dvořák, Oto Brzobohatỳ, and David Trunec. Determination of electron density and temperature in a capacitively coupled rf discharge in neon by oes complemented with a cr model. *Journal of Physics D: Applied Physics*, 43(50):505203, 2010.

[58] S Siepa, S Danko, Tsanko V Tsankov, T Mussenbrock, and U Czarnetzki. On the oes line-ratio technique in argon and argon-containing plasmas. *Journal of Physics D: Applied Physics*, 47(44):445201, 2014.

[59] K Evdokimov, M Konischev, V Pichugin, and Z Sun. Study of argon ions density and electron temperature and density in magnetron plasma by optical emission spectroscopy and collisional-radiative model. *Resource-efficient technologies*, 3(2):187–193, 2017.

[60] Edouard Desjardins, M Laurent, A Durocher-Jean, G Laroche, N Gherardi, Nicolas Naudé, and Luc Stafford. Time-resolved study of the electron temperature and number density of argon metastable atoms in argon-based dielectric barrier discharges. *Plasma Sources Science and Technology*, 27(1):015015, 2018.

[61] Kil-Byoung Chai and Duck-Hee Kwon. Optical emission spectroscopy and collisional-radiative modeling for non-equilibrium, low temperature helium plasma. *Spectrochimica Acta Part B: Atomic Spectroscopy*, 183:106269, 2021.

[62] H Horita, D Kuwahara, H Akatsuka, and S Shinohara. Estimating electron temperature and density using improved collisional-radiative model in high-density rf argon plasma. *AIP Advances*, 11(7):075226, 2021.

[63] Kil-Byoung Chai and Duck-Hee Kwon. Optical emission spectroscopy and collisional-radiative modeling for low temperature ar plasmas. *Journal of Quantitative Spectroscopy and Radiative Transfer*, 227:136–144, 2019.

[64] Antoine Durocher-Jean, Edouard Desjardins, and Luc Stafford. Characterization of a microwave argon plasma column at atmospheric pressure by optical emission and absorption spectroscopy coupled with collisional-radiative modelling. *Physics of Plasmas*, 26(6):063516, 2019.

[65] John B Boffard, RO Jung, Chun C Lin, and AE Wendt. Optical emission measurements of electron energy distributions in low-pressure argon inductively coupled plasmas. *Plasma Sources Science and Technology*, 19(6):065001, 2010.

[66] RK Gangwar, R Srivastava, AD Stauffer, et al. Collisional-radiative model for non-maxwellian inductively coupled argon plasmas using detailed fine-structure relativistic distorted-wave cross sections. *The European Physical Journal D*, 67(10):1–9, 2013.

[67] Xi-Ming Zhu, Yi-Kang Pu, Yusuf Celik, Sarah Siepa, Edmund Schüngel, Dirk Luggenhölscher, and Uwe Czarnetzki. Possibilities of determining non-maxwellian eedfs from the oes line-ratios in low-pressure capacitive and inductive plasmas containing argon and krypton. *Plasma Sources Science and Technology*, 21(2):024003, 2012.

[68] Ximing Zhu and Yikang Pu. Determination of non-maxwellian electron energy distributions in low-pressure plasmas by using the optical emission spectroscopy and a collisional-radiative model. *Plasma Science and Technology*, 13(3):267, 2011.

[69] VA Godyak and RB Piejak. Abnormally low electron energy and heating-mode transition in a low-pressure argon rf discharge at 13.56 mhz. *Physical review letters*, 65(8):996, 1990.

[70] Máté Vass, Sebastian Wilczek, Aranka Derzsi, Benedek Horváth, Peter Hartmann, and Zoltán Donkó. Evolution of the bulk electric field in capacitively coupled argon plasmas at intermediate pressures. *Plasma Sources Science and Technology*, 31(4):045017, 2022.

[71] John M. Dawson. Particle simulation of plasmas. *Rev. Mod. Phys.*, 55:403–447, Apr 1983.

[72] R W Hockney and J W Eastwood. *Computer Simulation Using Particles*. Taylor and Francis, 1988.

[73] C Birdsall and B Langdon. *Plasma Physics via Computer Simulation*. Taylor and Francis, 1991.

[74] CK Birdsall. Particle-in-cell charged-particle simulations, plus monte carlo collisions with neutral atoms, pic-mcc. *IEEE Transactions on Plasma Science*, 19(2):65–85, 1991.

[75] V Vahedi, CK Birdsall, MA Lieberman, G DiPeso, and TD Ronhlien. Capacitive rf discharges modelled by particle-in-cell monte carlo simulation. ii. comparisons with laboratory measurements of electron energy distribution functions. *Plasma Sources Science and Technology*, 2(4):273, 1993.

[76] Kazuki Denpoh and Kenichi Nanbu. *J. Vac. Sci. Technol. A: Vac. Surf. Films*, 16:1201–1206, 1998.

[77] John P Verboncoeur. Particle simulation of plasmas: review and advances. *Plasma Physics and Controlled Fusion*, 47(5A):A231, 2005.

[78] D. Tskhakaya, K. Matyash, R. Schneider, and F. Taccogna. *Contrib. Plasma Phys.*, 47:563–594, 2007.

[79] O V Proshina, T V Rakhimova, A T Rakhimov, and D G Voloshin. *Plasma Sources Sci. Technol.*, 19:065013, 2010.

[80] Z Donkó. Particle simulation methods for studies of low-pressure plasma sources. *Plasma Sources Science and Technology*, 20(2):024001, 2011.

[81] Chieh-Wen Lo and Satoshi Hamaguchi. Numerical analyses of hydrogen plasma generation by nanosecond pulsed high voltages at near-atmospheric pressure. *Journal of Physics D: Applied Physics*, 44(37):375201, aug 2011.

[82] Markus M Becker, Hanno Kählert, Anbang Sun, Michael Bonitz, and Detlef Loffhagen. Advanced fluid modeling and pic/mcc simulations of low-pressure ccrf discharges. *Plasma Sources Science and Technology*, 26(4):044001, 2017.

[83] Anbang Sun, Markus M Becker, and D Loffhagen. *Plasma Sources Sci. Technol.*, 27:054002, 2018.

[84] Thomas Charoy, Jean-Pierre Boeuf, Anne Bourdon, Johan A Carlsson, Pascal Chabert, B Cuenot, Denis Eremin, Laurent Garrigues, Kentaro Hara, Igor D Kaganovich, et al. 2d axial-azimuthal particle-in-cell benchmark for low-temperature partially magnetized plasmas. *Plasma Sources Science and Technology*, 28(10):105010, 2019.

[85] Trevor Lafleur, SD Baalrud, and Pascal Chabert. Theory for the anomalous electron transport in hall effect thrusters. i. insights from particle-in-cell simulations. *Physics of Plasmas*, 23(5):053502, 2016.

[86] Zoltán Donkó, Aranka Derzsi, M++t++ Vass, Julian Schulze, Edmund Schuengel, and Satoshi Hamaguchi. Ion energy and angular distributions in low-pressure capacitive oxygen rf discharges driven by tailored voltage waveforms. *Plasma Sources Science and Technology*, 27(10):104008, oct 2018.

[87] Zoltán Donkó, Satoshi Hamaguchi, and Timo Gans. The effect of photoemission on nanosecond helium microdischarges at atmospheric pressure. *Plasma Sources Science and Technology*, 27(5):054001, may 2018.

[88] Zoltán Donkó, Aranka Derzsi, Máté Vass, Benedek Horváth, Sebastian Wilczek, Botond Hartmann, and Peter Hartmann. *Plasma Sources Sci. Technol.*, 30:095017, 2021.

[89] Mate Vass, Peter Palla, and Peter Hartmann. Revisiting the numerical stability/accuracy conditions of explicit pic/mcc simulations of low-temperature gas discharges. *Plasma Sources Science and Technology*, 31(6):064001, 2022.

[90] D Nishijima, S Kajita, and GR Tynan. Machine learning prediction of electron density and temperature from he i line ratios. *Review of Scientific Instruments*, 92(2), 2021.

[91] Jun-Hyoung Park, Ji-Ho Cho, Jung-Sik Yoon, and Jung-Ho Song. Machine learning prediction of electron density and temperature from optical emission spectroscopy in nitrogen plasma. *Coatings*, 11(10):1221, 2021.

[92] Kamran Shojaei and Lorenzo Mangolini. Application of machine learning for the estimation of electron energy distribution from optical emission spectra. *Journal of Physics D: Applied Physics*, 54(26):265202, 2021.

[93] Thijs van der Gaag, Hiroshi Onishi, and Hiroshi Akatsuka. Arbitrary eedf determination of atmospheric-pressure plasma by applying machine learning to oes measurement. *Physics of Plasmas*, 28(3), 2021.

[94] George R McKee, Christel Fenzi, Raymond J Fonck, and Marcin Jakubowski. Turbulence imaging and applications using beam emission spectroscopy on diii-d. *Review of Scientific Instruments*, 74(3):2014–2019, 2003.

[95] GD Conway. Turbulence measurements in fusion plasmas. *Plasma Physics and Controlled Fusion*, 50(12):124026, 2008.

[96] Masaki Osakabe, Sadayoshi Murakami, Mikirou Yoshinuma, Katsumi Ida, Allan Whiteford, Motoshi Goto, Daiji Kato, Takako Kato, Kenichi Nagaoka, Tokihiko Tokuzawa, et al. Fast ion charge exchange spectroscopy measurement using a radially injected neutral beam on the large helical device. *Review of Scientific Instruments*, 79(10), 2008.

[97] Katsumi Ida, Tatsuya Kobayashi, Mikiro Yoshinuma, Tsuyoshi Akiyama, Tokihiko Tokuzawa, Hayato Tsuchiya, Kimitaka Itoh, and LHD Experiment Group. *Phys. Plasmas*, 24:122502, 2017.

[98] Marcus G Burke, Raymond J Fonck, George R McKee, and Gregory R Winz. *Rev. Sci. Instrum.*, 89:10D114, 2018.

[99] Martin Kaufmann, Friedhelm Olschewski, Klaus Mantel, Oliver Wroblowski, Qiuyu Chen, Jilin Liu, Qiuchen Gong, Daikan Wei, Yajun Zhu, Tom Neubert, et al. *CEAS Space J.*, 11:525–531, 2019.

[100] John Harlander, Ronald J Reynolds, and Fred L Roesler. *Astrophys. J.*, 396:730–740, 1992.

[101] Pascal Chabert and Nicholas Braithwaite. *Physics of radio-frequency plasmas*. Cambridge University Press, 2011.

[102] A Von Keudell and V Schulz-Von Der Gathen. Foundations of low-temperature plasma physics—an introduction. *Plasma Sources Science and Technology*, 26(11):113001, 2017.

[103] Pascal Chabert, Tsanko Vaskov Tsankov, and Uwe Czarnetzki. Foundations of capacitive and inductive radio-frequency discharges. *Plasma Sources Science and Technology*, 30(2):024001, 2021.

[104] Oleg A Popov. *High density plasma sources: design, physics and performance*. Elsevier, 1996.

[105] Santacruz Banacloche, Ana R Gamarra, Yolanda Lechon, and Chiara Bustreo. Socioeconomic and environmental impacts of bringing the sun to earth: A sustainability analysis of a fusion power plant deployment. *Energy*, 209:118460, 2020.

[106] Stefano Segantin, Raffaella Testoni, and Massimo Zucchetti. The lifetime determination of arc reactor as a load-following plant in the energy framework. *Energy policy*, 126:66–75, 2019.

[107] Mengpin Ge, Johannes Friedrich, and Leandro Vigna. Charts explain greenhouse gas emissions by countries and sectors. *World Resources Institute*, 6:2020, 4.

[108] The 17 goals. Accessed on May 13, 2024.

[109] Samuele Meschini, Francesco Laviano, Federico Ledda, Davide Pettinari, Raffella Testoni, Daniele Torsello, and Bruno Panella. Review of commercial nuclear fusion projects. *Frontiers in Energy Research*, 11:1157394, 2023.

[110] T Kenneth Fowler. Nuclear power—fusion. *Reviews of Modern Physics*, 71(2):S456, 1999.

[111] TEG Nicholas, Thomas P Davis, F Federici, J Leland, BS Patel, C Vincent, and SH Ward. Re-examining the role of nuclear fusion in a renewables-based energy mix. *Energy Policy*, 149:112043, 2021.

[112] Francesco Romanelli, P Barabaschi, D Borba, G Federici, L Horton, R Neu, D Stork, H Zohm, et al. Fusion electricity: A roadmap to the realization of fusion energy. 2012.

[113] Francis F Chen et al. *Introduction to plasma physics and controlled fusion*, volume 1. Springer, 1984.

[114] Stellarators and tokamaks: How fusion is done. `https://medium.com/@bhatmuleyshail/stellarators-and-tokamaks-how-fusion-is-done-350d416b0384`. Accessed: May 2, 2024.

[115] Doe explains...stellarators. `https://www.energy.gov/science/doe-explainsstellarators`. Accessed: May 2, 2024.

[116] Atsuo Iiyoshi, A Komori, A Ejiri, M Emoto, H Funaba, M Goto, K Ida, Hiroshi Idei, S Inagaki, S Kado, et al. Overview of the large helical device project. *Nuclear Fusion*, 39(9Y):1245, 1999.

[117] U Fantz. Basics of plasma spectroscopy. *Plasma sources science and technology*, 15(4):S137, 2006.

[118] F.J. Arellano. Numerical simulation of capacitively-coupled ar plasma and its experimental validation. Master's Thesis, 2021.

[119] Dávid J Palásti, Miklós Füle, Miklós Veres, and Gábor Galbács. Optical modeling of the characteristics of dual reflective grating spatial heterodyne spectrometers for use in laser-induced breakdown spectroscopy. *Spectrochimica Acta Part B: Atomic Spectroscopy*, 183:106236, 2021.

[120] A Gaigalas, L Wang, HJ He, and P DeRose. Procedures for wavelength calibration and spectral response correction of ccd array spectrometers. *Journal of research of the National Institute of Standards and Technology*, 114(4):215, 2009.

[121] HJ Kunze. *Introduction to plasma spectroscopy*, volume 56. Springer Science & Business Media, 2009.

[122] J Stillahn, K Trevino, and E Fisher. Plasma diagnostics for unraveling process chemistry. *Annu. Rev. Anal. Chem.*, 1:261–291, 2008.

[123] Zongyin Yang, Tom Albrow-Owen, Weiwei Cai, and Tawfique Hasan. Miniaturization of optical spectrometers. *Science*, 371(6528):eabe0722, 2021.

[124] What is a spectrometer? uv, vis and ir spectrometer explained. `https://wavelength-oe.com/articles/what-is-a-spectrometer/`. Accessed: May 4, 2024.

[125] RC Isler. *Plasma Phys. Control. Fusion*, 36:171–208, 1994.

[126] B Horváth, A Derzsi, J Schulze, I Korolov, P Hartmann, and Z Donkó. Experimental and kinetic simulation study of electron power absorption mode transitions in capacitive radiofrequency discharges in neon. *Plasma Sources Science and Technology*, 29(5):055002, 2020.

[127] A Derzsi, P Hartmann, M Vass, B Horváth, M Gyulai, I Korolov, J Schulze, and Z Donkó. Electron power absorption in capacitively coupled neon–oxygen plasmas: a comparison of experimental and computational results. *Plasma Sources Science and Technology*, 31(8):085009, 2022.

[128] Toshiaki Makabe. Metastables as a probe for low-temperature plasma characteristics in argon. *Journal of Physics D: Applied Physics*, 52(21):213002, 2019.

[129] Ilija Stefanović, Thomas Kuschel, Sandra Schröter, and Marc Böke. Argon metastable dynamics and lifetimes in a direct current microdischarge. *Journal of Applied Physics*, 116(11):113302, 2014.

[130] Benedikt Niermann, Marc Böke, Nader Sadeghi, and J Winter. Space resolved density measurements of argon and helium metastable atoms in radio-frequency generated he-ar micro-plasmas. *The European Physical Journal D*, 60(3):489–495, 2010.

[131] Ihor Korolov, Zoltán Donkó, Gerrit Hübner, Yue Liu, Thomas Mussenbrock, and Julian Schulze. Energy efficiency of voltage waveform tailoring for the generation of excited species in rf plasma jets operated in he/n2 mixtures. *Plasma Sources Science and Technology*, 30(9):095013, 2021.

[132] Ihor Korolov, Marc Leimkühler, Marc Boeke, Zoltan Donkó, Volker Schulz-von der Gathen, Lena Bischoff, Gerrit Hübner, Peter Hartmann, Timo Gans, Yue Liu, et al. Helium metastable species generation in atmospheric pressure rf plasma jets driven by tailored voltage waveforms in mixtures of he and n2. *Journal of Physics D: Applied Physics*, 53(18):185201, 2020.

[133] M Lieberman and A Lichtenberg. *Principles of Plasma Discharges and Materials Processing*. 2005.

[134] S Wilczek, J Schulze, RP Brinkmann, Z Donkó, J Trieschmann, and T Mussenbrock. Electron dynamics in low pressure capacitively coupled radio frequency discharges. *Journal of Applied Physics*, 127(18):181101, 2020.

[135] Z Juhasz, J Ďurian, A Derzsi, Š Matejčík, Z Donkó, and P Hartmann. Efficient gpu implementation of the particle-in-cell/monte-carlo collisions method for 1d simulation of low-pressure capacitively coupled plasmas. *Computer Physics Communications*, 263:107913, 2021.

[136] C Birdsall and B Langdon. *Plasma physics via computer simulation*. CRC press, 2004.

[137] B Horváth, M Daksha, I Korolov, A Derzsi, and J Schulze. The role of electron induced secondary electron emission from sio2 surfaces in capacitively coupled radio frequency plasmas operated at low pressures. *Plasma Sources Science and Technology*, 26(12):124001, 2017.

[138] AV Phelps and Z Lj Petrovic. Cold-cathode discharges and breakdown in argon: surface and gas phase production of secondary electrons. *Plasma Sources Science and Technology*, 8(3):R21, 1999.

[139] S Barral, K Makowski, Zbigniew Peradzyński, N Gascon, and M Dudeck. Wall material effects in stationary plasma thrusters. ii. near-wall and in-wall conductivity. *Physics of Plasmas*, 10(10):4137–4152, 2003.

[140] S Mattei, K Nishida, M Onai, J Lettry, MQ Tran, and A Hatayama. A fully-implicit particle-in-cell monte carlo collision code for the simulation of inductively coupled plasmas. *Journal of Computational Physics*, 350:891–906, 2017.

[141] M Horkỳ, WJ Miloch, and VA Delong. Numerical heating of electrons in particle-in-cell simulations of fully magnetized plasmas. *Physical Review E*, 95(4):043302, 2017.

[142] Lin c c database. `http://raptor.physics.wisc.edu/`.

[143] O Zatsarinny and K Bartschat. The b-spline r-matrix method for atomic processes: application to atomic structure, electron collisions and photoionization. *Journal of Physics B: Atomic, Molecular and Optical Physics*, 46(11):112001, 2013.

[144] A Bogaerts, R Gijbels, and J Vlcek. Collisional-radiative model for an argon glow discharge. *Journal of applied physics*, 84(1):121–136, 1998.

[145] Yuri Ralchenko. Nist atomic spectra database. *Memorie della Società Astronomica Italiana Supplement, v. 8, p. 96 (2005)*, 8:96, 2005.

[146] R Mewe. Relative intensity of helium spectral lines as a function of electron temperature and density. *British Journal of Applied Physics*, 18(1):107, 1967.

[147] BM Smirnov. Excited atoms. *Moscow Energoizdat*, 1982.

[148] CM Ferreira, J Loureiro, and A Ricard. Populations in the metastable and the resonance levels of argon and stepwise ionization effects in a low-pressure argon positive column. *Journal of applied physics*, 57(1):82–90, 1985.

[149] AG Zhiglinsky. Handbook of constants of elementary processes with atoms, ions, electrons and photons. *Saint Petersburg*, 1994.

[150] RK Gangwar, Lalita Sharma, Rajesh Srivastava, and AD Stauffer. Argon plasma modeling with detailed fine-structure cross sections. *Journal of Applied Physics*, 111(5), 2012.

[151] Y Yi-Qing, X Yu, and N Zhao-Yuan. Diagnosis of a low pressure capacitively coupled argon plasma by using a simple collisional-radiative model. *Chinese Physics B*, 20(1):015207, 2011.

[152] A Hartgers, J van Dijk, J Jonkers, and JAM Van Der Mullen. Crmodel: a general collisional radiative modeling code. *Computer physics communications*, 135(2):199–218, 2001.

[153] A Kramida, Y Ralchenko, J. Reader, and and NIST ASD Team. NIST Atomic Spectra Database (ver. 5.8), [Online]. Available: `https://physics.nist.gov/asd` [2021, May 21]. National Institute of Standards and Technology, Gaithersburg, MD., 2020.

[154] PJ Dagdigian. Fundamentals of optical spectroscopy. In *Laser Spectroscopy for Sensing*, pages 3–33. Elsevier, 2014.

[155] E Fill. The radiation escape factor. *Journal of Quantitative Spectroscopy and Radiative Transfer*, 39(6):489–491, 1988.

[156] David Alexander Schulenberg, Ihor Korolov, Zoltan Donko, Aranka Derzsi, and Julian Schulze. *Plasma Sources Sci. Technol.*, 30:105003, 2021.

[157] AK Bhatia and SO Kastner. Global and local doppler-profile escape factors for plane-parallel geometry. *Journal of Quantitative Spectroscopy and Radiative Transfer*, 67(1):55–63, 2000.

[158] PJ Walsh. Effect of simultaneous doppler and collision broadening and of hyperfine structure on the imprisonment of resonance radiation. *Physical Review*, 116(3):511, 1959.

[159] Takashi Fujimoto. A collisional-radiative model for helium and its application to a discharge plasma. *Journal of Quantitative Spectroscopy and Radiative Transfer*, 21(5):439–455, 1979.

[160] FE Irons. The escape factor in plasma spectroscopy—i. the escape factor defined and evaluated. *Journal of Quantitative Spectroscopy and Radiative Transfer*, 22(1):1–20, 1979.

[161] Eugene R Capriotti. Mean escape probabilities of line photons. *The Astrophysical Journal*, 142:1101, 1965.

[162] Sarah Luisa Siepa. *Global collisional-radiative model for optical emission spectroscopy of argon and argon-containing plasmas*. doctoralthesis, Ruhr-Universität Bochum, Universitätsbibliothek, 2017. Available at `https://hss-opus.ub.ruhr-uni-bochum.de/opus4/frontdoor/index/index/docId/5354`.

[163] Xi-Ming Zhu, Tsanko Vaskov Tsankov, Dirk Luggenhölscher, and Uwe Czarnetzki. 2d collisional-radiative model for non-uniform argon plasmas: with or without 'escape factor'. *Journal of Physics D: Applied Physics*, 48(8):085201, 2015.

[164] Aurélien Géron. *Hands-on machine learning with Scikit-Learn, Keras, and TensorFlow*. " O'Reilly Media, Inc.", 2022.

[165] Ali Mesbah and David B Graves. Machine learning for modeling, diagnostics, and control of non-equilibrium plasmas. *Journal of Physics D: Applied Physics*, 52(30):30LT02, 2019.

[166] Hyun-Joon Roh, Sangwon Ryu, Yunchang Jang, Nam-Kyun Kim, Younggil Jin, Seolhye Park, and Gon-Ho Kim. Development of the virtual metrology for the nitride thickness in multi-layer plasma-enhanced chemical vapor deposition using plasma-information variables. *IEEE Transactions on Semiconductor Manufacturing*, 31(2):232–241, 2018.

[167] Takuya Akiba, Shotaro Sano, Toshihiko Yanase, Takeru Ohta, and Masanori Koyama. Optuna: A next-generation hyperparameter optimization framework. In *Proceedings of the 25th ACM SIGKDD international conference on knowledge discovery & data mining*, pages 2623–2631, 2019.

[168] Megumi Iwayama, Stephen Wu, Chang Liu, and Ryo Yoshida. Functional output regression for machine learning in materials science. *Journal of Chemical Information and Modeling*, 62(20):4837–4851, 2022.

[169] Andrej Krenker, Janez Bešter, and Andrej Kos. Introduction to the artificial neural networks. *Artificial Neural Networks: Methodological Advances and Biomedical Applications. InTech*, pages 1–18, 2011.

[170] Angelo D Bonzanini, Ketong Shao, David B Graves, Satoshi Hamaguchi, and Ali Mesbah. Foundations of machine learning for low-temperature plasmas: methods and case studies. *Plasma Sources Science and Technology*, 32(2):024003, 2023.

[171] Tin Kam Ho. Random decision forests. In *Proceedings of 3rd international conference on document analysis and recognition*, volume 1, pages 278–282. IEEE, 1995.

[172] Leo Breiman. Random forests. *Machine learning*, 45:5–32, 2001.

[173] Trevor Hastie, Robert Tibshirani, Jerome H Friedman, and Jerome H Friedman. *The elements of statistical learning: data mining, inference, and prediction*, volume 2. Springer, 2009.

[174] F. Pedregosa, G. Varoquaux, A. Gramfort, V. Michel, B. Thirion, O. Grisel, M. Blondel, P. Prettenhofer, R. Weiss, V. Dubourg, J. Vanderplas, A. Passos, D. Cournapeau, M. Brucher, M. Perrot, and E. Duchesnay. Scikit-learn: Machine learning in Python. *Journal of Machine Learning Research*, 12:2825–2830, 2011.

[175] Will Koehrsen. Hyperparameter tuning the random forest in python. `https://towardsdatascience.com/hyperparameter-tuning-the-random-forest-in-python-using-scikit-lea` 2018. Accessed: May 6, 2024.

[176] VA Godyak, RB Piejak, and BM Alexandrovich. Measurement of electron energy distribution in low-pressure rf discharges. *Plasma sources science and technology*, 1(1):36, 1992.

[177] De-Qi Wen, Janez Krek, Jon Tomas Gudmundsson, Emi Kawamura, Michael A Lieberman, and John P Verboncoeur. Benchmarked and upgraded particle-in-cell simulations of a capacitive argon discharge at intermediate pressure: The role of metastable atoms. *Plasma Sources Science and Technology*, 30(10):105009, 2021.

[178] De-Qi Wen, Janez Krek, Jon Tomas Gudmundsson, Emi Kawamura, Michael A Lieberman, and John P Verboncoeur. Particle-in-cell simulations with fluid metastable atoms in capacitive argon discharges: electron elastic scattering and plasma density profile transition. *IEEE Transactions on Plasma Science*, 50(9):2548–2557, 2022.

[179] Zoltán Donkó, Peter Hartmann, Ihor Korolov, David Schulenberg, Stefan Rohr, Shahid Rauf, and Julian Schulze. Metastable argon atom kinetics in a low-pressure capacitively coupled radio frequency discharge. *Plasma Sources Science and Technology*, 32(6):065002, 2023.

Appendix A

Radiative Properties of Transitions

Table 1.1: Overview of the radiative transitions included in the CRM. The values in the table are the vacuum wavelengths of the transitions given in units of nm. The transitions marked with boldface are also examined experimentally.

λ [nm]	j	i	$A_{j\to i}$ [s^{-1}]	g_j	g_i
104.822	$1s_2$	gs	5.10×10^8	3	1
106.666	$1s_4$	gs	1.19×10^8	3	1
667.728	$2p_1$	$1s_4$	2.36×10^5	1	3
696.543	$2p_2$	$1s_5$	6.39×10^8	3	5
706. 722	$2p_3$	$1s_5$	3.80×10^6	5	5
714.704	$2p_4$	$1s_5$	6.25×10^5	3	5
727.294	$2p_2$	$1s_4$	1.83×10^6	3	3
738.398	$2p_3$	$1s_4$	8.47×10^6	5	5
747.117	$2p_4$	$1s_4$	2.20×10^4	3	3
750.387	$2p_1$	$1s_2$	4.45×10^7	1	3
751.465	$2p_5$	$1s_4$	4.02×10^7	1	3
763.511	$2p_6$	$1s_5$	2.45×10^7	5	5
772.376	$2p_7$	$1s_5$	5.18×10^6	3	5
772.421	$2p_2$	$1s_3$	1.17×10^7	3	1
794.818	$2p_4$	$1s_3$	1.86×10^7	3	1

800.616	$2p_6$	$1s_4$	4.90×10^6	5	3
801.479	$2p_8$	$1s_5$	9.28×10^6	5	5
810.369	$2p_7$	$1s_4$	2.50×10^7	3	3
811.531	$2p_9$	$1s_5$	3.31×10^7	7	5
826.452	$2p_2$	$1s_2$	1.53×10^7	3	3
840.821	$2p_3$	$1s_2$	2.23×10^7	5	3
842.465	$2p_8$	$1s_4$	2.15×10^7	5	3
852.144	$2p_4$	$1s_2$	1.39×10^7	3	3
866.794	$2p_7$	$1s_3$	2.43×10^6	3	1
912.297	$2p_{10}$	$1s_5$	1.89×10^7	3	5
922.45	$2p_6$	$1s_2$	5.03×10^6	5	3
935.422	$2p_7$	$1s_2$	1.06×10^6	3	3
965.779	$2p_{10}$	$1s_4$	5.43×10^6	3	3
978.45	$2p_8$	$1s_2$	1.47×10^6	5	3
1047.005	$2p_{10}$	$1s_3$	9.80×10^5	3	1
1148.811	$2p_{10}$	$1s_2$	1.90×10^5	3	3

Appendix B

List of Excited Levels

Table 2.1: List of Excited Levels considered in the CRM

Excited State	Principal Quantum Number (n)	Total Angular Momentum Quantum Number (J)	Energy (eV)	Statistical Weight (g)
$1s_5$	4	2	11.55	5
$1s_4$	4	1	11.62	3
$1s_3$	4	0	11.72	1
$1s_2$	4	1	11.82	3
$2p_{10}$	4	1	12.91	3
$2p_9$	4	3	13.08	7
$2p_8$	4	2	13.10	5
$2p_7$	4	1	13.15	3
$2p_6$	4	2	13.17	5
$2p_5$	4	0	13.27	1
$2p_4$	4	1	13.28	3
$2p_3$	4	2	13.30	5
$2p_2$	4	1	13.33	3
$2p_1$	4	0	13.48	1

Appendix C

Reactions included in the PIC/MCC simulations

Table 3.1: List of reactions included in the PIC/MCC simulations, as taken from Ref. 3 and Ref. 4

Reaction	Type of Reaction
$e^- + Ar \rightarrow e^- + Ar$	Elastic
$e^- + Ar \rightarrow e^- + Ar(1s_5)$	Excitation
$e^- + Ar \rightarrow e^- + Ar(1s_4)$	Excitation
$e^- + Ar \rightarrow e^- + Ar(1s_3)$	Excitation
$e^- + Ar \rightarrow e^- + Ar(1s_2)$	Excitation
$e^- + Ar \rightarrow e^- + Ar(2p_{10})$	Excitation
$e^- + Ar \rightarrow e^- + Ar(2p_9)$	Excitation
$e^- + Ar \rightarrow e^- + Ar(2p_8)$	Excitation
$e^- + Ar \rightarrow e^- + Ar(2p_7)$	Excitation
$e^- + Ar \rightarrow e^- + Ar(2p_6)$	Excitation
$e^- + Ar \rightarrow e^- + Ar(2p_5)$	Excitation
$e^- + Ar \rightarrow e^- + Ar(2p_4)$	Excitation
$e^- + Ar \rightarrow e^- + Ar(2p_3)$	Excitation
$e^- + Ar \rightarrow e^- + Ar(2p_2)$	Excitation
$e^- + Ar \rightarrow e^- + Ar(2p_1)$	Excitation

$e^- + Ar \rightarrow e^- + Ar(3d_{12}) + 3d_{11})$	Excitation
$e^- + Ar \rightarrow e^- + Ar(3d_{10})$	Excitation
$e^- + Ar \rightarrow e^- + Ar(3d_9)$	Excitation
$e^- + Ar \rightarrow e^- + Ar(3d_8)$	Excitation
$e^- + Ar \rightarrow e^- + Ar(3d_7 + 2s_5)$	Excitation
$e^- + Ar \rightarrow e^- + Ar(3d_6 + 2s_4)$	Excitation
$e^- + Ar \rightarrow e^- + Ar(3d_5)$	Excitation
$e^- + Ar \rightarrow e^- + Ar(3d_4)$	Excitation
$e^- + Ar \rightarrow e^- + Ar(3d_3 or 3d_2 + 2s_3 or 2s_2)$	Excitation
$e^- + Ar \rightarrow e^- + Ar(3d_1)$	Excitation
$e^- + Ar \rightarrow e^- + Ar(3p_{10})$	Excitation
$e^- + Ar \rightarrow e^- + Ar(3p_9)$	Excitation
$e^- + Ar \rightarrow e^- + Ar(3p_8)$	Excitation
$e^- + Ar \rightarrow e^- + Ar(3p_7)$	Excitation
$e^- + Ar \rightarrow e^- + Ar(3p_6)$	Excitation
$e^- + Ar \rightarrow e^- + Ar(3p_5)$	Excitation
$e^- + Ar \rightarrow e^- + Ar(3p_4)$	Excitation
$e^- + Ar \rightarrow e^- + Ar(3p_3)$	Excitation
$e^- + Ar \rightarrow e^- + Ar(3p_2)$	Excitation
$e^- + Ar \rightarrow e^- + Ar(3p_1)$	Excitation
$e^- + Ar \rightarrow e^- + Ar(2d)$	Excitation

$e^- + Ar \rightarrow e^- + Ar(3s)$	Excitation
$e^- + Ar \rightarrow e^- + Ar(2d')$	Excitation
$e^- + Ar \rightarrow e^- + e^- + Ar^+$	Ionization
$Ar + Ar^+ \rightarrow Ar + Ar^+$	Isotropic
$Ar + Ar^+ \rightarrow Ar + Ar^+$	Backscattering

RESEARCH ACHIEVEMENTS

PUBLICATIONS

- "First-principles simulation of optical emission spectra for low-pressure argon plasmas and its experimental validation," **F. Arellano**, M. Gyulai, Z. Donkó, P. Hartmann, Ts. V. Tsankov, U. Czarnetzki, and S. Hamaguchi, Plasma Sources Sci. Technol. 32, (2023) 125007

- "Machine learning-based prediction of the electron energy distribution and electron density of argon plasma from the optical emission spectra," **F. Arellano**, M. Kusaba, S. Wu, R. Yoshida, Z. Donkó, P. Hartmann, Ts. V. Tsankov and S. Hamaguchi, J. Vac. Sci. Technol. A, Accepted. [Editor's pick]

- "Self-consistent calculation of the optical emission spectrum of an argon capacitively coupled plasma based on the coupling of particle simulation with a collisional-radiative model," Z. Donkó, Ts. V. Tsankov, P. Hartmann, **F. Arellano**, U. Czarnetzki, S. Hamaguchi, J. Phys. D: Appl. Phys., In press.

- "Charge exchange spectroscopy using spatial heterodyne spectrometer in the large helical device," **F. Arellano**, M. Yoshinuma, and K. Ida, Rev. Sci. Instrum. 93, (2022) 033503

PRESENTATIONS

- "Machine-learning-based prediction of plasma characteristics from optical emission spectra," **Fatima Jenina Arellano**, Zoltan Donko, Peter Hartmann, Tsanko V. Tsankov, Minoru Kusaba, Stephen Wu, Ryo Yoshida, Uwe Czarnetzki, and Satoshi Hamaguchi, 74th Annual Gaseous Electronics Conference (GEC 2023), (10 October, 2023, Michigan USA) Bulletin of the American Physical Society, DT1. 00002. [GEC Student Excellence Award Finalist Presentation, Oral].

- "Common plasma models and an application: first-principles simulation of optical emission spectra for low-pressure argon plasmas and its experimental validation," **Fatima Jenina Arellano**, Marton Gyulai, Zoltan Donko, Peter Hartmann, Tsanko V. Tsankov, Uwe Czarnetzki, and Satoshi Hamaguchi, Plasma and Society II: A technical training course, (5-6 May 2023, online/Quezon City Philippines) [Invited talk]

- "Predicting plasma parameters using a machine learning-based inversion of the collisional-radiative model", **Fatima Jenina Arellano**, Minoru Kusaba, Stephen Wu, Ryo Yoshida and Satoshi Hamaguchi, The 5th International Symposium of the Vacuum Society of the Philippines (ISVSP 2024), (17-19 January, 2024, Baguio City Philippines) Plasma Science & Technologies Session [Oral].

- "Machine learning prediction of the electron density and the electron energy distribution function from the optical emission spectra," **Fatima Jenina Arellano**, Minoru Kusaba, Stephen Wu, Ryo Yoshida, Zoltan Donko, Peter Hartmann, Tsanko V. Tsankov, and Satoshi Hamaguchi, Europhysics Conference on Atomic and Molecular Physics of Ionized Gases 2024 (ESCAMPIG), (9-13 July, 2024, Brno, Czech Republic) P1-T5-19 [Poster]

- "Machine learning prediction of plasma parameters from optical emission spectra in argon plasma", **Fatima Jenina Arellano**, Marton Gyulai, Zoltan Donko, Peter Hartmann, Tsanko V. Tsankov, Uwe Czarnetzki, and Satoshi Hamaguchi, Global Plasma Forum in Aomori (GPF), (15-18 October, 2023, Aomori Japan) DX-O-1 [Oral].

- "First-principles simulation of optical emission spectra for low-pressure argon plasmas and its experimental validation," **Fatima Jenina Arellano**, Marton Gyulai, Zoltan Donko, Peter Hartmann, Tsanko V. Tsankov, Uwe Czarnetzki, and Satoshi Hamaguchi, The 25th International Symposium on Plasma Chemistry (ISPC25), (21-26 May, 2023, Kyoto Japan) POS-5-201 [Poster]

- "First-principles simulation of optical emission spectra for low-pressure argon plasmas and its experimental validation," **Fatima Jenina Arellano**, Marton Gyulai, Zoltan Donko, Peter Hartmann, Tsanko V. Tsankov, Uwe Czarnetzki, and Satoshi Hamaguchi, The 14th EU-Japan Joint Symposium on Plasma Processing (JSPP-14), (16-21 April, 2023, Okinawa Japan) P-25 [Poster]

- "Towards a validation effort of Particle-in-Cell/Monte Carlo Collision simulation coupled with Collisional Radiative Model by Optical Emission Spectroscopy," **Fatima Jenina Arellano**, Marton Gyulai, Zoltan Donko, Peter Hartmann, Tsanko V. Tsankov, Uwe Czarnetzki, and Satoshi Hamaguchi, 25th International Plasma School on "Low-Temperature Plasma Physics: Basics and Applications, Poster Session (October 1 - 8, 2022, Bad Honnef, Germany) [Poster]

- "Towards a validation effort of Particle-in-Cell/Monte Carlo Collision simulation coupled with Collisional Radiative Model by Optical Emission Spectroscopy," **Fatima Jenina Arellano**, Zoltan Donko, Peter Hartmann, Tsanko V. Tsankov, Uwe Czarnetzki, and Satoshi Hamaguchi, The 22nd International Vacuum Congress (IVC-22) (September 11-16, 2022, Sapporo, Japan).

- "Evaluation of OES line ratios using Particle-in-Cell/Monte Carlo Collision Simulation coupled with a Collisional Radiative Model," **Fatima Jenina Arellano**, Zoltan Donko, Peter Hartmann, Tsanko V. Tsankov, Uwe Czarnetzki, and Satoshi Hamaguchi, Japan-RUB Workshop: Bridging the Pandemic: Reigniting Cooperation on Plasma Research (25 November, 2021, online). [Poster]

- "Experimental Validation of Particle-in-Cell/Monte Carlo Collision simulation coupled with Collisional Radiative Model by Optical Emission Spectroscopy," **Fatima Jenina Arellano**, Zoltan Donko, Peter Hartmann, Tsanko V. Tsankov, Uwe Czarnetzki, and Satoshi Hamaguchi, Gaseous Electronics Conference (05 October, 2021, online). [Oral]

AWARDS

- Finalist, Gaseous Electronics Conference Student Excellence Award 2023
- Best Presenter, Global Plasma Forum in Aomori 2023
- Best Presenter, 5th International Symposium of the Vacuum Society of the Philippines (ISVSP 2024)
- Recipient, Japan Ministry of Education, Culture, Sports, Science and Technology (MEXT) Scholarship